Feedback-regulated Lyman continuum leakage in cosmological simulations

Nele Stachlys

Supervisors: Dr. Ewald Puchwein, Prof. Dr. Christoph Pfrommer
First Referee: Prof. Dr. Christoph Pfrommer
Second Referee: Prof. Dr. Lutz Wisotzki

Master Thesis

Astrophysics
Universität Potsdam, Leibniz Institut für Astrophysik Potsdam
June 25, 2024

Abstract

During the epoch of reionisation, the hydrogen in the intergalactic medium was ionised by Lyman-continuum radiation produced by the stars inside the first generations of galaxies. I analysed galaxies found in the high-resolution region of three zoom-in resimulations of groups from the THESAN full box simulation. The simulations were run using a modified version of the SMUGGLE galaxy formation model, which is coupled to the radiative transfer module in AREPO-RT. The radiation escaped the interstellar medium by channels formed by stellar and supernova feedback, reducing the density and ejecting gas.

I compared three methods of determining the fraction of ionising radiation escaping the ISM: Using the on-the-fly AREPO-RT M1 radiative transfer, ray-tracing from the galaxy's centre, and ray-tracing from each star using the COLT code. The method involving the COLT code proved to be the most reliable, as it does not assume that the stars are located in the galaxy's centre and does not rely on the M1 radiative transfer approximation.

I found that recent star formation is strongly correlated with the creation of low-density channels that allow radiation to escape. Somewhat surprisingly, I find a positive correlation between the escape fraction and the gas mass for well-resolved haloes. In our simulations, the stellar mass increases more strongly with halo mass than the gas mass does. The escape fraction correlates positively with halo mass. Also, more feedback per gas mass is injected in heavier haloes. This appears to mitigate the effects of deeper potential wells in more massive haloes.

Furthermore, I could identify galaxies in low-mass haloes with high escape fractions. Here, feedback and photoevaporation could eject most of the gas from the ISM. Some of these haloes are below the filtering mass, preventing gas accretion. These small galaxies, while having high escape fractions, have low escaping luminosities due to their inability to form (young and bright) stars. The escape fractions of these low-mass galaxies may also be affected by resolution issues.

Compared to a recent study from the literature (Rosdahl et al., 2022), I found a different mass dependency of the escape fraction in the galaxies in our simulations. However, a measure using the specific star formation rate showed similar results, even with our different selection function.

The work done in this thesis enabled new insight into the escape of Lyman-continuum radiation into the IGM through channels created by feedback in galaxies over 5 orders of magnitude in halo mass.

Acknowledgements

I am extremely grateful to Ewald Puchwein for being my supervisor, for his guidance through this thesis project, and for thorough discussions on my plots and the weirdest things I could find in the simulations. Many thanks to Christoph Pfrommer for being my first referee and for giving me the opportunity to write my thesis in the cosmology and high-energy physics group at the AIP. I want to thank Lutz Wisotzki for agreeing to be my second referee. I am very thankful for Aaron Smith, who took the time to explain the COLT code to me, without which the analyses in this thesis would not have been possible in this detail. I am also thankful to the THESAN zoom-in collaboration team for not only providing me with the simulations I analysed in this thesis, but also some input regarding my plots.

I am very thankful to my partner and friends for keeping the world around me spinning and for their emotional support. Furthermore, I want to especially thank Nikolai Bahr, Carlo Fulde, Kelvin Kiesewetter, and Luca Krajnik for proof-reading this thesis so thoroughly. This degree would not have been possible without the support of my parents, whom I am extremely grateful for. Last but not least, I want to thank the entire cosmology and high-energy physics group at the AIP for making my time there so far an amazing experience.

Contents

1 Introduction to cosmology and galaxy formation

1.1 Cosmology and galaxy formation

In the beginning there was nothing, which exploded.

- Terry Pratchett, Lords and Ladies

From the Big Bang to the very different state the universe is in nowadays, it evolved through a number of stages, which are studied in the field of cosmology. However, to start explaining a thing that seems too big and complicated to grasp, some assumptions must be made. These two assumptions are known as the cosmological principle, which consists of the following two statements:

1. *Homogeneity*: The universe is the same no matter where the observer is, i.e. there is the same distribution of matter everywhere.

2. *Isotropy*: No matter which direction in the universe an observer looks, it looks the same.

These assumptions are true on scales of $\gtrsim 300$ Mpc; otherwise, matter would be the same everywhere and structures like Galaxies would not exist.

Through these assumptions, the metric given in Einstein's general relativity can be simplified to a form that can actually be used to describe the background expansion of our universe

$$ds^2 = -c^2 dt + a^2(t)\left[d\omega^2 + f_K^2(\omega)d\Omega^2\right] . \tag{1.1}$$

In this equation ω and $f_K(\omega)$ have the dimension of a length, ω is the radial coordinate in a spherical coordinate system and $f_K(\omega)$ is defined as

$$f_K^2(\omega) = \begin{cases} K^{-1/2}\sin(K^{1/2}\omega) & (K > 0) \\ \omega & (K = 0) \\ |K|^{-1/2}\sinh(|K|^{1/2}\omega) & (K < 0) \end{cases} . \tag{1.2}$$

a in these equations is the scale factor of the universe. It is defined to be 1 at the current time and size of the universe and is smaller at earlier times, as the universe was smaller then. For example, at the scale factor $a = 1/2$, the universe was half the size of the universe today. K is the curvature of the universe. A universe with $K = 0$ is spatially flat, and a universe with $K < 0$ or $K > 0$ has a negative or positive curvature, respectively. c is the speed of light, $\mathrm{d}\Omega^2 = \mathrm{d}\theta^2 + \sin^2\theta \mathrm{d}\phi^2$ and t time.

To move further, the universe is assumed to be a perfect fluid, such that the energy-momentum tensor in Einstein's field equations is only dependent on pressure P and density ρ. These are both only dependent on time due to the homogeneity of the universe. Using this in combination with Equation (1.1), we recover two equations solving Einstein's field equations, the Friedmann equations

$$\left(\frac{\dot{a}}{a}\right)^2 = \frac{8\pi G}{3}\rho - \frac{Kc^2}{a^2} + \frac{\Lambda c^2}{3}, \tag{1.3}$$

$$\frac{\ddot{a}}{a} = -\frac{4\pi G}{3}\left(\rho + \frac{3P}{c^2}\right) + \frac{\Lambda c^2}{3}. \tag{1.4}$$

Motivated by Equation (1.3) the Hubble parameter $H(t)$ is defined as

$$H(t) \equiv \frac{\dot{a}}{a}. \tag{1.5}$$

The Hubble constant is the Hubble parameter determined at the current time t_0, $H_0 = H(t_0)$.

The density $\rho(t)$ is comprised of the matter density $\rho_m(t)$ and the radiation density $\rho_r(t)$. Both of these are dependent on the scale factor as

$$\rho_m = \rho_{m,0}a^{-3} \tag{1.6}$$

and

$$\rho_r = \rho_{r,0}a^{-4}, \tag{1.7}$$

in which $\rho_{m,0}$ is the matter density and $\rho_{r,0}$ the radiation density at the current time. The critical density ρ_{cr} is defined as

$$\rho_{cr} \equiv \frac{3H^2(t)}{8\pi G}. \tag{1.8}$$

The critical density at the current time is similarly defined to the Hubble constant $\rho_{cr,0} = \rho_{cr}(t_0)$. Next, the dimensionless density parameters are defined. The dimensionless density parameter of matter is

$$\Omega_m(t) \equiv \frac{\rho_m(t)}{\rho_{cr}(t)}, \quad \Omega_{m,0} \equiv \frac{\rho_m(t_0)}{\rho_{cr,0}}. \tag{1.9}$$

The dimensionless density parameter for the radiation is defined similarly as

$$\Omega_r(t) \equiv \frac{\rho_r(t)}{\rho_{cr}(t)}, \quad \Omega_{r,0} \equiv \frac{\rho_r(t_0)}{\rho_{cr,0}}. \tag{1.10}$$

The density parameter for the cosmological constant is

$$\Omega_\Lambda(t) \equiv \frac{\Lambda c^2}{3H^2(t)}, \quad \Omega_{\Lambda,0} \equiv \frac{\Lambda c^2}{3H_0^2}. \tag{1.11}$$

Substituting the dimensionless density parameters and the Hubble parameter into the Friedman equation Equation (1.3) yields

$$E^2(a) \equiv \frac{H^2(t)}{H_0^2} = \left[\Omega_{\mathrm{r},0} a^{-4} + \Omega_{\mathrm{m},0} a^{-3} + \Omega_\Lambda + \Omega_{\mathrm{K},0} a^{-2}\right]. \tag{1.12}$$

In this equation we substituted $\Omega_{\mathrm{K},0}$ for the expression containing the curvature K in Equation (1.3), but $\Omega_{\mathrm{K},0}$ can also be found using the other density parameters with

$$\Omega_{\mathrm{K},0} \equiv -\frac{Kc^2}{H_0^2} = 1 - \Omega_{\mathrm{r},0} - \Omega_{\mathrm{m},0} - \Omega_{\Lambda,0}. \tag{1.13}$$

In the cosmology of our universe, $\Omega_{\mathrm{K},0}$ is very close to 0, so our universe is approximately flat. The other density parameters are $\Omega_{\mathrm{r},0} = (4.67 \pm 0.26) \times 10^{-5}$, $\Omega_{\mathrm{m},0} = \Omega_{\mathrm{d},0} + \Omega_{\mathrm{b},0} = (0.227 \pm 0.014) + (0.0456 \pm 0.0016)$ ($\Omega_{\mathrm{d},0}$ is the dark matter density parameter and $\Omega_{\mathrm{b},0}$ is the baryonic density parameter) and $\Omega_{\Lambda,0} = 0.728^{+0.015}_{-0.016}$. H_0 is defined through the Hubble constant h as $H_0 = 100h \,\frac{\mathrm{km}}{\mathrm{s\,Mpc}}$. The Hubble constant is measured as $h = 0.704^{+0.013}_{-0.014}$ (Planck Collaboration et al., 2020).

In the radiation-dominated universe (starting after inflation and lasting until redshift $z \approx 3000$), in the beginning, thermal equilibrium is maintained as the timescale of particle scatterings is much shorter than the timescale of expansion. However, as the universe expands further, the thermal equilibrium cannot be maintained and breaks down. Particles freeze out as they do not gain energy from collisions anymore. For example, Neutrinos are frozen out at $k_B T_\nu = 2.7$ MeV. When protons and neutrons have frozen out, the universe goes through a phase of Nucleosynthesis, forming light elements like hydrogen-2 (deuterium), helium-3 and -4, and lithium-7. As the universe cools down further at around $k_B T_{\mathrm{rec}} = 0.3$ eV the electrons and protons start to form hydrogen atoms (Recombination), dropping the ionisation fraction of the universe almost down to 0 over time. Additionally to particles freezing out, the photons decouple from the baryons during recombination and form what we know as the cosmic microwave background (CMB).

1.1.1 Structure formation

In order to explain the structure formation of the universe, we follow the standard model of cosmology - ΛCDM. It postulates the cosmological constant Λ, fueling the expansion of the universe, and cold dark matter (CDM), i.e. dark matter (DM) having a velocity dispersion so small that structure formation is not influenced by the dispersion.

At this point, the universe is made up of hydrogen and some other light elements like helium and lithium, as well as DM. It is a soup of atoms and DM and still pretty homogeneous everywhere. Inhomogeneities are crucial for structure formation in the universe and to grow these, some force is needed.

The only one acting over such large distances - although very weak - is gravity. The gravitational force acts on everything that has mass - Baryons and DM. This force can be described by Newtonian gravity on an expanding background.

To describe the inhomogeneities in the cosmic fluid, the conservation of mass and momentum and the Poisson equation of gravity is used. The mass conservation equation is given as (e.g. Bartelmann and Pfrommer, 2023)

$$\frac{\partial \rho}{\partial t} + \nabla \cdot (\rho \boldsymbol{v}) = 0, \tag{1.14}$$

where $\boldsymbol{v}$ is the velocity. The momentum conservation (Euler's) equation is

$$\frac{\partial \boldsymbol{v}}{\partial t} + (\boldsymbol{v} \cdot \nabla)\boldsymbol{v} = -\frac{\nabla P}{\rho} - \nabla \Phi, \tag{1.15}$$

in which P is the pressure. Lastly, the Poisson equation of gravity is

$$\nabla^2 \Phi = 4\pi G \rho, \tag{1.16}$$

in which Φ is the gravitational potential and G is the gravitational constant. To look at the perturbations separately from the homogeneous background, the density and velocity are decomposed as

$$\rho(t, \boldsymbol{x}) = \rho_0(t) + \delta\rho(t, \boldsymbol{x}), \boldsymbol{v}(t, \boldsymbol{x}) = \boldsymbol{v}_0(t) + \delta \boldsymbol{v}(t, \boldsymbol{x}), \tag{1.17}$$

where $\rho_0(t)$ and $\boldsymbol{v}_0(t)$ are the homogeneous background values and $\delta\rho(t, \boldsymbol{x})$ and $\delta\boldsymbol{v}(t, \boldsymbol{x})$ the perturbations of the density and velocity, respectively.

By applying this decomposition to Equations (1.14) to (1.16) and defining the density contrast $\delta \equiv \frac{\delta\rho}{\rho_0}$, we get

$$\dot{\delta} + \boldsymbol{v}_0 \cdot \nabla \delta + \nabla \cdot \delta \boldsymbol{v} = 0, \tag{1.18}$$

$$\frac{\partial \delta \boldsymbol{v}}{\partial t} + (\delta \boldsymbol{v} \cdot \nabla)\boldsymbol{v}_0 + (\boldsymbol{v}_0 \cdot \nabla)\delta \boldsymbol{v} = -\frac{\nabla \delta P}{\rho_0} - \nabla \delta \Phi \tag{1.19}$$

and

$$\nabla^2 \delta \Phi = 4\pi G \rho_o \delta. \tag{1.20}$$

In the next step, these equations will be converted into comoving coordinates, yielding

$$\dot{\delta} + \nabla \boldsymbol{u} = 0, \tag{1.21}$$

$$\dot{\boldsymbol{u}} + 2H\boldsymbol{u} = -\frac{\nabla \delta P}{a^2 \rho} - \frac{\nabla \delta \Phi}{a^2} \tag{1.22}$$

and

$$\nabla^2 \delta\Phi = 4\pi G\rho_0 a^2 \delta. \tag{1.23}$$

Additionally, an equation of state is defined as

$$\delta P = \delta P(\delta) = c_s^2 \delta\rho = c_s^2 \rho_0 \delta, \tag{1.24}$$

which connects the pressure to the density fluctuations. At this point, a single expression can be formed, describing the density contrast as

$$\ddot{\delta} + 2H\dot{\delta} = 4\pi G\rho_0 \delta + \frac{c_s^2 \nabla^2 \delta}{a^2}. \tag{1.25}$$

Through decomposing δ into plane waves, i.e. Fourier transforming it, this can lastly be turned into

$$\ddot{\hat{\delta}} + 2H\dot{\hat{\delta}} = 4\pi G\rho_0 \hat{\delta} - \frac{c_s^2 k^2 \hat{\delta}}{a^2}. \tag{1.26}$$

With a static background and setting $H = 0$, this formula is turned into the oscillator equation

$$\ddot{\delta} + \omega_0^2 \delta = 0, \; \omega_0 \equiv \sqrt{\frac{c_s^2 k^2}{a^2} - 4\pi G\rho_0}, \tag{1.27}$$

which at sufficiently large wavenumbers k has real frequencies ω_0, and in which c_s is the soundspeed. The threshold at which the frequencies become real is the the Jeans length

$$\lambda_J \equiv \frac{c_s}{a}\sqrt{\frac{\pi}{G\rho_0}}, \tag{1.28}$$

which for a single fluid describes how large density perturbations have to be in order to grow or decay rather than just oscillate. For pressureless fluids, the perturbation equations turn into

$$\ddot{\hat{\delta}} + 2H\dot{\hat{\delta}} = \frac{3}{2}H^2 \hat{\delta}, \tag{1.29}$$

for the matter-dominated universe and

$$\ddot{\hat{\delta}} + 2H\dot{\hat{\delta}} = 4H^2 \hat{\delta}, \tag{1.30}$$

for the radiation-dominated universe.

Pressureless fluids do not have a sound speed. Their Jeans length is defined through the velocity dispersion v of particles as

$$\lambda_J \equiv \frac{< v^{-2} >^{-1/2}}{a}\sqrt{\frac{\pi}{G\rho_0}}. \tag{1.31}$$

In this case, not the collisions are preventing the growth of perturbations, but rather their gravity is insufficient to keep the particles bound. In the regime of CDM, the velocity dispersion is very close to 0, such that perturbations can grow on all scales.

Only modes that grow are important for structure formation, as their constructive interference leads to the formation of overdensities (positive amplitudes) and voids (negative amplitudes). These overdensities can then collapse into walls, filaments, or haloes hosting galaxies or clusters. This structure formation cannot happen during the radiation-dominated era, as the radiation pressure is too high for modes entering the horizon to continue growing. Therefore, when a mode with wavelength λ enters the horizon ($\lambda < c/H$) it is suppressed. As the universe expands, it becomes matter-dominated at redshift ~ 3400 and modes entering the horizon at this point are able to grow. Their density contrast grows according to the linear perturbation theory until close to unity, where this description breaks down. Non-linear evolution causes density-perturbation modes to couple moving power from intermediate to smaller scales as structures collapse. Large scales continue to evolve independently.

These structures are in the form of filaments and pancakes. When such filaments fragment into small knots, they form haloes. In ΛCDM, the first haloes to collapse are rather small. Often, these structures move towards each other to form larger and larger structures to, in the end, form galaxies and galaxy clusters. Galaxies form at smaller constructive interference sites, while clusters form at larger ones. In short, first galaxies are formed, then galaxy groups, and finally clusters. This is called bottom-up or hierarchical structure formation. It is caused by amplitudes of small-scale fluctuations being the largest, which leads to them reaching non-linear densities first.

1.1.2 Galaxy formation

One can approximate the state that haloes are in before collapse as a spherical and uniform overdensity. This is not quite the case, but it makes it easier to explain the collapse itself. During the collapse, one can imagine the halo as an onion with different shells. All these shells collapse inwards at the same timescale, keeping the overdensity uniform. This model continues to the overdensity collapsing until an infinite density is formed and then expanding again. However, this is wildly unphysical, and in reality, the overdensity is not uniform, and deviations from the radial infall are randomising the motion, leading to the virialisation of the halo. The virialised region will roughly have an overdensity 200 times the critical density ρ_{crit} (e.g. White, 2001). The radius in which the matter is gravitationally bound for such a halo is hence called the virial radius ($r_{200,\mathrm{crit}}$).

In high-redshift galaxies, gas accretes in cold mode accretion (Benson and Bower, 2010; Kereš et al., 2005). The gas accretes from cosmic filaments and rather large distances (Rauch et al., 2013). In hot mode accretion, which one would see in higher mass galaxies, the gas accreting onto the halo comes from the matter surrounding the halo and is shock heated by an accretion shock before falling inwards. For haloes with masses $M_{\rm DM} \lesssim 10^{10.4}$ $M_\odot$ this is not the case and the cold gas accretes without getting heated (Birnboim and Dekel, 2003; Kereš et al., 2005; van de Voort et al., 2012). Nonetheless, the gas must lose its kinetic energy. This is either done by drag processes (Benson and Bower, 2010) in the halo or by a shock close to its centre. This converts the kinetic energy to thermal energy, which is directly radiated away (Benson and Bower, 2010). Cold accretion leads to rather efficient star formation at early times (Dekel and Birnboim, 2006).

The first so-called minihaloes to form stars had potential wells deep enough, such that gas, although having a net velocity in comparison to the DM (Schauer et al., 2019; McQuinn and O'Leary, 2012; O'Leary and McQuinn, 2012; Greif et al., 2011; Naoz et al., 2012; Tseliakhovich and Hirata, 2010) could accrete onto them. The formation of the first stars began at $z \approx 20 - 30$ (Abel et al., 2002; Tegmark et al., 1997; Glover, 2005; Riaz et al., 2022). The haloes are expected to have masses between $10^5 - 10^6$ $M_\odot$ (Glover, 2005; Abel et al., 2002; Tegmark et al., 1997). The gas accreting onto the halo at this point only consisted of hydrogen, helium, and trace amounts of lithium. The typical temperature ($< 10^4$ K) in the protogalaxies is too low for atomic hydrogen cooling, and the lack of metals prohibited metal cooling, such that they relied on the comparatively inefficient cooling via molecular hydrogen (H_2) instead (Saslaw and Zipoy, 1967; Bromm, 2013). The formation of and cooling via H_2 is well described in the review of Glover (2011) as the following: In minihaloes, H_2 at first formed through the processes

$$\mathrm{H} + \mathrm{e}^- \rightarrow \mathrm{H}^- + \gamma \tag{1.32}$$

and

$$\mathrm{H}^- + \mathrm{H} \rightarrow \mathrm{H}_2 + \mathrm{e}^-. \tag{1.33}$$

Due to this, the initial formation of H_2 was highly bounded by the free electron fraction. As the free electron fraction decreased due to the recombination of atoms, the formation of molecular hydrogen stopped. The H_2 formed in the halo allowed the gas to cool to $\sim$200 K and collapse under self-gravity, accumulating at the centre of the halo. Once a high enough density is reached, H_2 can again form, this time through three-body processes. This leads to quickly forming H_2 from most of the hydrogen. However, even though more H_2 is now available for cooling, the gas does not cool significantly at this time, as the binding energy is converted into heat, balancing the cooling. The collapse of the gas continues until the gas is dense enough that it becomes optically thick, inhibiting the cooling via radiative processes. Afterwards, the gas heats up, dissociating the H_2 and in the end, halting the collapse of the core. At this point, the core has formed a protostar. An accretion disk forms around this star, onto which gas inflows faster than can be fed to the protostar. This causes the accretion disk to become gravitationally unstable and fragment, forming more protostars.

The first stars forming are called Population III (Pop III) stars, which were quite massive due to the inefficient H_2 cooling. The supernovae (SNe) of heavy Pop III stars were the first things to inject metals into the interstellar medium (ISM). However, their SNe, in combination with feedback due to photoionisation, stripped the minihaloes off their gas, as they had rather shallow potential wells (Bromm and Yoshida, 2011). The end of the formation of Pop III stars is induced by themselves, as they strip their host haloes of gas and enrich the surrounding medium with metals (Bromm, 2013; Tornatore et al., 2007). They form roughly until the end of the reionisation, as not all parts of the universe form minihaloes at the same time (Mebane et al., 2018). The stars with higher metallicities formed after the Pop III stars are Population II (Pop II) stars, which have smaller masses and higher metallicities.

As heavier haloes (10^7 to 10^9 $M_\odot$) collapsed (Wise, 2019; Bromm and Yoshida, 2011) incorporating minihaloes, the first proper (dwarf) galaxies formed were rather gas-poor, but had a higher metal fraction. They still had a sufficiently low mass for cold accretion; however, their interiors were hot enough for atomic hydrogen cooling ($T > 10^4$ K). In addition, their metal fraction enables them to conduct metal line cooling whenever the gas cools below the temperature where atomic cooling is possible. This enhances the star formation inside of the galaxy (Choi and Nagamine, 2009). Even galaxies that are not enriched with metals have the ability to cool to high densities in a process described by Oh and Haiman (2002). In these cases, the galaxies are able to form gravitationally stable disks by hydrogen cooling. In these, the density is high enough, such that H_2 can be formed at short timescales and cooling by it leads to fragmentation. Additionally, these galaxies had high enough temperatures in their interiors to form Population II stars. As their potential wells were deeper than the ones of the minihaloes, stellar and SN feedback could not strip their gas as easily.

Lyman-Werner Radiation

Massive Pop III stars (and stars thereafter) produce UV radiation, which can influence the gas surrounding them in two main ways in these early times. One way is through photoionisation, which I will discuss further in Section 1.2, and the other is photodissociation. Radiation with energies in the range of 11.2 to 13.6 eV is able to photodissociate H_2 and is called Lyman-Werner (LW) radiation.

Once the first stars have formed in a minihalo, the LW radiation can inhibit further star formation by dissociating the molecular hydrogen and hence hinder their ability to cool and fragment (Haiman et al., 2000). Additionally, this radiation could influence minihaloes in the vicinity (Ahn et al., 2009). For heavier but metal-poor haloes, this radiation does not have a large influence, as the timescale of which these haloes can form H_2 is so short that the LW radiation will not influence their cooling much. Generally speaking, LW radiation could have a rather large impact on the star formation in galaxies by dissociating their molecular hydrogen (Ahn et al., 2009; Haiman et al., 2000; Navarro and Steinmetz, 1997; Machacek et al., 2001; O'Shea and Norman, 2008). However, research by Latif and Khochfar (2019); Schauer et al. (2021) on this topic has shown, that the self-shielding of H_2 is effective, and LW radiation will not have a large impact on star formation.

X-ray radiation

X-rays in the early universe are mainly produced by high-mass X-ray binaries (Mirabel et al., 2011; Klessen and Glover, 2023) but also through active galactic nuclei (AGN), hot shocked gas in SN remnants and cosmic ray electrons ejected by SN remnants, which were inverse Compton scattered on CMB photons (Oh, 2001). The universe is optically thin for radiation with hard X-ray energies (Klessen and Glover, 2023; Furlanetto et al., 2006). The radiation, already produced by Pop III stars, can hence not only influence its own protogalaxy/-galaxy but also form an X-ray background.

X-rays influence gas in two ways: Firstly, they can heat up the gas. Secondly, they can ionise the gas, which fuels the H_2 formation through the resulting free electrons (Haiman et al., 2000). In theory, the ionisation from X-ray radiation might fuel the H_2 formation enough that the destruction by LW radiation is balanced out. In numerical studies (Glover and Brand, 2003; Klessen and Glover, 2023), it appears that the LW radiation dominates.

Supernovae

SNe can be split up into Types I and II. Type I SNe show no hydrogen lines in their emission, and type II SNe do show hydrogen lines. The most important forms of SNe for feedback are type Ia and II SNe. Type Ia SNe go off after hundreds of Myr or even a few Gyr after the formation of the star (Brandt et al., 2010; Maoz et al., 2012). Type II SNe go off after a couple of Myr up to 200 Myr after their birth, in the case of late SNe (Zapartas et al., 2017). The evolution of SNe after their explosion is described in e.g. Brantseg (2013) and Cox (1972). At first, the shock created by the SN explosion expands into the ISM with almost no resistance, sweeping up material in the process. In this stage, the shock is expanding with roughly the velocity of the original explosion. After some time the mass swept up and carried along the shock reached masses comparable to the SN ejecta. At this point, the SN shock reached the adiabatic phase, also called the Sedov-Taylor phase (after the Sedov-Taylor self-similar blast wave model, SEDOV, 1959). The shock wave is moving outward, only influenced by the already injected energy. After further expansion, the accumulated material at the shock wave starts cooling radiatively. A thin shell is formed, moving outward through its momentum.

Stellar and supernova feedback

Feedback is the process of injecting matter, energy, and momentum into a medium. In the case of the first galaxies, the most significant feedback is stellar and SN feedback of early stars (Trebitsch et al., 2017). Two feedback processes were already described above: LW feedback and X-ray feedback. However, stellar feedback can take many shapes, e.g. stellar winds, photoionisation and radiation pressure. What appears to be the most efficient feedback in the early universe is photoionisation and SN feedback, which will be touched upon in the next section. Another form of feedback that becomes important is the feedback through infrared (IR) radiation (Olivier et al., 2021). As this infrared radiation in galaxies is produced by heating dust particles, this feedback only becomes important later on. Dust is formed through the condensation of metals, so the first SNe must have happened before this feedback can become efficient (Dwek, 1998; Cherchneff and Dwek, 2010; Nozawa et al., 2003; Triani et al., 2020).

Cosmological simulations of the first galaxies usually show rather high Star Formation Rates (SFRs) before the feedback of the first SNe reduces these by blowing out the gas of the ISM. These high SFRs are inconsistent with observations of the first galaxies. However, in the results from JWST, many star-forming galaxies at high redshifts were found (e.g. Adams et al., 2022; Haro et al., 2023; Labbé et al., 2023; Donnan et al., 2022, 2023; Finkelstein et al., 2023), challenging the old observations. An explanation for this might be feedback-free starbursts (Li et al., 2023; Dekel et al., 2023).

The former observed low SFRs implied a need for early stellar feedback in galaxies (Stinson et al., 2013). A theory on where this feedback might be coming from is the resonant scattering of Lyman-α photons (Kimm et al., 2018) on gas, injecting momentum into the gas of the galaxy. This, in turn, can suppress the star formation inside of these early galaxies. Lyman-α radiation is emitted whenever an electron in a hydrogen atom jumps from the first excited state to the ground state. The electron moving to the excited state is facilitated either by ionised hydrogen recombining with an electron or collisions. As this radiation is fueled by the photoionising feedback provided by Pop III stars, its onset is much earlier than the first SNe.

1.2 Cosmic reionization

When the first stars have formed inside the first galaxies and are injecting (Lyman-Continuum) radiation into the ISM, the neutral hydrogen in the ISM starts to become ionised. In these ionised regions, two processes are prominent: The ionisation and recombination of hydrogen. The ionisation of hydrogen atoms happens when a photon with an energy higher than 13.6 eV is absorbed by a neutral hydrogen atom, ejecting an electron. Radiation with this energy is called Lyman-Continuum radiation. Recombinations happen if the ionised hydrogen has a temperature of a few $\times 10^4$ K and combines with an electron - emitting a photon in the process. As more hydrogen is ionised than recombined, these so-called HII regions or ionised bubbles are growing. The source of the radiation, i.e. the stars in the galaxy, has a finite amount of photons it gives off per second. Over time, the HII regions are heating up and expanding due to photoionisation, which causes a shock between the less dense gas around the ionised bubble and the surrounding ISM, pushing the gas of the ISM outward. The ionised bubble can then expand further into the lower-density gas. At a certain point, the ionised bubble has grown large enough that all the photons coming from the source are "used up" by ionising recombined hydrogen atoms; it has formed a Strömgren sphere. This means that the ionised bubble is in an equilibrium state and will not grow any further.

The ISM is rather dense, and some help is needed for the radiation to escape into the intergalactic medium (IGM). Next to the photoionisation feedback described above, this help is provided in the form of other stellar and especially SN feedback. The SN feedback can eject the gas out of the ISM more efficiently in less dense regions, e.g. such regions that have been subjected to photoionisation feedback. This feedback creates channels of low neutral hydrogen column densities in which the ionising radiation can escape the ISM. The fraction of HI ionising radiation escaping the ISM into the IGM is called escape fraction $f_{\rm esc}$.

The feedback injected by stars can also affect galaxies other than their host galaxy in a process called photoevaporation. The ionisation front of galaxies expanding into the IGM supersonically can sweep up the gas of other dwarf galaxies (Shapiro and Raga, 2000; Shapiro et al., 2004; D'Aloisio et al., 2019; Iliev et al., 2005). When entering such a dwarf galaxy, the ionisation front slows down, forming a shock (Shapiro and Raga, 2000; Shapiro et al., 2004; Iliev et al., 2005). When passing through the dwarf galaxy, much of the gas in the ISM is heated up and ejected back into the IGM (Shapiro et al., 2004; Iliev et al., 2005). The leftover gas in the ISM, which would otherwise not be affected due to self-shielding, can now be boiled out of the halo by photoionising radiation (Barkana and Loeb, 1999; Shapiro et al., 2004). This heating happens as the excess energy provided by photons ionising hydrogen is thermalised. This process can remove gas from small haloes and, in turn, increase the escape fraction through feedback from external sources.

Some of these minihaloes once had deep enough potential wells to accrete gas, but are now unable to as the ISM and IGM were heated up by photoionisation. Due to the increase in temperature, the pressure of the gas increases as well, preventing it from accreting onto the minihaloes. The mass of haloes below which no gas can be accreted is called filtering mass (Gnedin, 2000). The filtering mass increases throughout the epoch of reionisation, as the temperature does. The ejection (by photoevaporation and feedback) and the inability of these haloes to accrete new gas prevents further star formation in them.

Cosmic reionisation occurred between redshift $z = 15$ and ~ 5.3 (Bosman et al., 2022; Kulkarni et al., 2019). During this time, the ionised bubbles went through three phases: in the first phase, each galaxy had its own ionised bubble; in the second phase, the ionised bubbles of nearby galaxies started to combine; and in the third phase, most of the hydrogen in the IGM is ionised with only a few neutral patches left. Nowadays, the matter in the universe is highly ionised. This process can be nicely seen in Figure 1, which shows the ionised hydrogen

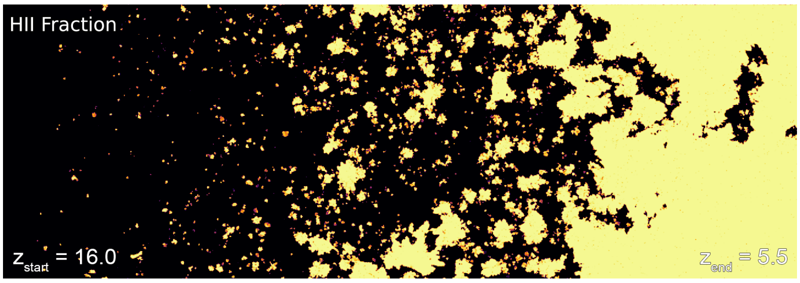

Figure 1: Image showcasing the ionised hydrogen fraction from redshift 16 until redshift 5.5. This image was taken from the website of the THESAN collaboration (`https://www.thesan-project.com/`).

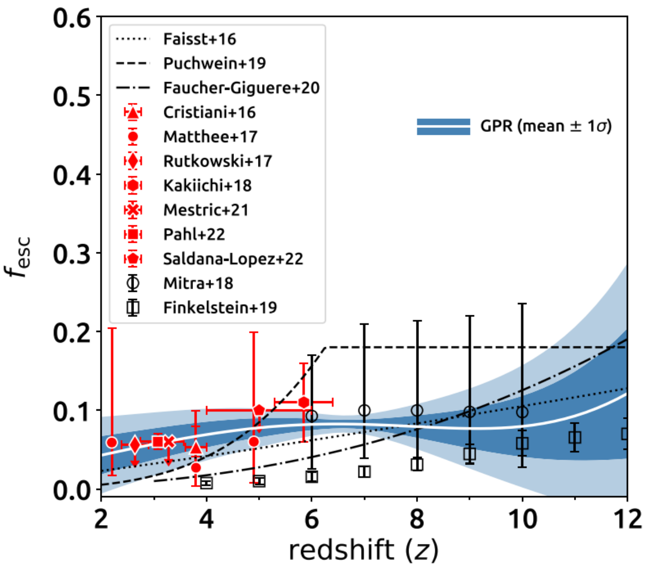

Figure 2: Escape fraction versus redshift taken from Mitra and Chatterjee (2023). The red symbols show some observational constraints on escape fractions. The dotted lines are fits to these. The white line shows a reconstruction done in the paper itself based on a data-driven reionisation model. The dark blue shaded region is the 1σ confidence interval, and the light blue region is the 2σ confidence interval. The open circles and squares show two additional reconstructions.

fraction from redshift 16 until redshift 5.5.

It is not possible to measure the escape fraction of these early galaxies directly, as the intervening neutral hydrogen absorbs all of the ionising radiation. However, as the matter in the universe nowadays is already highly ionised, the escape fractions of present-day galaxies can be measured. Figure 2 shows a few measured escape fractions as red symbols, and some fits can be seen as dotted lines. The white line shows a reconstruction by Mitra and Chatterjee (2023), with the 1σ confidence limit being dark blue and the 2σ confidence limit shown in light blue. The escape fractions of galaxies until redshift 4 typically lie between 0 and 0.1, which means that less than 10 per cent of the ionising radiation from these galaxies reaches the IGM. If early galaxies had a similar escape fraction, not enough radiation would reach the IGM for reionisation to happen. However, this has recently been questioned by Muñoz et al. (2024), as the JWST results suggest a larger amount of star-forming galaxies as high redshifts as previously expected. Cosmological simulations can be used to investigate how high the escape fractions during reionisation actually were.

1.3 Previous simulations investigating the escape fractions of galaxies

In this section, I want to review some work on the analysis of escape fractions in simulations from the literature. The simulations in all three papers that I will discuss have been conducted using the adaptive mesh refinement code RAMSES (Teyssier, 2002). To include radiation in these simulations, RAMSES-RT was used (Rosdahl et al., 2013), which models the radiation using the M1 radiative transfer technique (for a more in-depth explanation, see Section 2.2) and uses non-equilibrium hydrogen and helium thermochemistry. The galaxy formation simulations were conducted using the SPHINX model (Rosdahl et al., 2018).

Rosdahl et al. (2022) studied the escape fractions of haloes and their correlation with the mass and SFR. For this, a (20 cMpc)^3 volume and two (10 cMpc)^3 volumes were simulated. The radiation was modelled using the M1 radiative transfer method and a variable speed of light approximation, enabling non-equilibrium hydrogen and helium thermochemistry, including photoionisation and radiation pressure feedback. The cooling rates of heavier elements were implemented using CLOUDY (López Fernández et al., 2018) for temperatures larger than 10^4 K and using the fine structure metal cooling rates from Rosen and Bregman (1995) for lower temperatures. Molecular hydrogen cooling was not implemented; an initial metal fraction was set to enable cooling in the first galaxies. They implemented SNe as individual feedback injections around star particles at ages 3 to 50 Myr. The momentum injected by an SN is split up between the host cell of the SN and the surrounding cells. In the host cell, the energy is injected thermally if the resolution can capture the expansion of the SN bubble; otherwise, it is injected as momentum. In the cells connected to the host cell, a fraction of the momentum is injected. In order for the star formation to be in line with observations, the energy injected by SNe was boosted four-fold.

The escape fractions of the galaxies formed in the two simulations run by Rosdahl et al. (2022) were calculated using RASCAS (Michel-Dansac et al., 2020). This uses a Monte Carlo radiative transfer approach to avoid the effects of the variable speed of light approximation when using the M1 flux to determine the escape fraction. Using a non-variable but reduced speed of light approximation, Trebitsch et al. (2017) compared the escape fractions determined using the M1 flux and the escape fraction determined by RASCAS. They simulated three relatively isolated galaxies. They found that both methods of determining the escape fraction are almost equal, as the stars are formed in and stay in the centre of the galaxy.

Rosdahl et al. (2022) find a correlation between the stellar mass and the escape fraction with a maximum escape fraction at about 10^7 $M_\odot$. The decrease towards high stellar masses is suspected to be due to a decreased efficiency of stellar feedback within high-mass galaxies. The decrease towards low stellar masses is possibly due to the star formation being unsustained over time in low-mass galaxies. This leads to less efficient SN feedback and, thus, to a lack of channels being formed for Lyman Continuum radiation to escape through. The ionising radiation feedback suppresses the clustering of star formation in these low-mass galaxies, and the efficiency of SNe is weakened, as less stellar feedback disperses the gas. The higher-mass galaxies, however, have a more clustered star formation, such that the feedback is able to clear away gas from young stars, leading to higher escape fractions.

They could not find a clear positive correlation between the escape fraction and the specific SFR (sSFR) over the last 10 Myr. Galaxies with a lower sSFR show a higher escape fraction than galaxies with a medium sSFR. Although this is the case, galaxies with a medium sSFR show a larger escaping luminosity due to a higher internal luminosity. Afterwards, they did the same analysis, but with the maximal sSFR in 10 Myr intervals throughout the last 50 Myr. This is because these galaxies might have had a period of high SFR in their recent history, which expelled much of their gas, leading to a high escape fraction now, although their SFR might have decreased significantly. Using this measure, they find a better correlation between the escape fraction and the star formation. The analysis based on the maximal sSFR additionally showed less redshift dependence than the analysis using just the sSFR. The escape fraction, or for that matter, the escaping luminosity, was observed to be rather bursty in their simulation, only escaping when efficient feedback was present.

One might suggest that AGN play a role in the injection of either feedback or radiation into the ISM. The influence of AGN on the escape fractions and the escaping luminosity was analysed in Trebitsch et al. (2018), where one halo was simulated multiple times using different feedback mechanisms. A similar galaxy simulation model was used as in Trebitsch et al. (2017) (described above).

All runs that included SN feedback showed a very bursty escape fraction and behaved similarly. The SN feedback hinders black hole growth as it expels the gas from around the black hole. Black hole growth, on the other hand, did not influence the escape fraction; it was not able to remove the gas before the ejection by SN feedback. The radiation produced by the AGN escaped at the same time as the radiation from the stars, and only a fraction of the radiation produced by the AGN escaped into the IGM. Additionally, AGN only produce a fraction of the radiation produced by stars in the epoch of reionisation. This suggests that AGN did not have a significant impact on the reionisation of the universe, neither on the aspect of feedback nor luminosity.

In this thesis, the escape fractions of galaxies in the epoch of reionisation are investigated in cosmological galaxy formation simulations. These galaxy formation simulations are zoom-in simulations of galaxies found in the THESAN (Kannan et al., 2022; Smith et al., 2022; Garaldi et al., 2022) simulation. The simulations are based on a modified version of the SMUGGLE (Marinacci et al., 2019) galaxy formation model. The hydrodynamics and DM dynamics of the simulation are solved with the AREPO code Springel (2010), and the radiative transfer is treated with AREPO-RT (Kannan et al., 2019).

In Section 2, I will discuss the galaxy formation simulations in more detail. In Section 3, I explain the methods used to determine the escape fractions of galaxies found in the simulations. In Section 4, I analyse and compare the different methods of determining escape fractions. In Section 5.2, I analyse the escape fractions of galaxies under the aspects of time evolution, star formation, and stellar, gas and halo mass. Finally, my conclusions are presented in Section 6 and an outlook in Section 7.

2 Galaxy formation simulations with AREPO

2.1 (Magneto)hydrodynamics in AREPO

For the simulation of gas and DM in the universe, AREPO (Springel, 2009, 2010, 2011; Weinberger et al., 2020) is used. The simulations are performed in a box of fixed comoving size with periodic boundary conditions.

The properties of the gas in the simulation are discretised on a Voronoi mesh with different cells. The cells get assigned the properties of the gas in that region. The mesh is created using mesh generating points, which move roughly with the velocity of the gas. The gravitation acting on both the gas and DM is solved by combining octrees and particle mesh algorithms (Springel, 2010; Weinberger et al., 2020). These forces are then used to evolve the velocity of mesh-generating points and result in a different coordinate at the next time step. To find out which parts of the gas are sampled by which mesh generating point, a Voronoi mesh is generated. In a Voronoi mesh, a mesh generating point is assigned the volume closer to this point than any other to form cells. An example of the resulting mesh in 2D is depicted in Figure 3. In AREPO the Voronoi mesh is 3-dimensional and found using Delauney triangulation (Springel, 2011, 2009).

The next step is to determine how the gas properties evolve over time. To model the gas in the universe, it is assumed to be a fluid. It can then be described by the magnetohydrodynamic equations

$$\frac{\partial \rho}{\partial t} + \frac{1}{a}\nabla \cdot (\rho \boldsymbol{v}) = 0, \tag{2.1}$$

$$\frac{\partial \rho a \boldsymbol{v}}{\partial t} + \nabla \cdot \left(\rho \boldsymbol{v}\boldsymbol{v}^T + \boldsymbol{I}P_{\text{tot}} - \frac{\boldsymbol{B}\boldsymbol{B}^T}{a} \right) = -\frac{\rho}{a}\nabla\Phi, \tag{2.2}$$

$$\frac{\partial a^2 E}{\partial t} + a\nabla \cdot \left[\boldsymbol{v}(E + P_{tot}) - \frac{1}{a}\boldsymbol{B}(\boldsymbol{v}\cdot\boldsymbol{B}) \right] = \frac{\dot{a}}{2}\boldsymbol{B}^2 - \rho(\boldsymbol{v}\cdot\nabla\Phi) + a^2(\mathcal{H} - \Lambda), \tag{2.3}$$

$$\frac{\partial \boldsymbol{B}}{\partial t} + \frac{1}{a}\nabla \cdot (\boldsymbol{B}\boldsymbol{v}^T - \boldsymbol{v}\boldsymbol{B}^T) = 0. \tag{2.4}$$

In these equations ρ is the density, $\boldsymbol{v}$ is the velocity, t is the time, $\boldsymbol{B}$ is the magnetic field strength, Φ is the gravitational potential, P_{tot} is the total pressure, E the total energy density, and $a^2(\mathcal{H} - \Lambda)$ is a term describing external heating and cooling (Pakmor and Springel, 2013; Weinberger et al., 2020).

Since a computer is not able to solve these equations analytically, the solution is found numerically by the approach explained by Springel (2010) and Weinberger et al. (2020) in seven steps.

1. Generate a new Voronoi mesh based on the coordinates of the mesh generating points. This also gives the centre of mass and volume of each cell, as well as the areas and centres of each face at the boundary to another cell.

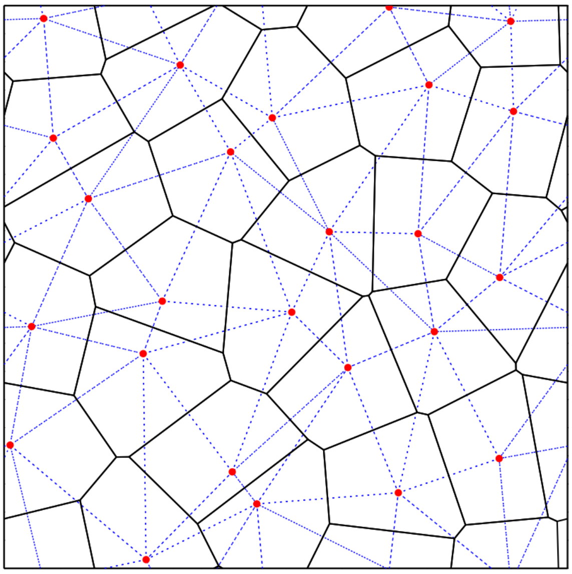

Figure 3: Voronoi mesh in two dimensions taken from Springel (2011). The mesh is generated with periodic boundary conditions. The black lines show the Voronoi mesh, and the dotted blue lines show the Delaunay triangulation. The mesh-generating points are shown as red dots.

2. Calculate the gradient of the primitive variables $\rho_i, \boldsymbol{v}_i, \boldsymbol{B}_i$ in each cell according to Pakmor et al. (2016).

3. Update the velocity of the mesh generating points.

4. Evaluate a new size of time step based on the Courant criterion.

5. Determine the flux across each face between Voronoi cells. This is done by first calculating the states left and right of the face and predicting the states of them half a timestep forwards. Next, the Riemann problem is solved in the rest frame of the face. Lastly, the result is transformed back to the lab frame.

6. Update the primitive variables of each mesh generating point.

7. Lastly, assign new positions for the mesh-generating points based on their velocity.

To combine gravity and magnetohydrodynamics, as both influence the velocity of each fluid element, the fluid elements are evolved for half a timestep by gravitational forces at first. Next, they are evolved through the fluid equations for one timestep. Lastly, they are evolved by the gravitational force for half a timestep again. While evolving in time, the fluid elements are able to follow gravitational collapse, which, in addition to radiative cooling, is needed for galaxy formation. Further information on how galaxy and star formation is implemented can be found in Section 2.3.

To remove the unphysical two-body interactions between the cells (or rather mesh generating points), gravitational softening is implemented (Weinberger et al., 2020). This replaces the Newtonian gravity for small distances, replacing it with a function declining to zero. The softening length for the gas is dependent on the volume V of the cell as

$$\epsilon_{\text{cell}} = f_h \left(\frac{3V}{4\pi}\right)^{1/3}. \tag{2.5}$$

Here, f_h is an input parameter varying the size of the softening dependent on the cell size. The softening parameter of DM is set as a constant.

The results of these simulations are put out as snapshots of all cell and DM properties at predefined scale factors, which can then be analysed in post-processing.

2.2 AREPO-RT and M1 radiative transfer

The radiation field in simulations conducted with AREPO-RT (Kannan et al., 2019) is computed through discretisation of the radiative transfer equation (Mihalas and Mihalas, 1984)

$$\frac{1}{c}\frac{\partial I_\nu}{\partial t} + \boldsymbol{n} \cdot \nabla I_\nu = j_\nu - \kappa_\nu \rho I_\nu. \tag{2.6}$$

In this equation, I_ν is the specific density, $\boldsymbol{n}$ is the direction of the radiation, j_ν is the emission term and κ_ν the absorption coefficient.

There are multiple approaches to discretising this, including ray tracing or a Monte Carlo approach. Here, it is solved for its zeroth and first moment, (e.g. Levermore, 1984), yielding the transfer equations

$$\frac{\partial E_r}{\partial t} + \nabla \cdot \boldsymbol{F}_r = S - \kappa_E \rho \tilde{c} E_r, \tag{2.7}$$

$$\frac{\partial \boldsymbol{F}_r}{\partial t} + \tilde{c}^2 \nabla \cdot \mathbf{P}_r = -\kappa_F \rho \tilde{c} \boldsymbol{F}_r, \tag{2.8}$$

where radiation energy density E_r, flux $\boldsymbol{F}_r$ and pressure $\mathbf{P}_r$ are defined as follows

$$\{\tilde{c}E_r, \boldsymbol{F}_r, \mathbf{P}_r\} = \int_{\nu_1}^{\nu_2} \int_{4\pi} \{1, \boldsymbol{n}, \boldsymbol{n} \otimes \boldsymbol{n}\}\ I_\nu \mathrm{d}\Omega \mathrm{d}\nu. \tag{2.9}$$

In the transfer equations, S is a source term which quantifies the radiation emitted, and κ_E and κ_F are the radiation energy density and radiation flux weighted mean opacities within the frequencies ν_1 and ν_2. The speed of light c was replaced with the signal speed of the radiation transport $\tilde{c}$. $\tilde{c}$ can differ from the speed of light if the reduced speed of light approximation (RSLA) is used. A very high speed of light leads to small timesteps in the numerical integration of these equations. This would lead to executing computationally expensive parts of the simulation (radiative transfer, mesh generation, and gravity) often. An RSLA is accurate enough when the characteristic velocities of a simulation are significantly smaller than the speed of light (Gnedin and Abel, 2001).

The pressure can be determined from the radiation energy density using the Eddington tensor $\mathbf{D}$ through the Eddington tensor formalism (Levermore, 1984)

$$\mathbf{P}_r = E_r \mathbf{D}. \tag{2.10}$$

The Eddington tensor can be approximated by adopting the M1 closure, which is only dependent on the properties of the cell,

$$\mathbf{D} = \frac{1-\chi}{2}\mathbf{I} + \frac{3\chi - 1}{2}\boldsymbol{n} \otimes \boldsymbol{n}. \tag{2.11}$$

χ and $\boldsymbol{n}$ in the above equation are defined as

$$\boldsymbol{n} = \frac{\boldsymbol{F}_r}{|\boldsymbol{F}_r|}, \chi = \frac{3+4f^2}{5+2\sqrt{4-3f^2}}, f = \frac{|\boldsymbol{F}_r|}{\tilde{c}E_r}. \tag{2.12}$$

What is left is to couple the photons to the gas in the simulation. This is done through photon absorption and scattering. These processes are quantified through κ_E and κ_F. Absorption introduces source terms to the hydrodynamical equations for momentum and energy conservation, which will then be used to facilitate the coupling of photons to gas. The hydrodynamical equations then turn into

$$\frac{\partial(\rho \boldsymbol{v})}{\partial t} + \nabla \cdot (\rho \boldsymbol{v}\boldsymbol{v}^T + P\boldsymbol{I}) = \frac{\kappa_F \rho \boldsymbol{F}_r}{c}, \tag{2.13}$$

$$\frac{\partial(\rho E)}{\partial t} + \nabla \cdot [(\rho E + P)\boldsymbol{v}] = -\Lambda + \kappa_E \rho \tilde{c} E_r + \frac{\kappa_F \rho}{c}\boldsymbol{F}_r \cdot \boldsymbol{v}. \tag{2.14}$$

In these equations, Λ is the gas cooling rate, which is dependent on the abundance of ionic species present in the gas (their evolution is explained later in this section), P is the thermal pressure, E is the total energy per unit mass, and $\boldsymbol{v}$ is the gas velocity field.

To combine the transport and coupling to gas, an operator split approach - the Strang split scheme - is used, yielding second-order accuracy. This scheme results in the following three steps as explained in Kannan et al. (2019).

1. Half step upgrade of (E_r, $\boldsymbol{F}_r$) due to the source terms in the hydrodynamical equations 2.13 and 2.14

2. Full step upgrade of (E_r, $\boldsymbol{F}_r$) due to the transport equations 2.7 2.8

3. Half step upgrade of $(E_r, \boldsymbol{F}_r)$ due to the source terms in the hydrodynamical equations 2.13 and 2.14

To see how different energy bins i of radiation interact with different ionic species j like hydrogen-I, hydrogen-II, etc., Equation (2.7) and Equation (2.8) can be rewritten in terms of the photon number density N^i_γ, the photon number flux $\boldsymbol{F}^i_\gamma$ and the pressure tensor $\mathbf{P}^i_\gamma$. These values are defined as

$$\{\tilde{c}N^i_\gamma, \boldsymbol{F}^i_\gamma, \tilde{c}\mathbf{P}^i_\gamma\} = \int_{\nu_{i1}}^{\nu_{i2}} \frac{1}{h\nu} d\nu \int_{4\pi} \{1, \boldsymbol{n}, (\boldsymbol{n} \otimes \boldsymbol{n})\} I_\nu \mathrm{d}\Omega, \tag{2.15}$$

with $\nu_{i1} \leq \nu_i < \nu_{i2}$ defining the threshold of the frequency bins i. Equation (2.7) and Equation (2.8) can then be reformulated as (e.g. Kannan et al., 2019)

$$\frac{\partial N^i_\gamma}{\partial t} + \nabla \cdot \boldsymbol{F}^i_\gamma = -\sum_j \tilde{c} n_j N^i_\gamma \bar{\sigma}_{ij} - \kappa_i \rho \tilde{c} N^i_\gamma + \sum_j s_{ij} \tag{2.16}$$

and

$$\frac{\partial \boldsymbol{F}^i_\gamma}{\partial t} + \tilde{c}^2 \nabla \cdot \mathbf{P}^i_\gamma = -\sum_j \tilde{c} n_j \boldsymbol{F}^i_\gamma \bar{\sigma}_{ij} - \kappa_i \rho \tilde{c} \boldsymbol{F}^i_\gamma, \tag{2.17}$$

in which n_j is the number density of species j, κ_i is the dust opacity for radiation in the frequency bin i, $\bar{\sigma}_{ij}$ is the mean ionisation cross-section of the species j in the frequency bin i and s_{ij} is a source term for photons stemming from recombination, which gets important in optically thin media.

Equation (2.16) and Equation (2.17) are solved in an operator split approach as well. First, the transport equations are solved (by setting the right-hand-side of Equations (2.16) and (2.17) to 0) as described above, then the thermochemistry equations are solved through

$$\frac{\partial N^i_\gamma}{\partial t} = -\tilde{c} N^i_\gamma \left(\sum_i n_j \bar{\sigma}_{ij} + \kappa_i \rho \right) + \sum_j s_{ij}, \tag{2.18}$$

$$\frac{\partial \boldsymbol{F}^i_\gamma}{\partial t} = -\tilde{c} \boldsymbol{F}^i_\gamma \left(\sum_j n_j \bar{\sigma}_{ij} + \kappa_i \rho \right). \tag{2.19}$$

These are coupled to the number density evolution of the ionic species. The species considered in our version of AREPO-RT (Kannan et al., 2020) are hydrogen-I, hydrogen-II, helium-I, helium-II, helium-III, and molecular hydrogen. The change in number density over time of these species is determined by the collisional ionisation and recombination rates, as well as photoionisation. In the case of molecular hydrogen, the number density also changes due to the formation of H_2 on dust grains, the formation rate in the gas phase and through three-body interactions, the collisional destruction rate, and the photodissociation rate due to LW radiation.

The amount of radiation (or number of photons) injected in a certain frequency bin, e.g. hydrogen ionising radiation, is determined from stellar population synthesis models. The luminosity of stars is split into multiple frequency bins, which are of interest, e.g. HI ionising radiation, HeI ionising radiation and HeII ionising radiation. The luminosity of each star in each frequency bin is integrated from these tables. For a deeper explanation of how this is performed in AREPO-RT, refer to Section 3.1. The injection of radiation will be further explained in the next section.

2.3 The SMUGGLE-RT galaxy formation model

A modified version of the SMUGGLE model (Marinacci et al., 2019) is employed for the galaxy simulations used in this thesis, which includes radiative transport and early stellar feedback. This model is referred to as SMUGGLE-RT in this thesis. The coupling of SMUGGLE to the radiative transport of AREPO-RT is explained in Kannan et al. (2020). The galaxy formation model used can be split up into five sections. The first one is the (magneto-)hydrodynamics solver AREPO (Springel, 2010), the second one is the radiative transfer with AREPO-RT (Kannan et al., 2019), the third one is gas heating and cooling, the fourth one is the star formation implementation and the fifth one is the stellar feedback implementation. AREPO and AREPO-RT have already been introduced in Section 2.1 and Section 2.2 respectively.

The gas heating and cooling in SMUGGLE-RT contains hydrogen and helium cooling, metal line cooling, photoelectric heating, and cooling due to dust-gas radiation field interaction. The atomic hydrogen and helium cooling is modelled self-consistently according to Katz et al. (1996). The low-temperature molecular hydrogen cooling is calculated through the formula

$$\Lambda(\mathrm{H_2}) = \Lambda(n \to 0)_{\mathrm{H_2,H_I}} n_{\mathrm{H_2}} n_{\mathrm{H_I}} + \Lambda(n \to 0)_{\mathrm{H_2,H_2}} n_{\mathrm{H_2}}^2, \tag{2.20}$$

in which $\Lambda(n \to 0)_{\mathrm{H_2,H_I}}$ and $\Lambda(n \to 0)_{\mathrm{H_2,H_2}}$ are the low-density limits of the molecular hydrogen collisional cooling coefficients (Hollenbach and McKee, 1979), $n_{\mathrm{H_I}}$ is the neutral hydrogen number density and $n_{\mathrm{H_2}}$ the molecular hydrogen number density. These hydrogen and helium cooling rates are coupled to the radiation through the abundance of the ionic species, described in Section 2.2. The metal-line cooling is implemented by fitting the CLOUDY cooling tables (Ferland et al., 1998). The cosmic ray ionisation and heating are implemented through the approach by Indriolo and McCall (2012). Photoelectric heating is modelled according to Wolfire et al. (2003). Additionally, AREPO-RT adds the energy exchange between gas and dust, as described by Burke and Hollenbach (1983).

The star formation in SMUGGLE is stochastically modelled. For a gas cell to be eligible for star formation, it must have a gas number density higher than 10 cm^3 and be Jeans unstable, such that $r_{\mathrm{cell}} > \lambda_j$, in which r_{cell} is the radius of the cell calculated from the cell volume, assuming the cell is a sphere and $\lambda_j = c_s\sqrt{\pi/(G\rho_{\mathrm{gas}})}$, with ρ_{gas} being the gas density of the cell. If these criteria are fulfilled, the SFR of the gas cell is calculated via

$$\dot{M}_* = \epsilon \frac{M_{\mathrm{gas}}}{t_{\mathrm{dyn}}}, \tag{2.21}$$

in which $\epsilon = 1$ is an efficiency factor, M_{gas} is the gas mass of the cell and t_{dyn} is the gravitational dynamical time, defined as

$$t_{\mathrm{dyn}} = \sqrt{\frac{3\pi}{32G\rho_{\mathrm{gas}}}}, \tag{2.22}$$

in which ρ_{gas} is the gas density of the cell.

In the time Δt, the fraction of gas mass $p \equiv 1 - \exp(-\dot{M}_*\Delta t/M_i)$ is converted to a star. p^* is drawn from a uniform distribution from the interval [0,1]. The cell or part of the cell is then converted to a star particle if $p^* < p$.

Three types of stellar feedback are implemented in SMUGGLE: SN, radiation and stellar wind feedback. SMUGGLE-RT includes a fourth kind of feedback, early stellar feedback, which is described in Section 2.5. To inject the SN feedback, the number of expected SNe in a given timeframe is determined. As the cooling radius of SNe can typically not be resolved in simulations, the momentum $p_{\mathrm{SN,tot}}$ caused by the PdV work injected in the Sedov-Taylor phase is injected in the surrounding cells of the SN. The cells within the coupling radius, i.e. the 32 closest cells of the SN (kernel-weighted neighbour number), are considered for this. Each of these cells gets assigned a weight $\tilde{w}_i$ based on its solid angle as seen from the position of the SN. The weight is normalised in a way that all weights sum to 1. The momentum injected to each of the cells within the injection radius is

$$\Delta p_i = \tilde{w}_i \min\left[p_{\mathrm{SN,tot}}\sqrt{1 + \frac{m_i}{\Delta m_i}}, p_t\right]. \tag{2.23}$$

In this formula, m_i is the mass of the gas cell, $\Delta m_i = \tilde{w}_i(M_{\mathrm{SNII,tot}} + M_{\mathrm{SNIa,tot}})$, with $M_{\mathrm{SNII,tot}}$ being the mass ejected by type II SNe and $M_{\mathrm{SNIa,tot}}$ the mass being ejected by type Ia SNe, and p_t is the terminal momentum, which is the approximate momentum of the SN blast at the cooling radius. The mass and energy ejected by SNe are also injected into the cells inside the coupling radius, based on the weights $\tilde{w}_i$ of the gas cells.

The radiative transfer in AREPO-RT enables the modelling of radiative feedback self-consistently. The photoionisation rate of the non- or not completely ionised species mentioned above is given by

$$\dot{n}_j = -\tilde{c} n_j \sum_i \bar{\sigma}_{ij} N^i_\gamma. \tag{2.24}$$

The photoheating rate is given by

$$H = \sum_j n_j \Gamma_j, \tag{2.25}$$

with

$$\Gamma_j = \tilde{c} \sum_i N^i_\gamma \bar{\sigma}_{ij} h_{ij}. \tag{2.26}$$

In these formulae, h_{ij} is the mean excess of energy of photons beyond their ionisation energy, dependent on frequency bin and ionic species.

The radiation pressure is added as a source term in the momentum conservation equation as

$$\frac{\partial \rho \boldsymbol{v}}{\partial t} = \frac{1}{c} \sum_i \boldsymbol{F}^i_\gamma \left(\sum_j n_j \bar{\sigma}_{ij} p_{ij} + \kappa_i \rho e_i \right), \tag{2.27}$$

where p_{ij} is the momentum injected by radiation in the frequency bin i on ionic species j and e_i is the mean photon energy of frequency bin i.

For the feedback of stellar winds of OB stars, the mass loss M_{loss} of these stars is calculated and during each timestep t the mass gets deducted from the star. The energy injected from these winds is (Hopkins et al., 2018)

$$E_{\text{winds}} = M_{\text{loss}} \Psi \times 10^{12} \text{ erg g}^{-1}, \tag{2.28}$$

in which

$$\Psi = \frac{5.94 \times 10^4}{1 + \left(\frac{t_{\text{Myr}}}{2.5}\right)^{1.4} + \left(\frac{t_{\text{Myr}}}{10}\right)^5} + 4.83, \tag{2.29}$$

with t_{Myr} being the age of the star in Myr. The momentum injected is

$$p_{\text{winds}} = \sqrt{2 M_{\text{loss}} E_{\text{winds}}}. \tag{2.30}$$

The injection into individual gas cells is conducted as explained for SN feedback.

2.4 Finding galaxies in simulations

Two approaches are used to find gravitationally bound objects in simulations. The first one is a Friend-of-Friends (FoF) algorithm, which works with a maximum distance of the nearest neighbour of a DM particle (Springel, 2010; Weinberger et al., 2020). Starting at one DM particle, each particle closer than the maximum distance is added to the FoF group. Then, one iterates over the newly added particles and finds the particles within the maximum distance to those. This is continued until no more particles can be found within the maximum distance of each particle belonging to the group.

These groups can have substructures in which merging haloes have retained some of their structure and, hence, are visible as density peaks. To find these regions, Springel et al. (2001) introduced the Subfind algorithm. To identify the overdensities, the DM particles are iterated over by density, and the two nearest neighbours of each particle i are considered. If none of these particles has a higher density than i, which means none of the particles belongs to a group yet, the particle is the start of a new group. If one of these particles or both are in the same group, the particle is added to that. If both of these particles have different labels, then i is considered a saddle point. The two groups are considered subhalo candidates, and another group is formed where i joins the two groups. Next, the algorithm checks if the subhalo candidates are gravitationally bound. The centre of the halo is considered the position of the most bound particle, and the velocity of this particle is used to normalise the other velocities of the particles in the subhalo candidate. After adding the Hubble flow to these velocities to derive the physical velocity of each particle, one can easily see if the particle is gravitationally bound. If more than a predefined number of particles are bound, then the subhalo candidate is considered a subhalo. What remains a problem is one particle being part of more than one subhalo. This is accounted for by assigning each particle to only the smallest subhalo it is part of. This does not affect the larger subhaloes containing these small subhaloes largely, as the substructures usually have significantly smaller masses compared to the parent subhaloes.

In order to do analyses of the time series of one halo, one has to be able to identify the progenitors of a halo and, especially the main progenitor. This has been implemented into the subfind code in one of the latest updates (Springel et al., 2021).

2.5 The THESAN zoom-in simulations

The galaxy simulations I am investigating in this thesis are zoom-in simulations of galaxies found in the THESAN simulation. The THESAN simulation is a large-box (95.5 cMpc) AREPO simulation. For the radiation in THESAN, AREPO-RT is used. The galaxies are modelled with the IllustrisTNG model (Weinberger et al., 2017; Pillepich et al., 2018). This simulation aimed to simulate the epoch of reionisation and matched observations, like the reionisation history, Lyman-α transmission and predictions for 21 cm measurements. One of the results of the THESAN can be seen in Figure 1, showing the reionised regions combining over time, ionising the universe.

The galaxies found in THESAN are then resimulated using a higher resolution and SMUGGLE-RT. The galaxy itself is modelled as a high-resolution

simulation	group	$M_{200,\mathrm{crit}}$ [$\mathrm{M}_\odot$]	z_{end}	zoom factor	$M_{\mathrm{res,gas}}$
large	39	4.25×10^{12}	3	4	9.1×10^3
medium	1921	4.74×10^{10}	4.6	4	9.1×10^3
small	500531	1.94×10^9	3	8	1.1×10^3

Table 1: Groups of which zoom-in simulations were used in the analysis in this thesis. The first column shows the name of the group used in this thesis, the second column shows the group number, the third column shows the virial mass of the group at the redshift the simulation ended at, which is shown in column four, and column five shows the zoom factor and column six the gas resolution.

region and surrounded by a low-resolution region to save computational resources but still enable the surrounding medium to influence the galaxy itself. For a smoother transition, there are some cells of medium resolution around the high-resolution region. The SMUGGLE model itself has some shortcomings when used in a cosmological context, as it overproduces stellar mass at high redshift. In the modified code used for these zoom-in simulations, early stellar feedback is implemented as momentum injections before the first SNe can blow out the gas from the halo. Additionally, a limiting radius is implemented, such that the momentum is only injected in a specific region around a star and blowing very large bubbles in the ISM is avoided.

The input parameter for the gravitational softening of the gas f_h found in Equation (2.5) is set to 2.8 with a minimal softening length of 0.046875 ckpc/h being enforced. The constant softening length for the DM is set to 0.375 ckpc/h.

The zoom-in simulations I analysed in this thesis are shown in Table 1. The first column shows the name used for the simulation in the analyses. The second column shows the THESAN group resimulated in the zoom-in simulations. The third column shows the halo mass at the end of the simulation at the redshift shown in the fourth column. The fifth column shows the zoom factor, which is the factor of improvement of the linear resolution in comparison to the THESAN simulation. The gas mass resolution resulting from each zoom factor is shown in column six. All simulations have a boxsize of 44000 ckpc.

2.6 Post processing with COLT

The Cosmic Lyman α Transfer (COLT) code is a Monte Carlo code originally written to simulate the Lyman α resonant scattering through neutral hydrogen (Smith et al., 2015). However, here, I use it to model Lyman-Continuum radiation. The radiation is injected in the form of photon packets, and the number of photon packets per frequency bin is quantified through tables of the stellar spectra.

The star at which a photon packet is injected is drawn based on its luminosity. However, to better account for less luminous stars (which are otherwise poorly sampled), a bias is implemented, which is later accounted for. I will first start by explaining the unbiased case to make the biased case easier to understand. In the unbiased case, a (to follow the terminology of Smith et al. (2015)) "Probability Distribution Function" (PDF) is formed from the luminosity L_i of the star as

$$\mathrm{PDF} = \frac{L_i}{\sum_i L_i}, \tag{2.31}$$

which is normalised to 1 by dividing it by the sum of the luminosities of all stars in the galaxies. This is then cumulatively summed up to form a "cumulative distribution function" (CDF). Each star contributes its luminosity to the CDF. Next, a number between 0 and 1 is chosen, and according to this, a star is picked from the CDF. Leading to a selection with a probability based on the star's luminosity. Here, it becomes apparent that the photon packets are more likely to get injected at high-luminosity stars.

A similar method is implemented to decide which frequency bin gets assigned to the photon. This time, the PDF is chosen according to which frequency bin the star has the highest luminosity in. From this, a CDF is created, and the bin is chosen by uniformly drawing a number between 0 and 1.

In the biased case of photon packet injection, the bias $\beta = 0.5$ is implemented. Using this, the PDF becomes

$$\mathrm{PDF} = \frac{L_i^{\beta}}{\sum_i L_i^{\beta}}. \tag{2.32}$$

Here, it becomes clear that the probability of injecting a photon packet at a high-luminosity star is decreased, and the probability of injecting a photon packet at a low-luminosity star is increased. However, this needs to be accounted for when calculating escape fractions. This will be explained further in Section 3.4.

The initial direction $\boldsymbol{k_i}$ of each photon packet injected at the star is drawn from an isotropic distribution. The optical depth τ_{cell} of a path of length l_{cell} of a photon packet flying in direction $\boldsymbol{k_i}$ from the source through a certain cell containing a number density of neutral hydrogen n_{HI} is

$$\tau_{\mathrm{cell}} = n_{\mathrm{HI}} \bar{\sigma}_{\mathrm{HI}} l_{\mathrm{cell}}, \tag{2.33}$$

where $\bar{\sigma}_{\mathrm{HI}} = 3.30693 \times 10^{-28}$ cm^2 is the mean photoionisation cross section for hydrogen ionised by photons in the hydrogen ionising frequency bin (13.6 - 24.6 eV).

The optical depth determines how much radiation will be absorbed travelling through a medium. The optical depth of an infinitesimally small path is

$$d\tau = n_{\mathrm{HI}} \bar{\sigma}_{\mathrm{HI}} dl = \frac{dl}{\lambda_{\mathrm{mfp}}}, \tag{2.34}$$

in which λ_{mfp} is the mean free path. From this, one can conclude that the probability of having no interactions along path l is $1 - dl/\lambda_{\text{mfp}} = 1 - d\tau$. Numerically representing the intervals $d\tau$ as $\Delta\tau$ and taking N partitions, we can calculate the PDF of the entire path as

$$P(\tau_\nu) = \lim_{N\to\infty} \left[1 - \frac{\Delta\tau_\nu}{N}\right]^N = e^{-\tau_\nu}. \tag{2.35}$$

This can be understood as the fraction of radiation left after travelling the path N. From this, we can arrive at the CDF, giving the probability for the photon packet to travel a path of optical depth τ_ν

$$F(\tau_\nu) = \int_0^{\tau_\nu} P(\tau')d\tau' = 1 - e^{-\tau_\nu}. \tag{2.36}$$

This can also be understood as the amount of radiation being absorbed. Inverting this equation, we arrive at an expression for the optical depth a photon packet can travel through until it is absorbed $\tau_{\text{abs}} = -\ln(1 - F)$. F can be drawn from a univariate distribution. τ_{abs} can be interpreted as a budget of optical depth a photon packet has to "spend" until it is absorbed. If the injection of photon packets is biased towards lower-luminosity stars, photon packets injected at high-luminosity stars receive a higher optical depth budget. This will be used to track how many Voronoi cells $j \in \{1, ..., m\}$ a photon packet $i \in \{1, ..., n\}$ can travel through until everything is absorbed. This process is performed in the following six steps:

1. Calculate the optical depth for a photon packet i travelling through the cell j it is at the border of (and lying in its path) by Equation (2.33). The length of the path through the cell l^j_{cell} is determined by its direction $\boldsymbol{k}_i$.
2. If the optical depth budget $\tau^j_{\text{abs},i}$ of the photon packet is larger than τ^j_{cell}, then $\tau^{j+1}_{\text{abs}} = \tau^j_{\text{abs},i} - \tau^j_{\text{cell}}$, as some of the budget is spent.
3. Update the position of the photon $\boldsymbol{r}^{j+1}_i = \boldsymbol{r}^j_i + l^j_{\text{cell}}\boldsymbol{k}_i$
4. Repeat steps 1-3 until $\tau^m_{\text{abs},i} \leq \tau^m_{\text{cell}}$, which means that the photon cannot travel through the next cell.
5. If $\tau^m_{\text{abs},i} \leq \tau^m_{\text{cell}}$, the photon is stopped at the border of the cell and will not travel further.

For a more in-depth explanation of how this is implemented in COLT, read Section 3.4.

During this travel, scattering events on dust or electrons can happen, changing the direction $\boldsymbol{k}_i$ and the energy of the photon packet. In the end, the positions, number of scatterings, frequency bins, weights, etc. of the photons will be output into a file, which can be used to determine the escape fractions of photons as predicted by COLT.

2.7 Differences to the SPHINX galaxy formation model

The results obtained using SMUGGLE-RT (Kannan et al., 2020) will be in comparison to the results of Rosdahl et al. (2022), already mentioned in Section 1.3, which use SPHINX (Rosdahl et al., 2018) simulations on the basis of RAMSES-RT (Rosdahl et al., 2013). These simulations are based on RAMSES (Teyssier, 2002), an adaptive mesh-refinement code, which has a cubical octree structure. The galaxy formation model used in their simulations has a few differences to our model, which I want to highlight here.

While the star formation is suppressed in our simulation via early stellar feedback, in Rosdahl et al. (2022), the SN explosion energies are boosted fourfold. To accurately model the Sedov-Taylor phase of SNe, we inject the momentum into the cells in the coupling radius based on a weight. The mass and energy ejected are injected into the cells within the coupling radius based on the weight as well. In SPHINX (Rosdahl et al., 2018), the thermal energy is injected in the host cell of the SN if the resolution is sufficient. Otherwise, momentum is injected. The radial momentum, mass ejected by the SN and gas mass of the host cell is distributed across the host cells and the adjacent cells (including those across the corners). The amount of momentum given to each neighbour depends on a weight based on the mass and a geometrical factor. The momentum injected is increased if a cell contains an unresolved HII region. In an SN explosion, no more than 90% of gas can be removed from a host cell. RAMSES-RT (Rosdahl et al., 2013) does not include dust cooling, which is included in SMUGGLE-RT (Kannan et al., 2020, 2019). While we use an RSLA, RAMSES-RT (Rosdahl et al., 2013) uses a variable speed of light approximation, which is slowest in small grid cells and faster for larger ones. The radiation injected by star particles is injected into cells inside the coupling radius in AREPO-RT (Kannan et al., 2019). In RAMSES-RT (Rosdahl et al., 2013), the radiation is injected only into the host cell. However, a transport step of the M1 radiative transfer is performed right after. SPHINX (Rosdahl et al., 2018) does not allow for molecular hydrogen cooling, while SMUGGLE-RT (Kannan et al., 2020) performs non-equilibrium molecular hydrogen cooling. SPHINX (Rosdahl et al., 2018) sets a base metallicity to enable cooling to low temperatures.

3 Methodology

In this section, I will discuss how to derive the escape fraction in post-processing in three different ways. The first way is using the flux coming from the M1 radiative transfer in AREPO-RT. The second approach is ray-tracing from the centre of the galaxy, utilising the neutral hydrogen density. The third approach is ray-tracing from each star in the galaxy using the COLT code (Smith et al., 2015). I will be starting off by explaining how to derive the luminosity of stars, as this variable is not included in the snapshots of AREPO-RT and is needed for the first way of calculating the escape fraction.

3.1 Interpolating the luminosity of stars

In AREPO-RT the luminosity of a star particle is found by interpolating in a table. In this table, luminosity is given for each frequency bin for multiple different ages and metallicities. The luminosity is given for a star of solar mass. This table is based on the tables produced by the Binary Population and Spectral Synthesis code (BPASS) Eldridge et al. (2017), which gives the luminosity of a stellar population for multiple frequencies. Because we split the frequency of light into multiple frequency bins, as mentioned in Section 2.2, the table was integrated over these frequency bins.

The luminosity I is given as a variable dependent on the frequency ν in the form

$$I = \nu \frac{dL}{d\nu}. \tag{3.1}$$

Here, L is the physical luminosity of a star of one solar mass. For each frequency bin, the luminosity is integrated in 999 steps. First, the stepsize $\Delta\nu$ of the frequency at each of the steps is determined using

$$\Delta\nu = \frac{\nu_1 - \nu_0}{1000 - 1}. \tag{3.2}$$

In this formula, ν_0 is the lowest frequency in the bin, and ν_1 is the highest. For each of the 999 steps, the frequency in the middle of the step is derived

$$\nu_j = \nu_0 + (j + 1/2)\Delta\nu. \tag{3.3}$$

Here, j is the number of the step of the integration being calculated. Next, the luminosity at this frequency is determined. This is done for all ages A and metallicities m found in the table. The luminosity table has certain frequencies for which the luminosity is given. The closest smaller frequency to ν_j will be denoted as $\nu_{\mathrm{tab},i-1}$ and the closest larger frequency as $\nu_{\mathrm{tab},i}$. As the next step, a measure of distance of ν_j to $\nu_{\mathrm{tab},i}$ is derived and normalised over the distance between $\nu_{\mathrm{tab},i-1}$ and $\nu_{\mathrm{tab},i}$

$$D_{\nu,j} = \frac{\nu_j - \nu_{\text{tab},i-1}}{\nu_{\text{tab},i} - \nu_{\text{tab},i-1}}. \tag{3.4}$$

The luminosities found in the table $I_{\text{tab},i}$ are used to derive the luminosity I_j by being weighted by $D_{\nu,j}$ through linear interpolation

$$I_{j,A,m} = (1 - D_{\nu,j}) I_{\text{tab},i-1,A,m} + D_{\nu,j} I_{\text{tab},i,A,m}. \tag{3.5}$$

The weighting is done, such that $I_{\text{tab},i}$ corresponding to the frequency closest to ν_j is making up a higher proportion of $I_{j,A,m}$, while the weights add up to 1.

For each of the ages A and metallicities m, multiple luminosities (one for each j) get derived for each bin. These are converted to the physical luminosity, mentioned in Equation (3.1) and added up

$$L_{\text{bin},j,A,m} = L_{\text{bin},j-1,A,m} + \frac{I_{j,A,m} \cdot \Delta\nu}{\nu_j}. \tag{3.6}$$

This first part of integrating the first table to form a second smaller table is not necessary, as one could interpolate the luminosity of given stars from the original table. However, this is done so by AREPO-RT and for consistency is done in this work as well.

The next step is to interpolate the luminosity $L_\star$ of a single star particle from the table L_{bin}. First, the linear distances Δm and ΔA of the metallicity $m_\star$ and age $A_\star$ of the star from the age A_{tab} and metallicities m_{tab} for which luminosities are given in the table are determined by

$$\Delta m = \frac{m_\star - m_{\text{tab},i}}{m_{\text{tab},i+1} - m_{\text{tab},i}}, \tag{3.7}$$

$$\Delta A = \frac{A_\star - A_{\text{tab},j}}{A_{\text{tab},j+1} - A_{\text{tab},j}}. \tag{3.8}$$

Here, $m_{\text{tab},i}$ is the closest metallicity in the table smaller than $m_\star$ and, hence, $m_{\text{tab},i+1}$ the closest larger metallicity. The age $A_{\text{tab},j}$ is defined similarly.

Lastly, the luminosity from the table is interpolated according to bilinear interpolation

$$\begin{aligned} L_{\star,M_\odot,\text{bin}} = &(1 - \Delta m)(1 - \Delta A) \cdot L_{i,j,\text{bin}} \\ &+ (1 - \Delta m)\Delta A \cdot L_{i,j+1,\text{bin}} \\ &+ \Delta m(1 - \Delta A) \cdot L_{i+1,j,\text{bin}} \\ &+ \Delta m \Delta A \cdot L_{i+1,j+1,\text{bin}}. \end{aligned} \tag{3.9}$$

To get the actual luminosity of the star particle in a frequency bin, it now has to be multiplied by its mass M in solar masses

$$L_{\star,\mathrm{bin}} = L_{\star,M_\odot,\mathrm{bin}} \cdot \frac{M}{M_\odot}. \tag{3.10}$$

3.2 Measuring the escape fraction using fluxes given by the M1 radiative transfer

3.2.1 Measuring the escaping flux of a galaxy

This section will discuss how to find the flux escaping through a spherical shell with some radius r. First, a spherical shell with multiple pixels j of the same size is needed to sample the radially outward pointing component of the flux $F_{\mathrm{rad},j}$ at each of these pixels. This is done by using a HEALPix sphere (Gorski et al., 2005), which is integrated into Python using healpy (Zonca et al., 2019).

Using healpy, a shell is created with $n = 49152$ pixels with its center at coordinate $(0, 0, 0)$ and a radius of 1. Tthe coordinates of the pixels are multiplied by the desired radius. The pixels on this sphere are then shifted, such that the center of this sphere lies in the centre of the galaxy.

To now determine the flux at each of these coordinates, the Voronoi cell in which each pixel lies must be found. This is done by building an Octree over the size of the box of the simulation and using it to find the nearest mesh generating point for each pixel. Once for each pixel, the nearest mesh generating point is found, each pixel gets assigned the flux of this cell $\boldsymbol{F}_j$ (in this case, the flux in the hydrogen ionising frequency band, 13.6 - 24.6 eV). To find the flux flowing out of (or into) the sphere L_{esc} (the escaping luminosity), the flux parallel to the vector from the origin to the coordinate of the centre of each pixel $F_{\mathrm{esc},j}$ has to be found. This is done by taking the unit vector pointing in the direction of each cell $\boldsymbol{s}$ and taking the dot product of the flux density and this unit vector

$$F_{\mathrm{esc},j} = \boldsymbol{F}_j \cdot \boldsymbol{s}. \tag{3.11}$$

Lastly, to get the entire flux flowing out of this region, the size of each pixel A_j is multiplied by its outward-pointing flux $L_{\mathrm{esc},j}$ and this value is then summed up for all the pixels to obtain the escaping luminosity

$$L_{\mathrm{esc}} = \sum_{j=1}^{n} F_{\mathrm{esc},j} \cdot A_j \tag{3.12}$$

This also contains incoming flux from stars lying outside of the virial radius of the galaxy. To what extent this leads to problems when determining the escape fraction will be discussed in Section 4.

3.2.2 Deriving the escape fraction from the integrated flux and the luminosity

This flux can now be used to find the escape fraction f_{esc} out of the sphere by the equation

$$f_{\text{esc,M1}} = \frac{L_{\text{esc}}}{\sum_i^n L_{\star,i}}, \tag{3.13}$$

in which $\sum_i^n L_{\star,i}$ is the sum of luminosities of all star particles $i \in \{1, ..., n\}$ inside the sphere. However, here, the RSLA might lead to problems, as the radiation coming from a star particle might take an amount of time high enough to reach the sphere, such that the luminosity of the star particle has changed significantly. Which in turn would lead to a wrong result for the escape fraction. This can be avoided by approximately correcting the stellar age when calculating the luminosity by the light travel time from the galaxy centre through the formula

$$A_{\text{corr}} = A - \frac{r}{\tilde{c}}. \tag{3.14}$$

3.3 Measuring the escape fraction through ray tracing from the centre of the galaxy

The second method implemented is ray tracing from the centre of the galaxy, using the neutral hydrogen density. I will start with an explanation of how the optical depth is calculated using the variables given in the snapshots and then go on to explain integrating the optical depth to HEALPix shells in order to get the escape fraction.

To derive the optical depth, first, the number density of HI needs to be derived. This is done by the equation

$$n_{\text{HI}} = \frac{\rho_{\text{gas}} w_{\text{H}}}{m_{\text{H}}} X_{\text{HI}}. \tag{3.15}$$

Here ρ_{gas} is the gas density, X_{HI} is the neutral hydrogen number fraction, $m_H = 1.673 \times 10^{-27}$ kg is the mass of a hydrogen atom and $w_H = 0.76$ is the mass fraction of hydrogen in this gas. From this and the hydrogen photoionisation cross-section at the mean wavelength of the hydrogen ionising frequency bin $\bar{\sigma}_{\text{HI}} = 3.30693 \times 10^{-22}$ m^2 the optical depth can be found by the formula

$$\tau_{\text{HI}} = \int_0^L \bar{\sigma}_{\text{HI}} n_{\text{HI}} ds. \tag{3.16}$$

Here L is the length the radiation travels through the medium described by n_{HI}.

To gain insight into what kind of optical depth a photon experiences coming from the centre of the galaxy and reaching the shell on which the flux is measured, the optical depth is determined on multiple shells at different radii and then summed up. For this, a similar tactic as in Section 3.2.1 is used. This aims to integrate the optical depth along the line-of-sight (LoS) j to each HEALPix pixel on a sphere at the virial radius of the galaxy. Each LoS is split up into intervals with a set length Δr, which is set such that it is one-third of the radius of a typical gas cell, assuming the gas cell is spherical. The neutral hydrogen density $n_{\mathrm{HI},i-1/2,j}$ of each interval i is measured in the centre of this to ensure 2nd-order accuracy. In practice, for each radius, $r_{i-1/2}$ at which the neutral hydrogen density is measured, a HEALPix sphere is created, and for each pixel the neutral hydrogen density is determined. The optical depth for each pixel is determined by

$$\tau_{\mathrm{HI},i,j} = \bar{\sigma}_{\mathrm{HI}} n_{\mathrm{HI},i-1/2,j} \Delta r. \tag{3.17}$$

The optical depth of the pixels along one LoS j from the centre of the galaxy are then summed up to gain insight into the optical depth encountered by photons travelling along this path to the outermost shell of radius r_n

$$\tau_{\mathrm{HI},j} = \sum_{i=1}^{n} \tau_{\mathrm{HI},i,j}. \tag{3.18}$$

3.3.1 Optical depth and escape fraction

The optical depth τ can be turned into the fraction of radiation f making it through a medium by the formula

$$f = e^{-\tau}. \tag{3.19}$$

As in this case, the optical depth is the optical depth radiation experienced when leaving the sphere radially, the above formula gives an expression of the escape fraction

$$f_{\mathrm{esc},\tau} = \frac{1}{N} \sum_{j}^{N} e^{-\tau_{\mathrm{HI},j}}, \tag{3.20}$$

in which N is the number of pixels on the HEALPix sphere.

3.4 Measuring the escape fraction by ray tracing from each star particle using COLT

To derive the escape fraction using the Monte Carlo method implemented in COLT[1] (Smith et al., 2015) weights $\omega_{\mathrm{S},i}$ and ω_i are assigned to each photon packet. The source weights ω_{S} are calculated, such that $\sum_i \omega_{\mathrm{S},i} = 1$ and all photon packets emitted from one star have the same source weight. In the case

[1]COLT is only used to determine the escape fraction in this thesis. Although COLT has functionalities to equilibrium ionise the gas, this is not used here. Instead, the non-equilibrium ionisation computed by SMUGGLE-RT is used.

of an unbiased injection of photon packets explained in Section 2.6, all photon packets have the same source weight $\omega_S = 1/n$, in which n is the number of photon packets. In the case of a biased injection of photon packets, the source weight is biased by β as well to ensure a correct escape fraction in the end. The source weight of a star $\omega_{S,*}$ is then defined as

$$\omega_{S,*} = \frac{1}{n}\left(\frac{L_*^{1-\beta}\sum_* L_*^{\beta}}{\sum_* L_*}\right), \tag{3.21}$$

where L_* is the luminosity of the star. Initially, the weight of the photon packet ω_i is set to the source weight of the star it is injected at, such that - in the biased case - photon packets coming from more luminous stars have higher initial weights and, as such, also higher optical depth budgets. In the unbiased case, all photon packets get the same source weight.

The optical depth budget is implemented, such that the initial weight ω_i^0 gives the photon packet an initial "optical depth" τ_i^0, as

$$\omega_i^0 = e^{-\tau_i^0}. \tag{3.22}$$

Every time the photon packet traverses a cell, the optical depth of this cell as described in Section 2.6 is "added" onto the initial optical depth of the photon packet by

$$\omega_i^{j+1} = e^{-\tau_i^j} e^{-\tau_{cell}^j} = e^{-(\tau_i^j + \tau_{cell}^j)}. \tag{3.23}$$

The photon packet is completely absorbed, i.e. the optical depth budget is used up when the weight of the photon packet reaches 10^{-14}.

A maximal radius is set in COLT at which the photon packets are stopped to gain insight into the escape fraction at a certain radius from a star or a galaxy. When a photon is stopped at this radii, it is not stopped at a cell boundary but has travelled a distance l into a new cell. The optical depth $\tau_{\text{end}} = n_{\text{HI}}\sigma_{\text{HI}} l$ through this cell needs to be subtracted from the optical depth budget as well. If a photon packet is stopped before the maximal radius is reached, it gets assigned the weight $\omega_i = 0$ as all radiation was absorbed. The final escape fraction can be found by summing up all weights

$$f_{\text{esc, COLT}} = \sum_i \omega_i. \tag{3.24}$$

Additionally, the escape fraction of single stars $f_{*,\text{ esc, MC}}$ can be determined by weighting the photon weights of the photon packets associated with this star $\omega_{*,i}$ with the source weight of the star $\omega_{*,S}$ as

$$f_{*,\text{ esc, COLT}} = \frac{\sum_i \omega_{*,i}}{\sum_i \omega_{*,S}}. \tag{3.25}$$

4 Comparison of escape fraction measurements

In this section, I will compare the three methods of determining the escape fraction detailed in Section 3 and explore the advantages and disadvantages of each method. The first method utilises the M1 flux and determines the escape fraction through the radially outward/inward pointing flux on a HEALPix sphere at the virial radius of a galaxy. The second method conducts ray-tracing along the LoS of the centre of a sphere towards the pixels on a HEALPix sphere. The third method uses the COLT code and ray traces photon packets from stars towards the virial radius. Each of these methods uses the gas properties as computed by SMUGGLE-RT.

First, I want to highlight the connection between the M1 flux pointing radially out of a sphere and the optical depth of a LoS, which is important in the second approach. A high optical depth along a LoS from a star towards the virial radius leads to efficient absorption of radiation along that LOS. The resulting flux measured at the virial radius should, hence, be quite low if a high optical depth is present and conversely high if the optical depth is low.

In Figure 4 in the top panel, you can see a Mollweide projection of the radially outward pointing (i.e. positive) flux on a HEALPix sphere. This sphere is placed at the virial radius of a halo. The flux is given in photons per second per pixel of the HEALPix sphere. In the bottom panel, you can see a similar Mollweide projection of the LoS optical depth of that pixel from the centre of the galaxy. The optical depth is given as its logarithm. Every time log is used in this thesis, it is shorthand for $\log_{10}$. While the optical depth is quite high for the largest part of this halo, there is a region visible, in which the optical depth is pretty low. This is the only path in this halo from which radiation can escape at this moment. As you can see in the flux plot, this is actually the only part which has an outward-pointing flux. This path was most likely formed through feedback, which ejected some of the neutral hydrogen in this direction.

It should be noted that in many cases, the optical depth and the M1 flux out of the sphere, measured in the way they were here, will not align this nicely. If the stars are not located in the centre of the halo, they do not see the same optical depth out of the halo as the measurement of the optical depth. Therefore, their radiation might escape more easily (if they lie in regions of low optical depth towards the virial radius) or not as easily (if they lie in very dense regions of neutral hydrogen). Additionally, due to the nature of the M1 radiative transfer, some flux coming from a source outside of the halo might lead to a negative flux measurement instead of radiation being able to escape, and the radiation might flow into regions where one would expect a shadow.

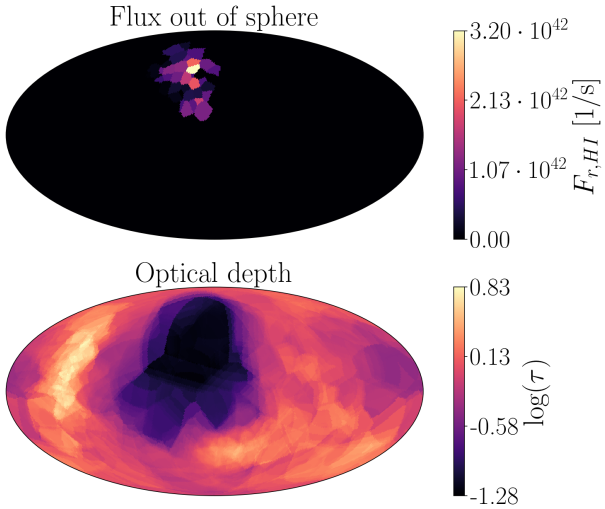

Figure 4: Mollweide projections of HEALPix spheres. The top panel shows the radially outward pointing M1 flux of a halo. The bottom panel shows the logarithmic LoS optical depth of each of the pixels of the HEALPix sphere of the same halo.

To compare how the three different methods compare over multiple distances, a somewhat isolated halo with only one star particle in its centre was chosen. In Figure 5, you can see a slice of the neutral hydrogen fraction of the halo. Overplotted on this slice, you can see white stars with black edges, which show the position of star particles close to this slice. The dark blue arrows show the effective flux velocity of the Lyman-Continuum frequency bin (13.6 - 24.6 eV). The effective velocity is derived by dividing the flux by the photon density and is used to show the direction but not the magnitude of the flux. The green circle shows the radius of 100 ckpc/h away from the centre of the halo. The x and y axes are centred on the centre of this halo. The flux points away from the star in the centre of the halo, as one would expect. However, further out from the star, there is flux coming from external sources pointing inward. This can be seen both on the bottom of the slice and the top right.

To see how the methods of determining the escape fraction differ with increasing radius for this relatively simple halo, you can see a plot of the escape fraction versus the radius in Figure 6. The grey line is the escape fraction determined by using the M1 flux. The turquoise line shows the escape fraction determined by ray tracing from the centre of the halo. The red-dotted line shows the escape fraction determined by ray tracing from each star inside the halo using COLT.

While both of the ray-tracing approaches agree very well, the approach using the M1 flux deviates greatly at small radii and a bit at larger radii. The deviation at smaller radii is due to how the radiation is injected. It is not injected directly into the gas cell in which the star particle lies, as this would lead to

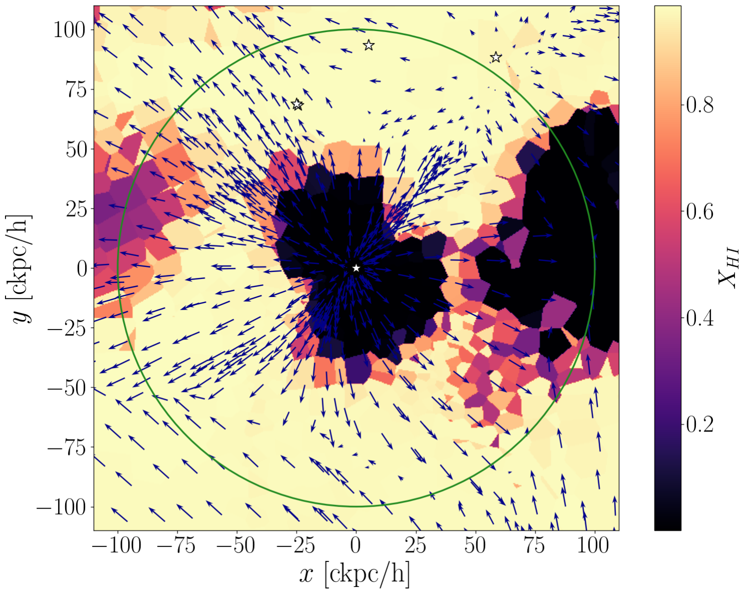

Figure 5: Slice of the neutral hydrogen fraction. The x and y axes are given in comoving kpc/h and are centred on the centre of the halo. The white stars with the black edges are star particles in the simulation. The dark blue arrows show the effective radiation velocity of the Lyman-Continuum frequency bin. The effective velocity is the photon flux divided by the photon density. The green circle shows a radius of 100 ckpc/h.

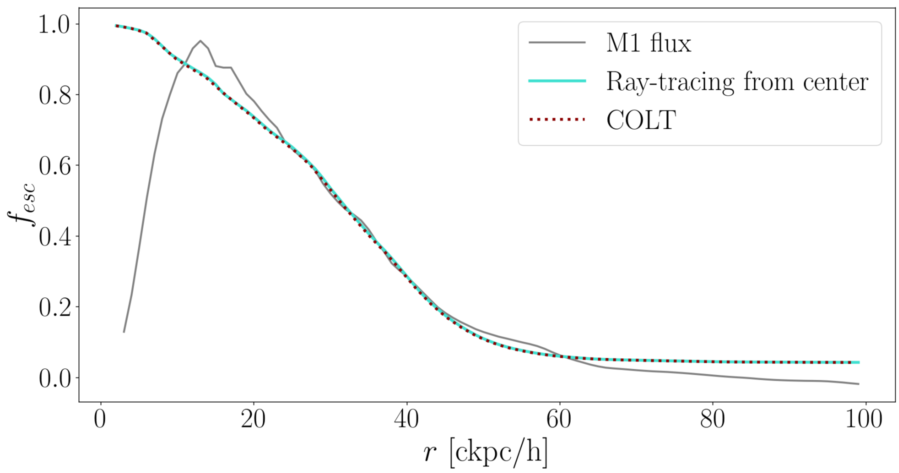

Figure 6: Escape fraction versus the radius, given in ckpc/h. The grey line shows the escape fraction determined by the M1 flux. The turquoise line shows the flux determined by ray tracing from the centre of the halo. The red dotted line shows the flux determined by ray tracing from each star using COLT.

a not quite spherically symmetric propagation of the radiation outward due to the nature of the M1 radiative transfer and the cell geometry. The radiation is instead injected into the 16 closest cells to the star. This means that right at the star, only a fraction of the total flux is injected, leading to a low escape fraction until about 17 ckpc/h in this example. At slightly higher radii until about 21 ckpc/h, the escape fraction is too high, as there is still flux injected into these cells, leading to some radiation propagating outward, which would usually not reach radii this high before being absorbed. The low escape fraction at radii bigger than 60 ckpc/h is due to the inflowing (”negative”) flux from external sources as shown in Figure 5. The nature of the M1 radiative transfer leads to interesting effects when the flux of two or more sources of radiation intersects. It can cause a change in direction, which appears rather unphysical as radiation is usually not collisional, or even inverts its direction when ”colliding” with radiation of a different source. Instead of flowing radially outward from each source, the radiation moves perpendicularly to the line connecting the two sources. This effect could be removed when external sources are deactivated, and the radiation travels outward in a static state of the gas. However, this does not remove the effects close to the area of injection, and there are some other effects this will not fix. The M1 radiative transfer will fail to form sharp shadows behind objects; instead of stopping the radiation, it rather flows around these objects. Additionally, as the radiation is injected at certain timesteps and diffuses out over the rest of the time, some fluctuations can show up in the escape fraction measurements, dependent on how close to the injection of radiation the snapshot was taken. This can also be visible over distance, not just time. As an RSLA is used, the light travel time from the star particle to the virial radius was corrected as mentioned in Section 3.2.2. However, this assumes that the star particle is located in the centre of the galaxy, so this is only an approximate correction. The many arguments against using the M1 flux approach to determine the escape fractions convinced me to reject this as a method of determining the escape fraction in the further analyses of this thesis.

The almost identical progression of the escape fraction for both ray tracing approaches in Figure 6 is simply due to the one bright/young star particle in the halo lying right in the centre of it. Hence, both of these approaches are essentially doing the same thing. However, this changes quite drastically when the star particles are no longer situated right in the centre.

In Figure 7, you can see a volume-weighted projection of the gas number density of a halo. The coloured stars plotted on top of it are the star particles lying inside the halo, which are younger than 10 Myr. Their colour shows their escape fraction. There are two reasons for (exclusively) plotting young stars here. The first reason is that it shows where the stars form inside a halo. The second reason is that young stars are the brightest stars in the ionising UV by several orders of magnitudes in such a halo and, hence, also dominate the escaping luminosity. While the younger star particles in this galaxy have luminosities of up to 10^{50} s^{-1}, the older star particles have luminosities lower than 10^{48} s^{-1}. You

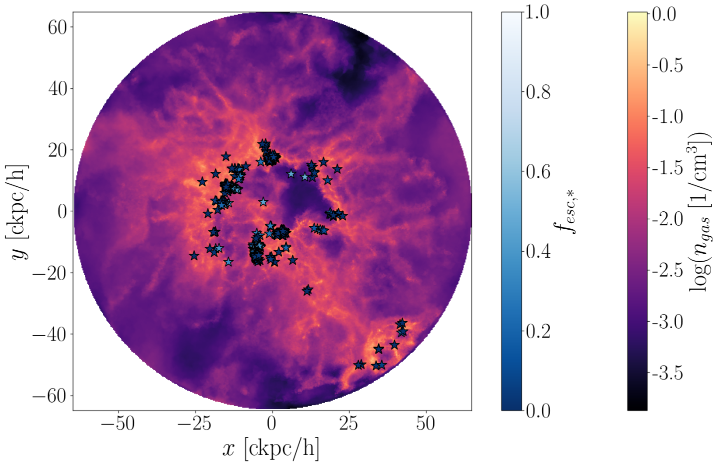

Figure 7: Volume-weighted projection of the gas number density of a halo. The stars are the locations of the star particles in this halo, which are younger than 10 Myr. Their colour shows their escape fraction.

can see that most of the star particles are, in this case, not formed in the centre of the halo but instead in dense regions 10-20 ckpc/h displaced from the centre. The underdense region formed in the centre of this halo is a bubble formed by stellar and supernova feedback, blowing the gas outwards. This is an example of positive feedback (Efstathiou, 2000; Silk, 2013), in which the density of the gas is increased and star formation is facilitated in the swept-up gas surrounding the bubble. The escape fraction of these young stars is quite low due to the high gas density and, hence, the high neutral hydrogen density surrounding them.

In Figure 8, you can see two slices of the neutral hydrogen density n_{HI} of a halo. In Figure 8 a) (left panel), the dots shown are positioned at the coordinates of HEALPix pixels (used for determining the escape fraction by ray tracing from the centre of the halo) close to the z coordinate of the slice. In Figure 8 b) (right panel), the dots shown are photon packets of the COLT code close to the z coordinate of the slice. Here, you can see that some photon packets that have used up their optical depth budget before reaching the maximal radius have been stopped at cell boundaries. Other photon packets that made it to the virial radius have rather low escape fractions, as they traversed a large optical depth.

When looking at a), you can see the pixels with a high escape fraction lie in regions with a low, neutral hydrogen column density along the LoS from the centre of the halo. In b) this is not the case. Almost all photon packets have a low escape fraction. As previously mentioned, this is due to the position of the young stars not being in the centre of the halo. Additionally, as the direction of the photon packets is randomly drawn in COLT, some of the photon packets visible might stem from stars above or below the plane of the slice, which yields results less correlated with the density in the slice than ray-tracing from the halo centre.

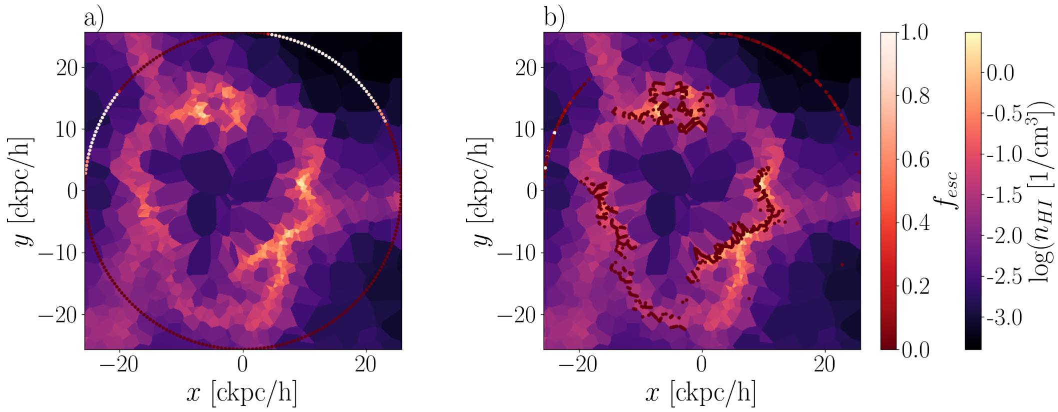

Figure 8: Slices of the neutral hydrogen number density in log scale. The dots in a) are pixels of the HEALPix sphere used for the ray tracing from the centre of the galaxy close to the z-component of the slice. The colour shows the escape fraction through one of these pixels. In b) the dots are photon packets of the COLT approach. The colour shows the escape fraction of each photon packet.

Using the M1 flux to determine the escape fraction has many disadvantages over the other methods due to the biases and artefacts caused by the flux from external sources, injection and time-stepping. This approach will, hence, not be used in further analyses in this thesis. The ray tracing from the centre approach is relatively slow due to the small distances at which the optical depth needs to be determined to get an accurate result. The main disadvantage, however, is the assumption that all the bright stars can be found in the centre of the halo, as this is only true for a fraction of the halos in our simulation. Although COLT requires some postprocessing of the snapshots in order to give the correct results, it is pretty fast through its parallelised code and yields the most reliable results. For further analyses in this thesis, COLT will be used to determine the escape fractions.

5 Escape fractions and correlations of galaxy properties in simulations

5.1 Time evolution of escape fractions

The escape fraction has a tight relationship with the stellar and SN feedback, as less dense gas inside the ISM enables radiation to escape more easily without getting absorbed. Due to this, one would assume the escape fraction is higher at times or directly after times with a higher SFR, as more young stars produce more (early) stellar feedback and, soon thereafter, SN feedback. To gain some insight into this relation, the zoom-in simulation of the medium group was used, which has a zoom factor of 4. This group has a virial mass of 4.74×10^{10} $M_{\odot}$ at redshift 4.57. The SFR in Figures 9 to 16 is defined using the mass of stars younger than 10 Myr inside of the virial radius of the halo. The virial radius of the halo is found through the FoF groups of each snapshot.

To check if the escape fraction is actually linked to the SFR, in Figure 9, the escape fraction f_{esc} is plotted in blue and the SFR in grey versus the redshift. For this plot, the galaxy corresponding to the largest FoF group in the high-resolution region of the medium group was followed over time. This was made possible using the merger tree feature of the Subfind code (Springel et al., 2021). In this figure, you can see that the escape fraction and the SFR seem to correlate, especially for the two peaks after redshift 6. It also can be seen that the escape fraction peaks are often slightly shifted towards lower redshifts in comparison to the peaks of the SFR. As stellar feedback takes a while to reduce the density of the ISM, and SNe take a while before they go off, the escape fraction increases slightly later than the SFR in the galaxy.

In Figure 10, the SFR and escape fraction shown in Figure 9 are displayed in a scatter plot. Here, the suspected correlation is clearly visible. The higher the SFR is, the higher the escape fraction. The scatter in this plot is due to effects like the previously mentioned lag in time between the high SFR and escape fraction, but also because a high SFR does not have quite the same result every time, dependent on the gas mass and ionisation of the ISM. If more of the hydrogen in the ISM is ionised, less gas has to be ejected by feedback to get high escape fractions. If the gas has a high density (and low ionisation fraction), more feedback must be injected to affect the escape fraction significantly.

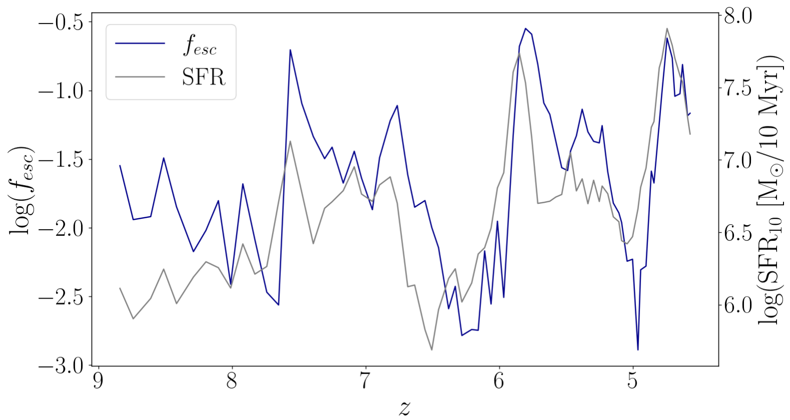

Figure 9: Escape fraction determined by the COLT code in dark blue and the star formation rate of the past 10 Myr in grey versus the redshift for one galaxy. The halo used here is the largest halo found in the high-resolution region of the resimulation of the medium group, which has a virial mass of 4.74 $\times 10^{10}$ $\mathrm{M}_\odot$ at redshift 4.57. Peaks in the escape fraction often follow peaks in the star formation rate.

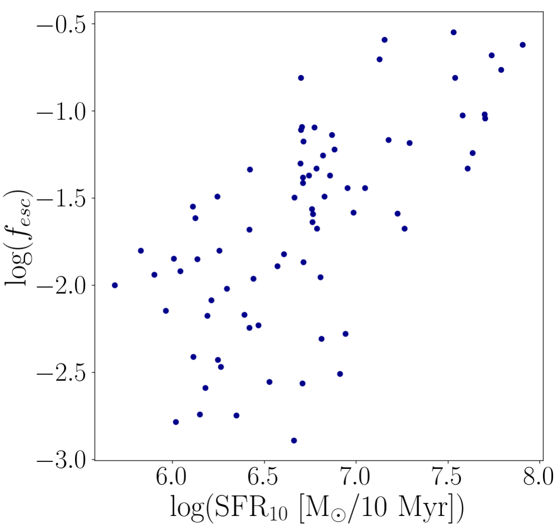

Figure 10: Scatter plot of the escape fraction versus the star formation rate in the previous 10 Myr for a single galaxy. The different points are taken at different times for the same galaxy. The data of this halo is measured between redshifts 10.3 and 4.6. The haloes were taken from the high-resolution region of the resimulation of the medium group, which has a virial mass of 4.74 $\times 10^{10}$ $\mathrm{M}_\odot$ at redshift 4.57.

5.2 Correlation between escape fractions and star formation

To test the effect of the SFR on the escape fraction statistically over a larger sample of data, the 10 largest haloes (FoF groups) for each snapshot of the zoom-in simulation of the medium group are considered in the following analysis. This selection has to be made, because COLT requires pre-processing for each halo. Only haloes completely in the high-resolution region of the snapshot are considered. The snapshots are split up into six bins based on their redshift: [11, 15), [9, 11), [8, 9), [7, 8), [6, 7), and [4, 6).

In Figure 11, one can see the escape fraction f_{esc} plotted versus the SFR for the data as explained above. The colour of the points shows the stellar mass inside the halo. The arrows indicate galaxies with escape fractions below 10^{-5}. The grey line shows the luminosity-weighted escape fraction for 10 bins, while only bins containing five or more data points are shown. The mean escape fraction shown in this line is luminosity-weighted, as galaxies with a higher intrinsic luminosity with high escape fractions have a higher contribution to the reionisation of the IGM than galaxies which are dim. The data follows a positive correlation for all six panels, meaning that haloes with a higher SFR have a higher escape fraction. In the higher redshift intervals, the data is quite spread out, and the positive trend is not as strong as for lower redshifts and is primarily present at high SFR. Additionally, fewer data points are visible in the panels of the higher redshift intervals due to fewer snapshots taken in these periods. The lines showing the luminosity-weighted mean escape fraction also do not show a clear positive trend in the bottom two panels due to the scarcity of data. The escape fraction of the halos becomes larger over time. While the halo with the highest escape fraction in the time frame between redshifts 4 and 6 is about 0.4, the largest escape fraction for the time frame between redshifts 11 and 15 is 0.1. A more detailed analysis of the escape fraction as a function of redshift is conducted later in Section 5.3. When investigating the colour of the points, a correlation of the escape fraction with the stellar mass is also visible. The higher the mass, the higher the escape fraction. However, a few halos with high stellar masses have a low escape fraction; these have a lower SFR than their high escape fraction counterparts.

The positive correlation between the escape fraction and the SFRs hinted at in the analysis of a single halo, was also found in this analysis with a larger dataset. This was expected as the stellar and SN feedback becomes more efficient in times of high star formation, as more young stars can inject more feedback. Additionally, higher escape fractions at later times hint at a more ionised universe, making the escape of radiation from galaxies easier, as less neutral hydrogen is present. However, for the most massive haloes at later times, one would expect a lower escape fraction, as a deeper potential well and higher gas mass withstand a higher degree of feedback. This effect, however, cannot be seen in our simulation. This means that even for the largest galaxies in our sample, the feedback is always strong enough to boost the escape fraction. The few galaxies with very high stellar masses but lower escape fractions also show a lower SFR, falling at roughly the same spot as lower-mass galaxies with a similar SFR.

To investigate the relationship between stellar mass and escape fraction in more detail and check for possible badly resolved haloes, the escape fraction $f_{\rm esc}$ versus the stellar mass inside the halo M_* is shown in Figure 12. The arrows indicate galaxies with escape fractions below 10^{-5}. The number of gas cells inside the virial radius of the halo is shown as the colour of the points. The colour bar is centred on 1000 cells, as this was chosen as a cutoff for a sufficient gas resolution of the halo. In SMUGGLE-RT, the radiation is injected in the 16 closest cells to a star particle; the ionisation fraction of the gas in these cells will not be accurate. As seen earlier, the star particles might not form in the centre of the halo but rather further out. If that is the case, these injection regions might cover a large part of the ISM in haloes with less than 1000 cells. This might then lead to escape fractions which are too high, as the photons traverse a higher ionised gas, than realistic. The grey lines show the luminosity-weighted mean escape fraction for 10 stellar mass bins, while only bins with more than four objects are shown. The dark blue dashed line is a fit to the data of Rosdahl et al. (2022), displayed as a similar blue dashed line in their figure 9. This line is a fit to their luminosity-weighted mean escape fraction calculated for several stellar mass bins.

For all the redshift ranges lower than 11, the escape fraction positively correlates with the mass, as already suspected from Figure 11. In the redshift interval from redshifts 11 to 15 in Figure 12, the luminosity-weighted mean escape fraction, as well as the data itself, hints at a negative correlation at low stellar masses, although there is a lot of scatter in the data and many galaxies with stellar masses lower than 10^5 $\mathrm{M}_\odot$ may be affected by the numerical resolution. The stellar mass of the haloes increases with decreasing redshifts. In the redshift range from 4 to 6, one can see some data points at stellar masses around 10^9 $\mathrm{M}_\odot$, which have quite low escape fractions. This most likely is one halo sampled over several snapshots in this redshift range. This halo is also visible in Figure 11, showing very high stellar masses but a lower escape fraction and star formation rate than other haloes with similar stellar masses. For higher redshift bins in Figure 12, the escape fractions of haloes with stellar masses lower than $10^{5.5}$ $\mathrm{M}_\odot$ seem to increase again with decreasing mass, forming a minimum at about this point. The general positive trend between stellar masses of $10^{5.5}$ $\mathrm{M}_\odot$ and 10^8 $\mathrm{M}_\odot$ indicates that feedback becomes more efficient in a galaxy with increasing stellar mass. For haloes with stellar masses below $10^{5.5}$ $\mathrm{M}_\odot$, the escape fraction appears to be increasing towards lower stellar masses. As these galaxies most likely have low gas masses, their escape fraction can potentially be affected by insufficient resolution. This is confirmed for some haloes, based on the number of gas cells inside their virial radius. This low number of gas cells is likely caused by efficient feedback. If these galaxies have rather low halo masses, they could be heavily affected by feedback and photoevaporation and might lie below the filtering mass. However, this cannot be concluded here, as the stellar mass

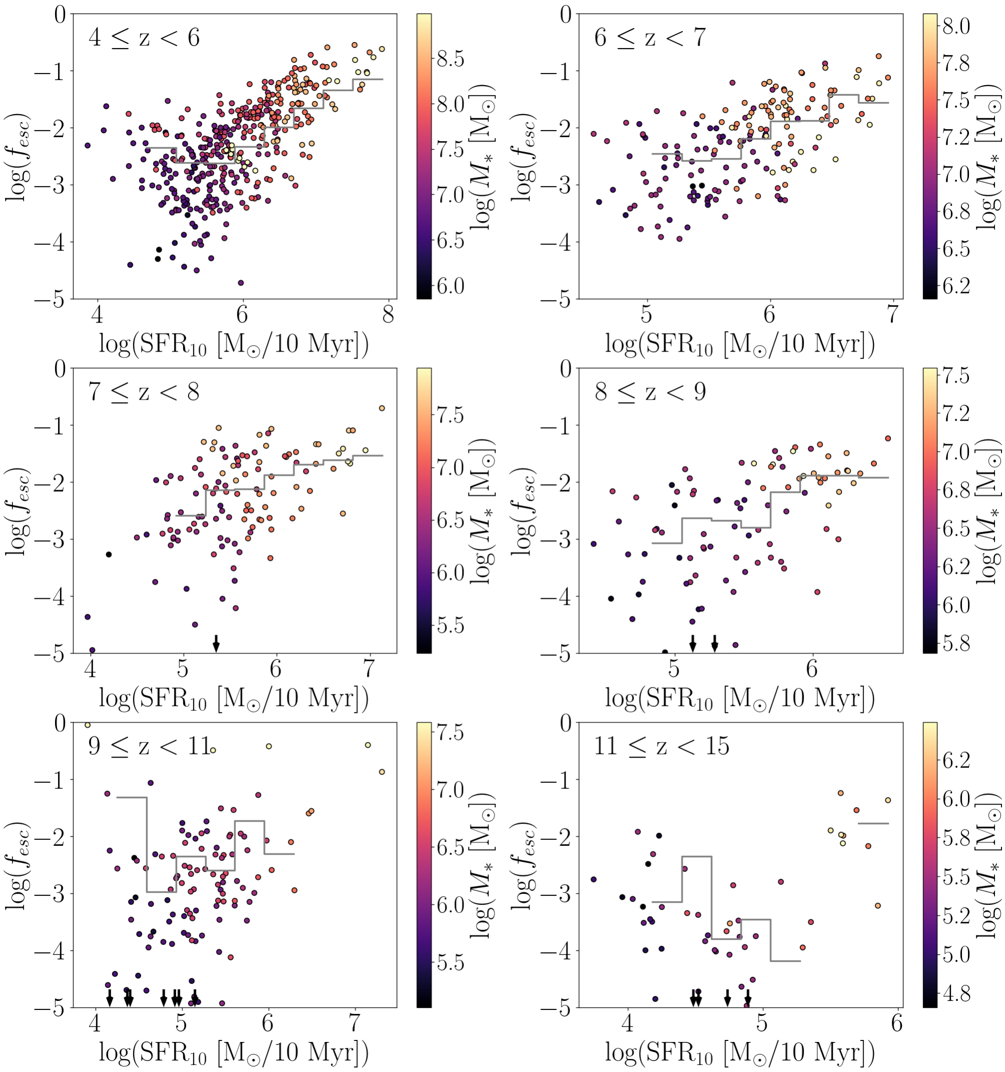

Figure 11: Escape fraction versus the star formation rate of the last 10 Myr for six different redshift ranges. The stellar mass of a galaxy is indicated by the colour of the points. The arrows indicate galaxies with escape fractions below 10^{-5}. The grey lines show the luminosity-weighted mean escape fraction for 10 star formation rate bins, while only bins with five or more data points are shown. Each data point is based on one of the 10 largest halos of one of the snapshots in the redshift range shown in the upper left corner of the panels. The haloes were taken from the high-resolution region of the resimulation of the medium group, which has a virial mass of 4.74 $\times 10^{10}$ M$_\odot$ at redshift 4.57.

is not a good proxy of halo mass. One can still find haloes with more than 1000 gas cells, with high escape fractions at low masses.

Two projections of the gas density of two of such galaxies are shown in Figure A.1 and Figure A.2. The first plot displays a volume-weighted number density projection of a galaxy with a gas cell count of over 1000. In this case, you can see that the high escape fraction stems from the star particles lying in regions with a low gas density. Most of the gas cells seem to lie in the top left corner, where a gas clump is entering the galaxy, which has otherwise a rather low gas density. Possibly in the past, the stars in this galaxy have ejected most of its gas, enabling a high escape fraction. When investigating the surrounding area, it became evident that the gas clump visible in the top left corner and one in the bottom right corner are travelling along filaments and are currently accreting onto the halo. The other haloes containing more than 1000 gas cells often show similar states as the one displayed here. The star particles still lie in low-density regions, while another region of the galaxy is accreting gas. In the second plot, you can see a halo with less than 1000 gas cells (Figure A.2). The one star particle visible in this galaxy lies in a region with a very low resolution and gas density, making the escape of the radiation easy. It becomes apparent that while these galaxies have very high escape fractions at low stellar masses, the stars inside of these galaxies are rather old, which indicates a low escaping luminosity.

The fits from Rosdahl et al. (2022) exhibit a maximum at around 10^7 $M_\odot$ which cannot be found in the data of our simulation of the medium group in Figure 12. Their fit shows a decline in escape fraction towards high stellar masses, which is not present in our data. This decline would indicate that heavier galaxies containing large amounts of stars cannot inject enough feedback anymore to have as high escape fractions as their lower mass counterparts. In the interval from redshift 11 to 15, Rosdahl et al. (2022) find very low escape fractions at low stellar masses and an increase towards higher stellar masses, while the opposite is the case in my analysis at low stellar masses. For stellar masses higher than $10^{5.5}$ $M_\odot$ we find an increase of escape fraction with stellar mass. In our simulation, some of the galaxies in the highest redshift interval have poor resolution. The comparison of the resolution is not trivial in this case, as Rosdahl et al. (2022) use an active mesh refinement code. However, they do mention that their minimum gas cell width is 10 pc. For our simulations, the minimum gas cell width, assuming spherical cells, is 1.2 pc. This might indicate that these small galaxies are not sufficiently resolved in their simulation as well, leading to these rather low escape fractions. For the other panels, the slope to the left of the maximum of the fit from Rosdahl et al. (2022) seems more aligned with the fit to our data. The selection function of the galaxies considered in our analysis differs from theirs. While Rosdahl et al. (2022) conduct a full box simulation, I am considering the 10 largest haloes in the high-resolution region of a zoom-in simulation of a galaxy found in THESAN.

As seen in Figure 11, the mass correlates with the escape fraction and the SFR, as the SFR is the stellar mass of stars younger than 10 Myr (in this case). Similar

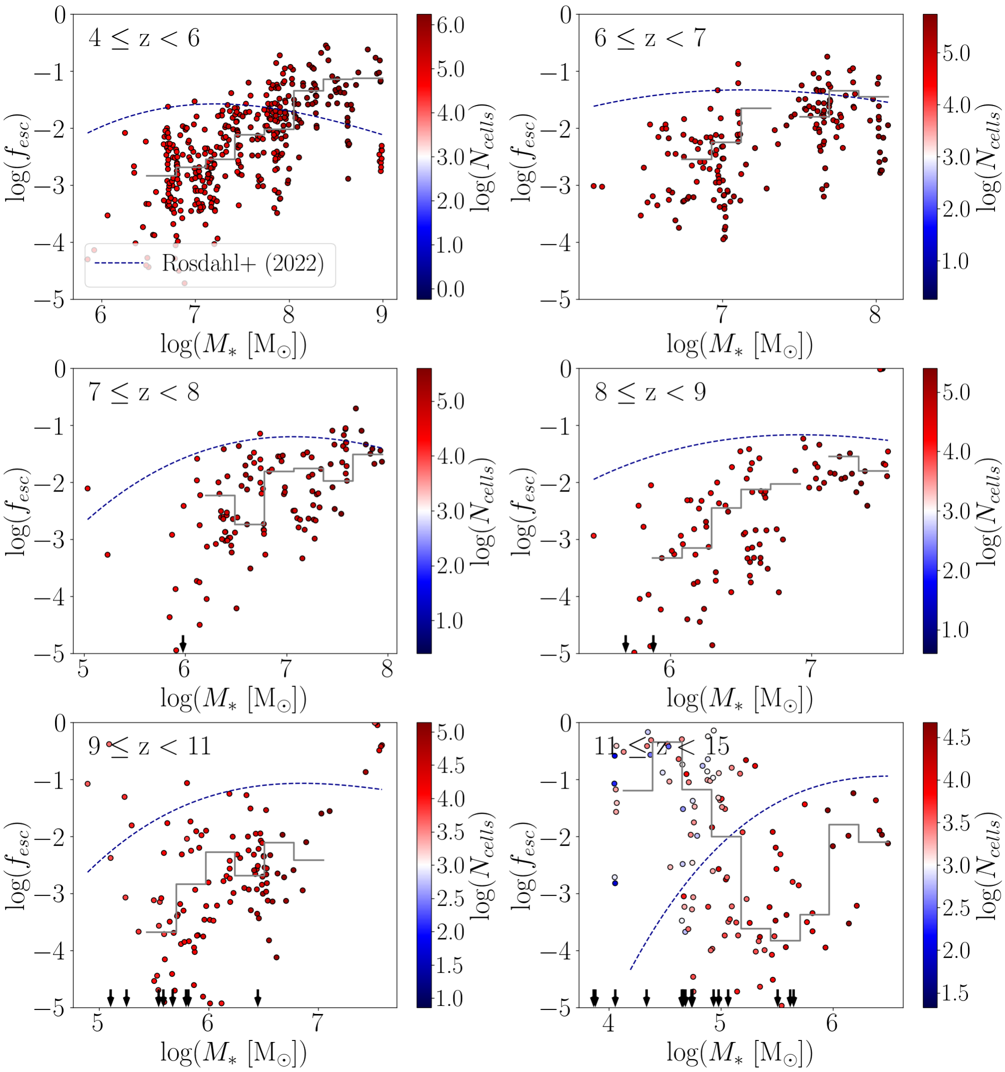

Figure 12: Escape fraction versus stellar mass for six different redshift ranges. The number of gas cells inside the virial radius of each galaxy is indicated by the colour of the points. The arrows indicate galaxies with escape fractions below 10^{-5}. The grey lines show the luminosity-weighted mean escape fraction for 10 stellar mass bins, while only bins with five or more data points are shown. The dashed dark blue line is a fit to the luminosity-weighted mean escape fraction of the data of Rosdahl et al. (2022), which can be seen in their figure 9. Each data point is based on one of the 10 largest halos of one of the snapshots in the redshift range shown in the upper left corner of the panels. The haloes were taken from the high-resolution region of the resimulation of the medium group.

plots with the sSFR were made to see how the feedback injection influences the escape fraction regardless of stellar mass, possibly removing the effects of galaxy mass. Here, the sSFR is the SFR averaged over 10 Myr divided by the stellar mass of the halo. In Figure 13, the escape fraction is plotted against the sSFR. The arrows indicate galaxies with escape fractions below 10^{-5}. The grey line again shows the luminosity-weighted mean escape fraction for 10 sSFR bins, while only bins with five or more objects are shown. The dashed dark blue line is a fit to luminosity-weighted escape fraction over multiple sSFR bins of the data of Rosdahl et al. (2022). This fit is shown in their figure 11 as a similar dashed blue line. The luminosity-weighted mean escape fraction appears to be increasing in the top two panels and rather flat in the other ones. The scatter of the data is still quite high. The colour of the points shows the stellar mass of the halo.

These results show that the mass of stars formed per time per galaxy stellar mass does not correlate significantly with the escape fraction in our simulation in most redshift intervals. Part of the motivation for utilising the sSFR was to try and account for the different strengths of feedback needed for galaxies of different masses to form channels through which the radiation can escape. This, however, does not appear to work in practice. The wide distribution of the data points makes seeing more subtle effects in these plots difficult. The stellar mass in these plots only correlates with the escape fraction and not the sSFR. The fits by Rosdahl et al. (2022) lie at similar escape fractions in comparison to the luminosity-weighted bins derived here in the upper two panels. In the other panels, the scarcity of data and the large scatter make drawing conclusions hard. Additionally, Rosdahl et al. (2022) find a minimum at around 10 Gyr^{-1}, which cannot be seen in the data of our medium group. To assess if such small features can be found, a more extensive analysis of galaxies with a broader range of masses needs to be conducted.

The escape fraction is not only influenced by stars formed in the last 10 Myr, even if those provide the most recent injection of feedback into the ISM. Even before that, periods of high SFR might have ejected gas and made the ISM less dense. Due to this, Rosdahl et al. (2022) suggested using the maximum sSFR - $\mathrm{sSFR}_{10,\mathrm{max}}$. This measure is based on the sSFR for the intervals of [50, 40) Myr, [40, 30) Myr, [30, 20) Myr, [20, 10) Myr, and [10, 0) Myr before the snapshot. It adopts the maximum of the five calculated values of the sSFR.

Plots of the escape fraction f_{esc} versus the maximum sSFR defined as described in the last paragraph can be seen in Figure 14. The arrows indicate galaxies with escape fractions below 10^{-5}. The grey line again shows the luminosity-weighted mean escape fraction for 10 maximum sSFR bins, while only bins with five or more objects are shown. The dashed dark blue line is a fit to the luminosity-weighted mean escape fraction for multiple maximum sSFR bins of the data of Rosdahl et al. (2022). The fits are shown in their figure 15 as similar blue dotted lines. More data points are shown at lower maximum sSFRs in comparison to Figure 13. Some haloes might not have formed stars in the past

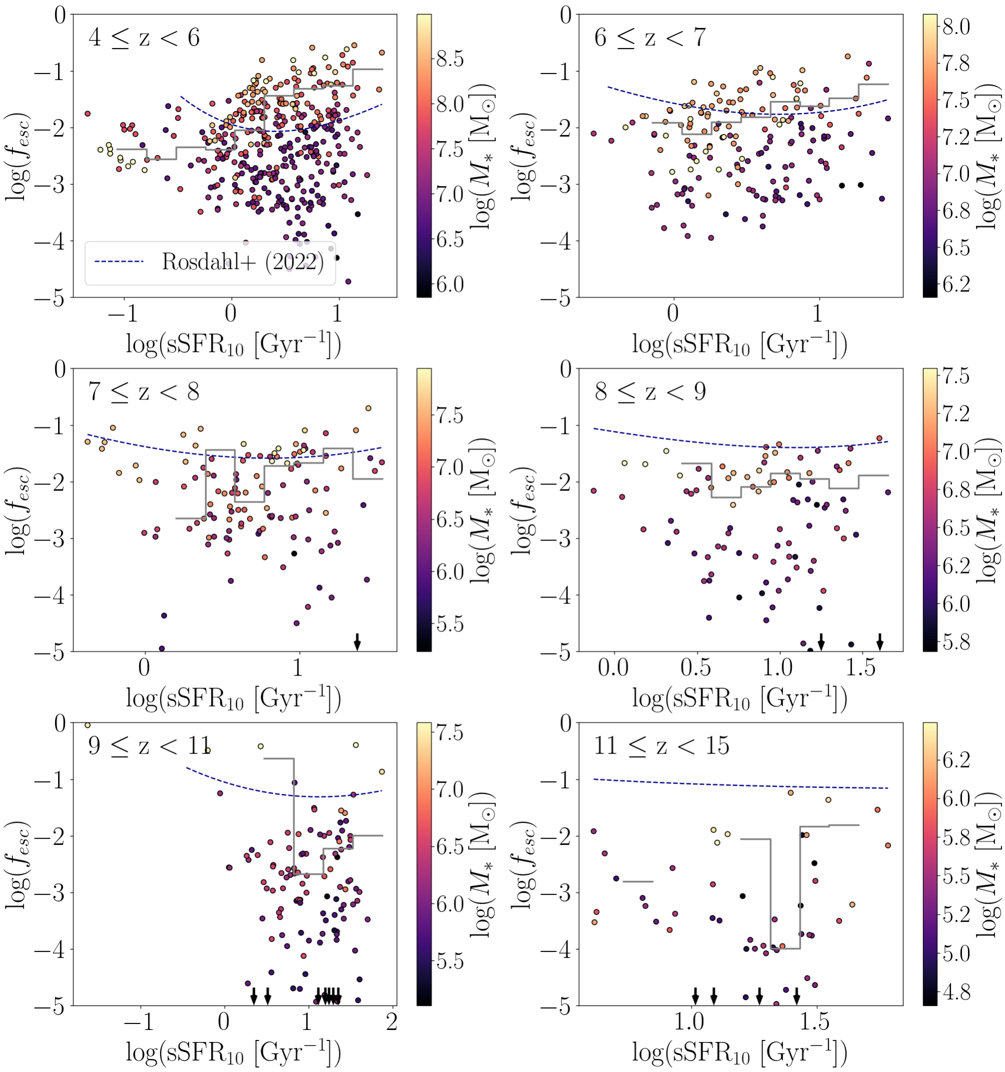

Figure 13: Escape fraction versus specific star formation rate over 10 Myr for six different redshift ranges. The stellar mass of a galaxy is indicated by the colour of the points. The arrows indicate galaxies with escape fractions below 10^{-5}. The grey lines show the luminosity-weighted mean escape fraction for 10 specific star formation rate bins, while only bins with five or more data points are shown. The dashed dark blue line is a fit to the luminosity-weighted mean escape fraction of the data of Rosdahl et al. (2022), which can be seen in their figure 11. Each data point is based on one of the 10 largest halos of one of the snapshots in the redshift range shown in the upper left corner of the panels. The haloes were taken from the high-resolution region of the resimulation of the medium group.

10 Myr; these do not show up in the sSFR plot in Figure 13. These same haloes might have formed stars in the last 50 Myr. Although a positive trend seems to have formed in most panels in Figure 14, the data is still very spread out, and the luminosity-weighted medium escape fraction may be affected by the sample size. The colour of the points again shows the stellar mass, which does not (obviously) correlate with the maximum sSFR over 50 Myr.

While Rosdahl et al. (2022) have fitted a curve to the escape fractions as a function of maximum sSFR and found a minimum, the same cannot be said about the analysis of the maximum sSFR in this analysis. However, in the three lowest redshift intervals, the luminosity-weighted escape fraction lies close to their fit. This is not the case for the other panels. An analysis of the maximum sSFR with more data and a higher mass range can be seen in Section 5.3.

The evolution of the escape fraction in time was mentioned in Figure 11. However, a clear conclusion cannot be made from the six panels in the plot; other than that it appears to increase with decreasing redshift. In Figure 15, the escape fraction f_{esc} is plotted versus the redshift z. Each escape fraction is again calculated for the 10 largest haloes in each snapshot. The red dots are data from haloes, which only contain less than 1000 gas cells, and the blue dots are data points from haloes, which contain more than 1000 gas cells. The grey line displays the median of the escape fraction for 24 redshift bins.

For redshifts higher than 12, a cloud of haloes with very high escape fractions can be seen in the top left corner. The majority of the data points in this cloud are likely affected by an insufficient resolution of the gas in these haloes. However, some of these haloes appear to have sufficiently high resolution and still have high escape fractions. These might still be insufficiently resolved around the stars, as visible in Figure A.1. As explained earlier, the feedback of only a few stars and photoevaporation from ionisation fronts of other galaxies might remove (almost) all of the gas from the halo, as the gravitational potential wells of these early haloes are rather shallow. These are the same galaxies seen in Figure 12 in the bottom two panels, increasing the escape fraction for very small masses. For haloes with redshifts smaller than 12 in Figure 15, which are not part of the cloud in the top left corner, one can see that the escape fraction increases with decreasing redshift. One could consider that this might be driven by the higher-mass galaxies analysed with decreasing redshift. However, at redshifts smaller than 8, this trend flattens. This flattening does not indicate the end of reionisation. As only the largest 10 haloes from each snapshot have been analysed, the area surrounding these galaxies might already be completely ionised at this point. However, the gas surrounding smaller haloes might still be rather neutral. A higher mass range is needed to make a statement about this.

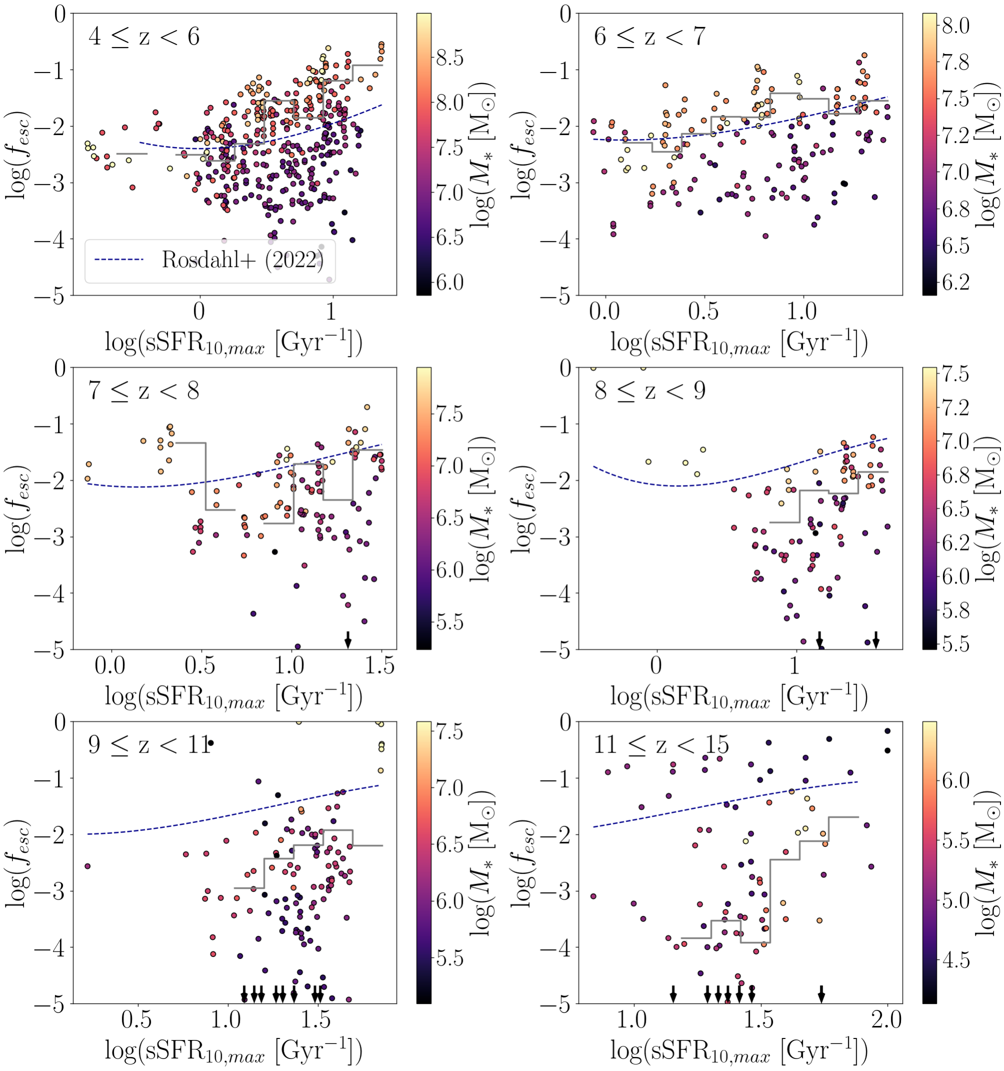

Figure 14: Escape fraction versus maximum specific star formation rate, based on the 10 Myr interval with the highest specific star formation rate of the last 50 Myr for six different redshift ranges. The stellar mass of a galaxy is indicated by the colour of the points. The arrows indicate galaxies with escape fractions below 10^{-5}. The grey lines show the luminosity-weighted mean escape fraction for 10 specific star formation rate bins, while only bins with five or more data points are shown. The dashed dark blue line is a fit to the luminosity-weighted mean escape fraction of the data of Rosdahl et al. (2022), which can be seen in their figure 15. Each data point is based on one of the 10 largest halos of one of the snapshots in the redshift range shown in the upper left corner of the panels. The haloes were taken from the high-resolution region of the resimulation of the medium group.

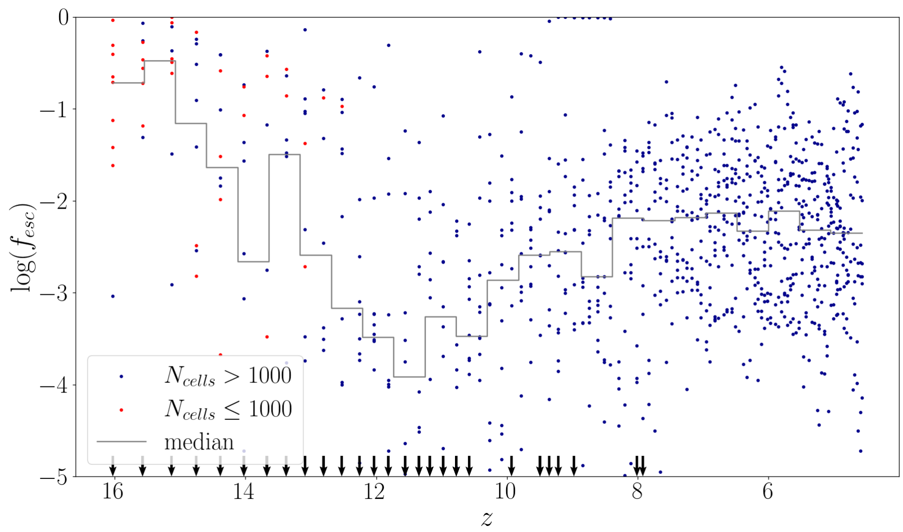

Figure 15: Escape fraction versus the redshift. Each data point is measured in one of the 10 largest haloes in each snapshot. The blue dots show haloes which contain more than 1000 gas cells, and the red dots show haloes that contain less than 1000 gas cells. The arrows indicate galaxies with escape fractions below 10^{-5}. The grey line shows the median escape fraction for 24 redshift bins. The haloes were taken from the resimulation of the medium group.

5.3 Ionising radiation escape over five orders of magnitude in halo mass

In this section, I will combine the results from three zoom-in simulations of groups from the THESAN simulation. Information about the groups shown here can be found in Table 1. In addition to the medium group already discussed in Section 5.2, one of the largest groups from the zoom-in simulations, THESAN group 39, was used, as well as one on the smaller side, group 500531. The small group has a zoom factor of 8 (512 times better mass resolution than THESAN) to ensure a high enough resolution. Again, the 10 largest FoF groups per snapshot were selected from each zoom-in simulation, due to the computational cost of the pre-processing of COLT. Only haloes completely in the high-resolution region of the snapshot are considered. This time, the plots are split up into seven redshift ranges, as the zoom-in simulations of the small and large groups were run until redshift 3. In Figures 16, 19 and 21, the galaxies found in the high-resolution region of the medium group are shown in blue, the large group in red and the small group in green.

As seen in the last section (Section 5.2), the SFR appears to be a good measure of the feedback injected influencing the escape fraction. However, the galaxies taken from the medium group only had a limited range of masses. To investigate what effect the SFR has on differently sized galaxies and how the SFRs of the galaxies in the three groups compare, one can see plots of the escape fraction versus the SFR averaged over 10 Myr in Figure 16. The arrows indicate galaxies with escape fractions below 10^{-5}. In the interval between redshift 3 and 4, one can see that while the galaxies in the high-resolution region of the large group indicate a positive correlation between the escape fraction and the SFR, the galaxies in the high-resolution region of the small group show a negative correlation. However, at SFRs around 10^6 $M_{\odot}/10$ Myr, the data from the small group is in reasonable agreement with the data from the large group.

When looking at the combined distribution of the data from the two groups, one can see a minimum escape fraction at about $10^{5.5}$ $M_{\odot}/10$ Myr. The same minimum can be seen in the interval between redshift 4 and 6. The maximum escape fraction at low SFRs reached maximum values of about 0.1 in this interval, while it reaches almost 1 in the interval between redshift 3 and 4. For the intervals at higher redshifts, a minimum cannot be found, while a flattening of the escape fraction for low SFRs can be seen in the interval from redshift 4 to 6. The combined data for the other redshift intervals displays an overall positive correlation between the escape fraction and SFR. The few galaxies in the small group form the lower end of this distribution. Galaxies in both the medium and large groups show a positive correlation between the escape fraction and the SFR in all panels. Their data points follow a very similar relation, with the data of the large group lying at higher SFRs than the data of the medium group. The galaxies in the small group forming the lower SFR end are not primarily due to the medium and large groups not containing small haloes; it is rather due to the bias towards large haloes introduced through only taking the 10 largest FoF groups per snapshot.

The data from the galaxies contained in the large group agrees with the findings from Figure 11 from Section 5.2. The escape fraction still increases with rising SFR in Figure 16. The increase of the data from the small group towards a higher escape fraction for lower SFRs for the redshift interval between 3 and 4 can be explained through those galaxies forming very few stars and also having a shallow potential well and/or little gas. This makes it easy for the feedback to create channels for the radiation to escape through. This gas ejection might also lead to a very low resolution in these small regions, even for a zoom-factor 8 simulation. Once the gas from haloes with shallow potential wells is removed, possibly by feedback or photoevaporation, they might not be able to accrete gas again due to having halo masses below the filtering mass. The gas surrounding the halo might have been heated up too much during the reionisation, such that it cannot accrete onto such small haloes anymore. These high escape fraction - low SFR galaxies do not appear prominently in the higher redshift intervals (except for a few points in the intervals from redshifts 9 to 11 and 11 to 15). A possible cause of this might be that there is too little data in these ranges to show such high escape fraction galaxies. This could be addressed by using more than the 10 largest haloes.

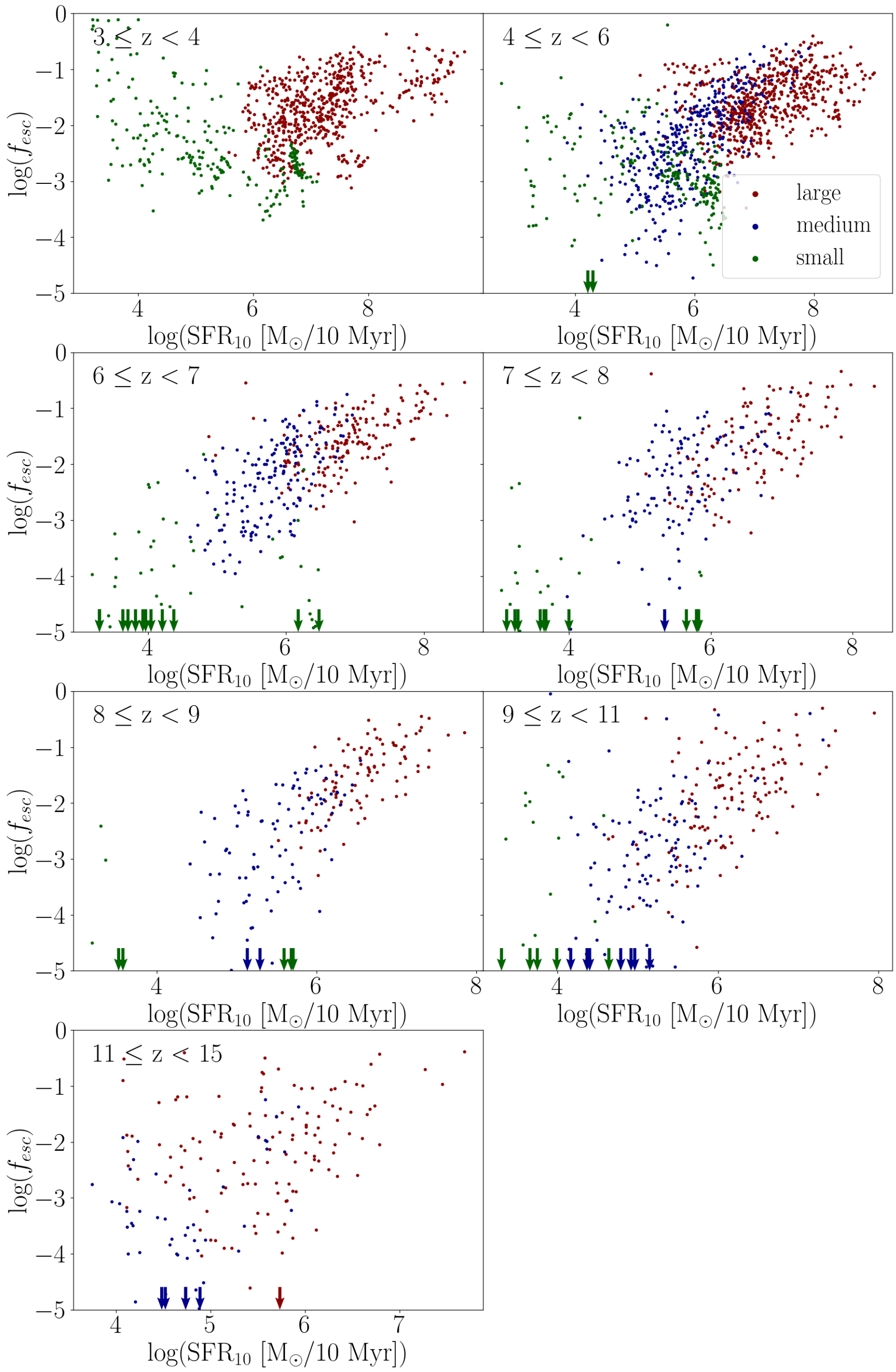

Figure 16: Escape fraction versus the star formation rate of the last 10 Myr for six different redshift ranges. Each data point is based on one of the 10 largest halos of one of the snapshots in the redshift range shown in the upper left corner of the panels. The arrows indicate galaxies with escape fractions below 10^{-5}. The haloes were taken from the resimulations of three THESAN groups, which are colour-coded. Red corresponds to the large group, which has a mass of 4.25×10^{12} M$_\odot$ at redshift 3, blue corresponds to the medium group, which has a mass of 4.74×10^{10} M$_\odot$ at redshift 4.6 and green corresponds to the small group, which has a mass of 1.94×10^{9} M$_\odot$ at redshift 3.

A possible explanation for galaxies having low escape fractions and low SFR is the following: these haloes have mostly old stars and not a lot of stars in general, such that not enough feedback is produced to eject the gas that is accreted. This would only be a very short-term effect, as the accreted gas would lead to new star formation and, hence, higher feedback, leading to higher escape fractions again. This cannot be observed in these higher redshift ranges, which might again be due to an insufficient amount of data. As the small group is still quite small at redshift 3, it does not have many star-forming haloes at higher redshifts. This could be better investigated by analysing more small haloes from the medium and large groups, not just the largest 10. Due to the amount of time and computational power needed for a broader analysis, this exceeded the scope of this thesis project.

In the last section, an analysis using the luminosity-weighted escape fraction was only partly possible due to the limited amount of data. The maximum sSFR seems like an interesting approach to not only account for the different strengths of feedback needed to eject gas from galaxies of different sizes but also take into account past periods of strong feedback in galaxies. Nevertheless, no clear correlation could be found in Figure 14. The larger mass range and abundance of objects when combining the data of the three groups might lead to different results.

A plot of the escape fraction versus the maximum sSFR as explained in Section 5.2 is shown in Figure 17 and Figure 18. The arrows indicate galaxies with escape fractions below 10^{-5}. The colour of the points shows the stellar mass. The data points are taken from all three THESAN groups. The dark blue dashed line is a fit through the data of Rosdahl et al. (2022), calculated using a luminosity-weighted mean in each bin, shown in their figure 15. The dark red line shows the luminosity-weighted mean for 24 maximum sSFR bins. Sometimes, fewer bins are shown, as only bins containing more than four objects are considered. Generally, the luminosity-weighted mean seems to agree quite well with the results of Rosdahl et al. (2022). In the intervals from redshift 4 to 9, the mean escape fraction calculated from our data lies above the fit from Rosdahl et al. (2022). For higher redshifts, my results lie slightly below their fit. In the interval from redshifts 4 to 6, the mean escape fraction even appears to have a minimum around the same point as the fit by Rosdahl et al. (2022). Another minimum can be seen in the interval from redshifts 3 to 4; however, the analysis of Rosdahl et al. (2022) only extends down to redshift 4.7, so this cannot be directly compared. Our data for the other redshift ranges becomes very scarce before the minimum found in their fit is reached, such that I cannot comment on the possible trajectory in comparison to the fit.

As the selection function here is different to that of Rosdahl et al. (2022), the luminosity-weighted means shown here are expected to somewhat differ. To get comparable results, also in terms of smoothness of relation, a more extensive analysis would be needed in which all star-forming galaxies from multiple THESAN groups are analysed. The data Rosdahl et al. (2022) used for their analysis of the escape fraction and the maximum sSFR in their figure 15 is also very scattered, and the shape looks similar to the one found here. While their data is very scattered, they have a large enough sample such that their luminosity-weighted escape fraction bins display a smooth relation and can hence be fitted well.

The effects of insufficient resolution were already visible in Figure 12, especially in the high redshift intervals. With the galaxies found in the high-resolution region of the small group, more data from small galaxies is available. While the small group has a better gas mass resolution than the other groups, the very small galaxies found in its high-resolution region still might have insufficiently resolved gas masses. A plot of the escape fraction versus the gas mass could show insufficiently resolved galaxies and a possible cutoff at which the gas mass is too high for feedback to efficiently form channels for radiation escape.

In Figure 19, one can see a plot of the escape fraction versus the gas mass. The arrows indicate galaxies with escape fractions below 10^{-5}. For this plot, two redshift intervals were chosen, which are representative of the other redshift intervals. It can be nicely seen that the galaxies found in the different THESAN groups sample different gas mass ranges. Considering the mass resolution of the gas in these zoom-in simulations, one can conclude that haloes with a gas mass lower than 10^6 $M_\odot$ have an insufficient resolution in the simulation of the small group, which has a zoom factor of 8. For the other two THESAN groups, a gas mass below 10^7 $M_\odot$ already becomes problematic. Even galaxies with a gas mass above these thresholds might be poorly resolved if, e.g. the majority of the gas cells are situated in a gas clump that is currently accreted, as can be seen in Figure A.2. The stripes that the scatter forms in Figure 19 show one halo over multiple snapshots.

For the interval between redshifts 4 and 6, the galaxies in the high-resolution region of the zoom simulations of the medium and large groups show an increase in the escape fraction towards higher gas masses. The data from the large group appears to flatten slightly above a gas mass of 10^{10} $M_\odot$, which might indicate that the feedback for galaxies with such high gas masses, and probably also high halo masses, cannot form as many channels for the radiation to escape through anymore. Additionally, our simulations do not include AGN feedback, which might become relevant in these galaxies as well. The galaxies found in the high-resolution region of the small group show a maximum escape fraction around 10^8 $M_\odot$ and very high escape fractions below masses of 10^7 $M_\odot$, as these are very gas-poor and possibly poorly resolved haloes. These trends of a decreasing escape fraction with increasing gas mass upto gas masses of 10^8 $M_\odot$ with a minimum around that point and then increasing escape fractions can be seen in the other redshift interval (and the ones not shown here) as well. In the interval from redshifts 8 to 9, one can also see some very high escape fraction galaxies of the medium group at $\sim 10^8$ and $\sim 10^{10}$. Many of the very high escape fraction galaxies cannot be seen in Figure 16. While these galaxies have very high escape fractions due to low gas content, they have had no star forma-

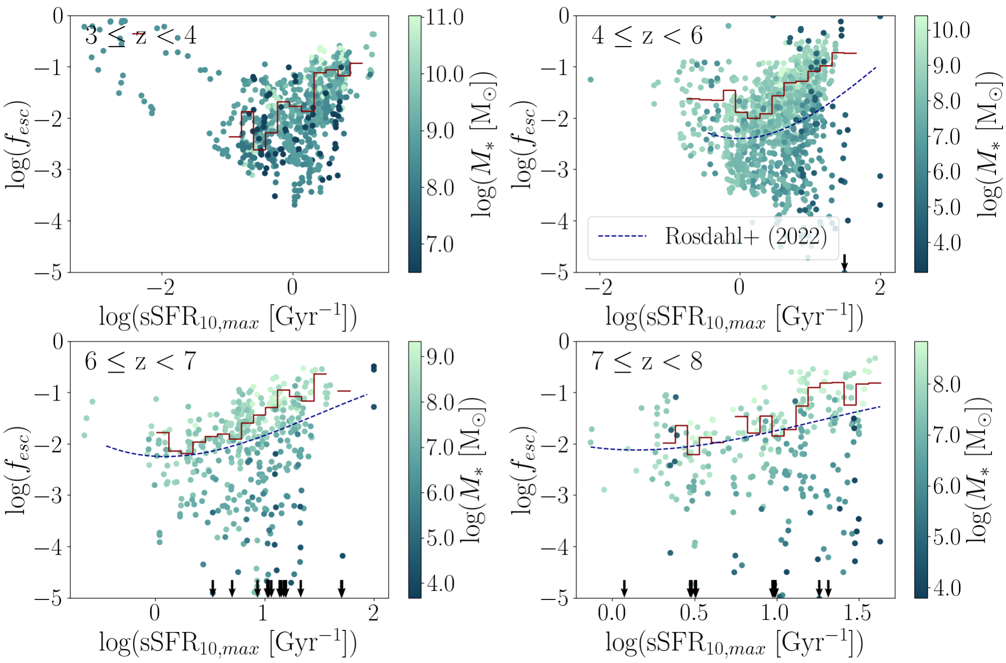

Figure 17: Escape fraction versus maximum specific star formation rate, based on the 10 Myr interval with the highest specific star formation rate of the last 50 Myr for six different redshift ranges (continued in Figure 18). The stellar mass of a galaxy is indicated by the colour of the points. The arrows indicate galaxies with escape fractions below 10^{-5}. The dark red lines show the luminosity-weighted mean escape fraction for 25 specific star formation rate bins, while only bins with more than four data points are shown. The dark blue line is a fit to the luminosity-weighted mean escape fraction of the data of Rosdahl et al. (2022), which can be seen in their figure 11. Each data point is based on one of the 10 largest halos of one of the snapshots in the redshift range shown in the upper left corner of the panels. The galaxies are taken from the high-resolution regions of the resimulations of three THESAN groups.

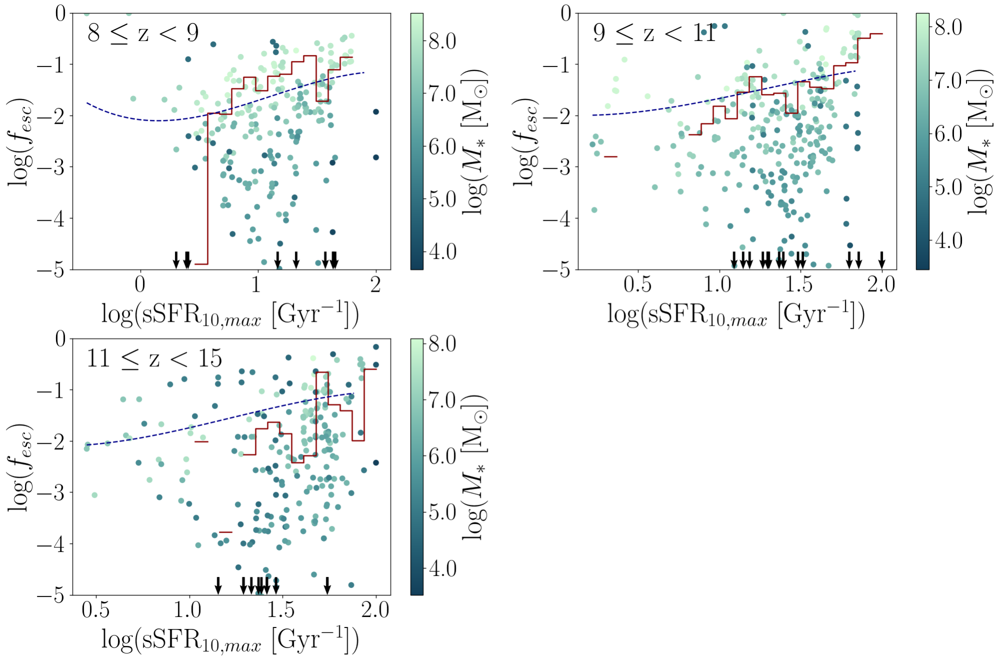

Figure 18: Continuation of Figure 17

tion in the last 10 Myr, and hence, the SFR over that interval is 0 and not shown in the Figure 16. Due to their very old stars, these galaxies also have rather low escaping luminosities and are irrelevant for reionisation.

The escape fraction seems to increase for increasing gas masses, and no clear cutoff point could be found in Figure 19. This indicates that the injected feedback seems to increase with gas mass. One could suspect that the stellar mass increases more strongly than the gas mass for increasing halo masses. In Figure 20, one can see plots of the stellar mass divided by the gas mass versus the virial mass. For this plot, two redshift intervals were chosen, which are representative of the other redshift intervals. The colour of the points shows the escape fraction of the corresponding halo. In both redshift intervals, one can see one branch in the lower half of the plots for which the stellar mass over gas mass fraction increases for higher halo masses. This shows that in this bottom branch, more stars per gas mass are formed in heavier haloes. This relationship between the gas mass and stellar mass is visualised in Figure B.1, which shows that the stellar mass increases more steeply than the gas mass.

The escape fraction increases for higher halo masses in Figure 20. The increase in stellar mass fraction for increasing halo masses, as can be found in the stellar mass halo mass relation for halo masses roughly below the Milky Way mass (Behroozi et al., 2019), also leads to more injected feedback. This increased feedback and the higher stellar mass over gas mass fraction leads to an increase in escape fraction, as the feedback appears strong enough to eject the gas even against a higher gravitational potential.

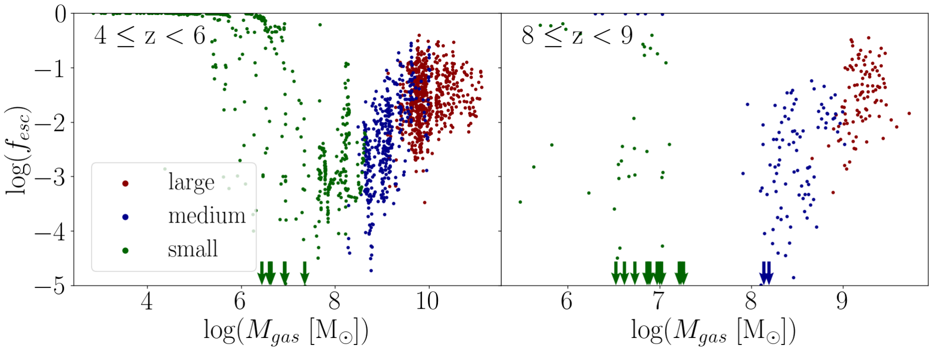

Figure 19: Escape fraction versus the gas mass for two different redshift ranges. Each data point is based on one of the 10 largest halos of one of the snapshots in the redshift range shown in the upper left corner of the panels. The arrows indicate galaxies with escape fractions below 10^{-5}. The haloes were taken from the resimulations of three THESAN groups, which are colour-coded. Red corresponds to the large group, blue corresponds to the medium group, and green corresponds to the small group.

As seen in Figure 11 and Figure 16, the escape fraction strictly increases for galaxies with increasing SFR instead of decreasing again for very high SFRs. The decrease could be explained by high halo and gas masses lowering the feedback efficiency. We can conclude now from Figure 20 that this is due to the stellar mass increasing stronger than the gas mass for higher halo masses and the feedback being strong enough to overcome the gravitational potential in large haloes. In Figure 12, one can see an increase in the escape fraction with higher stellar masses, deviating from the trajectory depicted by Rosdahl et al. (2022), which indicates a decrease in the escape fraction for higher stellar masses in their figure 9. This can also be traced back to the relation shown in Figure 20. It is not clear why this effect is not prominently present in SPHINX.

In Figure 20, in the redshift interval from 4 to 6, one can see high escape fraction haloes at low halo masses. They have stellar mass to gas mass ratios, which lie above the bottom branch. These data points appear in stripes, which is a good indication of belonging to the same halo sampled over multiple snapshots. These galaxies have possibly lost their gas from stellar feedback, as their halo mass is so low that they have very shallow potential wells. Another possibility is the removal of gas by photoevaporation by the ionisation fronts of other galaxies. Due to this, little gas mass in comparison to their stellar mass is left over, leading to these high escape fractions. Potentially, resolution problems may contribute to this as well. These small haloes might likely lie below the filtering mass in this region, such that they cannot accrete the surrounding gas anymore, as it was heated up due to reionisation. These galaxies have lost a lot of gas, and not many young stars are forming in them, as they cannot accrete gas; hence, their escaping luminosity is most likely low. Two more of these high stellar mass over gas mass fraction - high escape fraction distributions can be seen in the right panel. These appear to be only two galaxies sampled over multiple snapshots. They have a lower gas mass than their counterparts in the bottom branch.

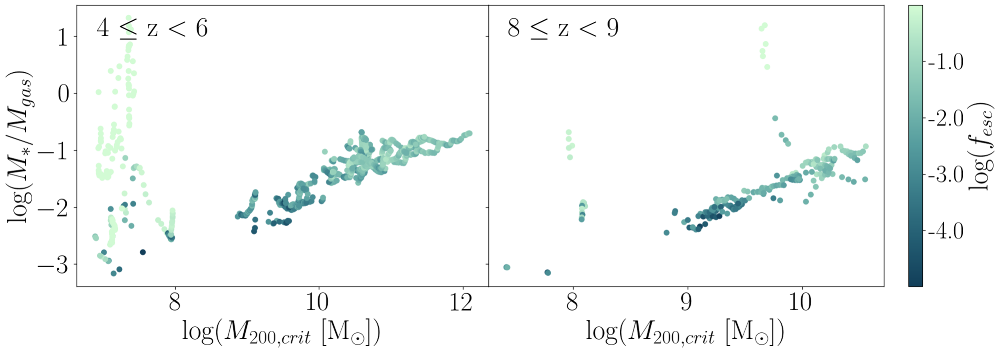

Figure 20: Stellar mass divided by the gas mass versus the virial mass for two redshift ranges. The escape fraction of a galaxy is indicated by the colour of the points. Each data point is based on one of the 10 largest halos of one of the snapshots in the redshift range shown in the upper left corner of the panels. The galaxies are taken from the high-resolution regions of the resimulations of three THESAN groups.

In the escape fraction versus redshift plot in Figure 15, it appears as if the reionisation of the medium group concludes after redshift 8. To see how the escape fraction behaves for the galaxies in the large and small groups, a plot of the escape fraction as a function of the redshift is shown in Figure 21. The colour of the dots corresponds to the galaxies found in the high-resolution regions of the different THESAN groups, similarly as above. The solid lines in the darker versions of the colours are the median of the escape fraction for 24 redshift bins. The medians of the escape fractions of the galaxies in both the large and medium groups appear constant after redshift 8. Before that, the escape fraction increased for both groups from redshift 12.5. At the highest redshifts, the escape fraction of the galaxies in the medium group decreases, and many of the high escape fraction galaxies had poor gas resolution. The shape of the median escape fraction of the galaxies in the large group before redshift 12.5 is most likely just due to scatter. The escape fractions of the galaxies in the small group are rather scattered before redshift 7 as a result of little data being available for these redshifts. After redshift 7, the median escape fraction of the galaxies in the small group is increasing fast due to very gas-poor haloes having escape fractions of (almost) 1. There are still many haloes with lower escape fractions, but the ones with larger escape fractions dominate.

The flattening of the median escape fraction for the galaxies in the medium and large group after redshift 8 could indicate the end of reionisation. As the largest 10 haloes from each snapshot are chosen, this only indicates that the gas surrounding these large galaxies is ionised at that point. The mass-weighted ionised hydrogen fraction of the high-resolution regions can be seen in Figure C.1, which also shows flattening around these redshifts. This indicates that only the self-shielded hydrogen remains neutral. The escape fractions of the galaxies belonging to the small group, which are not close to 1, appear to be increasing still at this point in Figure 21. However, due to the resolution problems of very small galaxies, no clear trend can be seen. As before, data with broader mass ranges would be needed here to make a conclusion. In Figure C.1, the high-resolution region of the small group appears to be mostly ionised at redshift 6, later than the larger groups. The evolution of the escape fraction as a function of redshift found in Figure 21 is different to the one Rosdahl et al. (2022) show in their figure 16, which is constantly decreasing towards lower redshifts, rather than increasing at intermediate redshifts. Additionally, the strong flattening we found cannot be seen in their figure 16, possibly due to a larger range of masses analysed. For a constant maximum sSFR, they find a nearly constant escape fraction over time after redshift ~ 8. Possibly the decrease they find is due to the evolution of the maximum sSFR over time and their selection function.

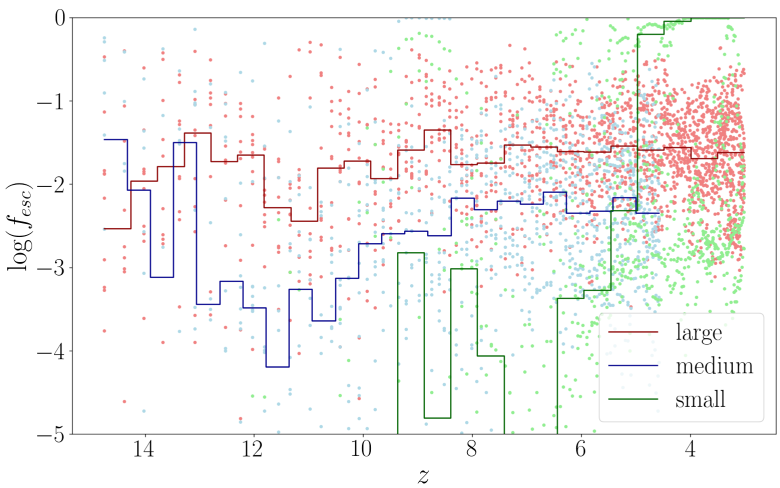

Figure 21: Escape fraction versus the redshift. Each data point is measured in one of the 10 largest haloes in each snapshot. The haloes were taken from the resimulations of three THESAN groups, which are colour-coded. Red corresponds to the large group, blue corresponds to the medium group, and green corresponds to the small group. The lines show the median escape fraction for 24 redshift bins for each group.

Many of the key differences found in comparison to the analysis of Rosdahl et al. (2022) cannot be reliably attributed to changes in the simulation model unless a more similar approach to theirs is followed in the analysis. While the galaxy formation model is a major difference, the amount of data analysed also deviates. I was only able to analyse parts of the THESAN zoom data available and was hence not able to conduct a more statistical analysis. Rosdahl et al. (2022) analysed a full box simulation, while I analysed groups in three zoom-in simulations. Lastly, the bias introduced by choosing the 10 largest haloes per snapshot likely also leads to significant differences.

6 Conclusion

In this thesis, I compared three different methods of determining the escape fraction from radiation hydrodynamical galaxy formation simulations and analysed the interplay of star formation and the associated feedback, as well as the escape fraction during the epoch of reionisation. During reionisation - as the name suggests - the intergalactic medium (IGM) was ionised through Lyman-Continuum radiation produced by the stars inside the first generations of galaxies. For this radiation to escape from the dense interstellar medium (ISM) into the IGM, (stellar) feedback is needed to create channels of low neutral hydrogen density in the ISM. Two of the most important kinds of feedback influencing the escape fraction are photoionisation and supernova feedback. The photoionisation feedback processes the gas to become less dense, such that supernova feedback can expel the gas from the ISM and, in turn, create the channels for the radiation to escape through. Another important form of feedback during reionisation is early stellar feedback, which suppresses the star formation before the first supernovae go off.

The simulations were based on the AREPO moving mesh code (Springel, 2009, 2010, 2011). The radiation was modelled using AREPO-RT (Kannan et al., 2019) and the M1 radiative transfer technique. The galaxies in the simulations were modelled using a modified version of the SMUGGLE galaxy formation model (Marinacci et al., 2019), which enables self-consistent feedback using the radiative transfer from AREPO-RT and aims to resolve the ISM. Additionally, early stellar feedback was implemented to reduce the star formation before the first massive stars die and go off as supernovae to agree with observations. However, this suppression does not appear as necessary at high redshifts as new JWST results suggest (e.g. Dekel et al., 2023; Haro et al., 2023; Finkelstein et al., 2023). The galaxies resimulated using the modified SMUGGLE model are taken from the THESAN simulation (Kannan et al., 2022; Smith et al., 2022; Garaldi et al., 2022), a full box simulation aimed to provide insight into the epoch of reionisation.

The first method of determining the escape fraction utilised the flux of the M1 radiative transfer as computed by AREPO-RT. The outward flux through a sphere at the virial radius of the galaxy was determined. From this and the luminosity of the stars inside the galaxy, the escape fraction could be determined. However, there are several caveats to this approach. The radiation is injected not directly at the star particle but in the 16 closest cells, leading to unphysical flux values in this region and an overestimated ionisation fraction. The M1 radiative transfer leads to interactions of the radiation from multiple distinct sources. One can get inward-pointing flux into the galaxy from external sources rather than outward-pointing flux, decreasing the galaxy's escape fraction unphysically. The outward propagation of radiation with the reduced speed of light assumption leads to a time delay in the escaping luminosity and the luminosity injected by the stars in the galaxy. This was approximately corrected under the assumption that the stars are located in the centre of the galaxy.

The second method of determining the escape fraction uses ray tracing from the galaxy's centre to the pixels of a HEALPix (Gorski et al., 2005) tesselation of a sphere at the virial radius of the galaxy. Although this approach does not have the same injection and interaction effects that the M1 method has, it assumes that the (young and bright) stars are located in the galaxy's centre. I have found that this assumption generally does not hold for our simulations. As the feedback forms underdense bubbles in the centre of the galaxies, where the first stars have formed, further stars are formed outside these bubbles in swept-up shells.

The last method of determining the escape fraction uses the COLT code (Smith et al., 2015), a Monte Carlo radiative transfer code, which ray traces photon packets from the individual star particles out to the virial radius of the galaxy. Although this method requires preprocessing of the snapshots, it is not significantly slower than ray tracing from the galaxy's centre. While the M1 flux approach is faster, it has too many caveats to be used in the analysis of escape fractions. Additionally, the results from COLT are reliable, as it does not rely on the M1 radiative transfer (other than using its ionisation states) or the assumption that all (young and bright) stars are at the centre of the galaxy.

The galaxies found in the high-resolution regions of zoom-in resimulations of three haloes of different sizes from the THESAN simulation were analysed to examine the interplay between the escape fraction, star formation rate, and the stellar, gas and halo mass. Next to the main halo aimed to resimulate, these high-resolution regions contain additional haloes analysed here. I found a positive correlation between the escape fraction and the star formation rate (SFR). As young stars inject the most feedback into the ISM, the SFR averaged over 10 Myr is a good measure of this feedback. The more stars have been formed recently, the higher the escape fraction is, as the feedback is able to form channels for the radiation to escape through. The specific SFR (sSFR), which is the SFR divided by the stellar mass, instead shows no positive correlation to the escape fraction. This suggests that the mass fraction of young stars in the galaxy does not determine the efficiency of feedback to create low-density channels alone; rather, one needs to consider other properties like the gas and halo mass as well.

The escape fractions of very small galaxies in our simulation are high. The haloes of these galaxies have rather low masses, making it easier for feedback to eject most of the halo's gas and increase the escape fraction. As the region around these small haloes becomes ionised by other galaxies, the gas from these small haloes might be boiled off by photoevaporation from the ionisation fronts of other galaxies. Due to the increase in temperature of the IGM throughout the epoch of reionisation, the halo mass of galaxies able to accrete gas (filtering mass) increases. This means that if a halo has lost large amounts of gas through feedback or photoevaporation, it might be unable to accrete gas any longer. While the loss of gas and the inability to accrete new gas increases the escape fraction of these small haloes over longer periods of time, the low stellar mass of these small galaxies, ageing stars, and inability to form new stars indicate a very low escaping luminosity. Hence, these galaxies will not contribute greatly to the reionisation of the IGM.

Galaxies with very low gas masses cannot be appropriately resolved. As the radiation is injected into a certain amount of cells around a star, the ionisation fraction of these cells will be higher. If too few gas cells are present in the ISM of a galaxy, the cells into which radiation is injected might cover large parts of it. Therefore, the ionisation fraction in the ISM might be unphysical and the escape fraction biased. The analysis shows an increase in escape fraction for lower gas masses and very high escape fractions for very poorly resolved galaxies.

Somewhat surprisingly, I find a positive correlation between the escape fraction and the gas mass for well-resolved haloes. In our simulation, the stellar mass over gas mass fraction increases with the halo mass. Through the stellar mass halo mass relation, it becomes clear that the stellar mass increases with halo mass for galaxies with halo masses lower than the Milky Way. However, the gas mass in our simulation does not increase as strongly with mass as the stellar mass does. The increase of stellar mass over gas mass indicates that more feedback per gas mass is injected in heavier haloes. This appears to mitigate the effects of deeper potential wells in heavier haloes, as the escape fraction positively correlates with the halo mass.

Lastly, an analysis of the escape fraction over multiple redshifts was conducted. While a constant escape fraction was found for redshifts lower than 8 for the two largest groups analysed, this does not indicate the end of the epoch of reionisation. Rather, the surroundings of these 10 largest haloes became ionised, while smaller haloes likely still reside in neutral regions.

A similar analysis as the one conducted in this thesis was also performed by Rosdahl et al. (2022), using one of the SPHINX simulations (Rosdahl et al., 2018), which was performed with RAMSES-RT (Rosdahl et al., 2013). A deeper introduction to this can be found in Section 1.3. While they find a maximum escape fraction at stellar masses around 10^7 $M_\odot$, with a decrease in escape fraction for both small and large stellar masses, this is not found here. I find a clear increase towards higher stellar masses, largely explained by the stellar mass to gas mass fraction as a function of halo mass. Additionally, I find an increase towards very small stellar masses, which might be (partly) due to insufficient resolution (possibly these galaxies have lost their gas by feedback or photoevaporation). However, Rosdahl et al. (2022) find a strong decrease instead. They explain this by insufficient star formation in these haloes to inject enough feedback for higher escape fractions. However, for these very small haloes, Rosdahl et al. (2022) also most likely don't have a sufficient mass resolution.

A comparison of the maximum sSFR of 10 Myr intervals in a period of 50 Myr yielded similar results to Rosdahl et al. (2022). The escape fraction appears to be increasing for increasing maximum sSFR rates after a minimum escape fraction at 1 Gyr^{-1}. Below that, they find a decrease in escape fraction for increasing maximum sSFRs. However, only very few data points from our sample lie in these ranges, such that no comment can be made on the similarity for lower maximum sSFRs. Additionally, the values of the escape fraction of our data coincide well with theirs. Furthermore, while I did not find a correlation between the sSFR and the escape fraction, Rosdahl et al. (2022) did. This might indicate that the channels through which the ionising radiation escapes form at different time scales in SPHINX and SMUGGLE-RT.

While not doing an extensive analysis of all star-forming galaxies in the high-resolution regions of many different resimulations of THESAN groups, I could still make some interesting conclusions. My analysis demonstrates the connection between the feedback injected by young stars and the ionising radiation escape in high-redshift galaxies in our simulations. I found an increase in the stellar mass - gas mass fraction and the escape fraction with halo size, suggesting that the feedback efficiency increases with halo mass for these early galaxies.

Additionally, strongly increased escape fractions due to the resolution of our simulations, but possibly also efficient feedback, photoevaporation, and the filtering mass could be found in low-mass objects. By only choosing the largest 10 haloes per snapshot, we have a different selection function in comparison to Rosdahl et al. (2022), which might bias the comparison to their results. However, comparing the escape fraction versus the maximum sSFR of our data and their data showed a similar correlation.

7 Outlook

The selection function in this thesis project was limited to the 10 largest haloes inside the high-resolution regions of the resimulations of three haloes of the THESAN simulation. Utilising a larger number of halos in possibly more simulations would be one way of enabling more detailed statistical analyses of the interplay between star formation rate and escape fraction, similar to Rosdahl et al. (2022). For example, analysing resimulations of more of the groups from THESAN extending the work done in this thesis would enable deeper insight into the dynamics inside differently-sized halos.

COLT has additional functionality computing an equilibrium ionisation state of hydrogen and helium. In this approach, the stars inside the halo are treated as if they have been shining forever. This assumption is appropriate inside the dense ISM, as the timescale at which the Lyman-Continuum radiation forms Strömgren spheres in the ISM is smaller than the timescale at which the luminosity of the stars changes significantly. As the IGM is much less dense, the timescale at which the ionisation is balanced out by recombination is much larger. Hence, the assumption that the stars have been shining forever is not appropriate there. In Figure 22, the four panels show slices of the neutral hydrogen fraction. The top two panels show a slice through a halo. The white circles show the virial radius. The two bottom panels show slices through the region the preprocessing for COLT extracts from the snapshot. This displays a larger part of the high-resolution region of the simulation. The right plots show the ionisation as derived by COLT in the equilibrium approach. As you can see in the top two panels, the radiation in the COLT approach was able to carve more channels for the radiation to escape from. In the bottom two panels, you can see that the ionisation fraction is mainly significantly higher in the COLT ionised panel. As expected, the M1 on-the-fly ionisation forms the ionised bubbles, while the rest of the IGM remains unionised. The COLT equilibrium ionised region, however, displays an overall higher ionisation while the bubbles are still visible. The exact reasoning behind this is not quite clear; however, exploring this is beyond the scope of this thesis. This indicates that while the COLT equilibrium ionisation appears valid for the ISM, the M1 on-the-fly ionisation appears more appropriate for the IGM. Combining these two approaches in a suitable way might yield better ionisation states of the universe during reionisation.

To compare the escape fractions of the equilibrium ionisation and on-the-fly ionisation approach, plots of the escape fraction versus the SFR for three different redshift intervals are shown in Figure 23. The colour of the data points shows the stellar mass. The left panels show the on-the-fly ionisation, which was already displayed in Figure 11. The right panels of Figure 23 display the data from the equilibrium ionisation. The escape fractions of the equilibrium ionised galaxies are generally higher. The trend of the escape fraction versus the SFR appears generally flatter in the equilibrium ionised data. While the escape fraction of the on-the-fly ionisation data shows a mere flattening towards lower

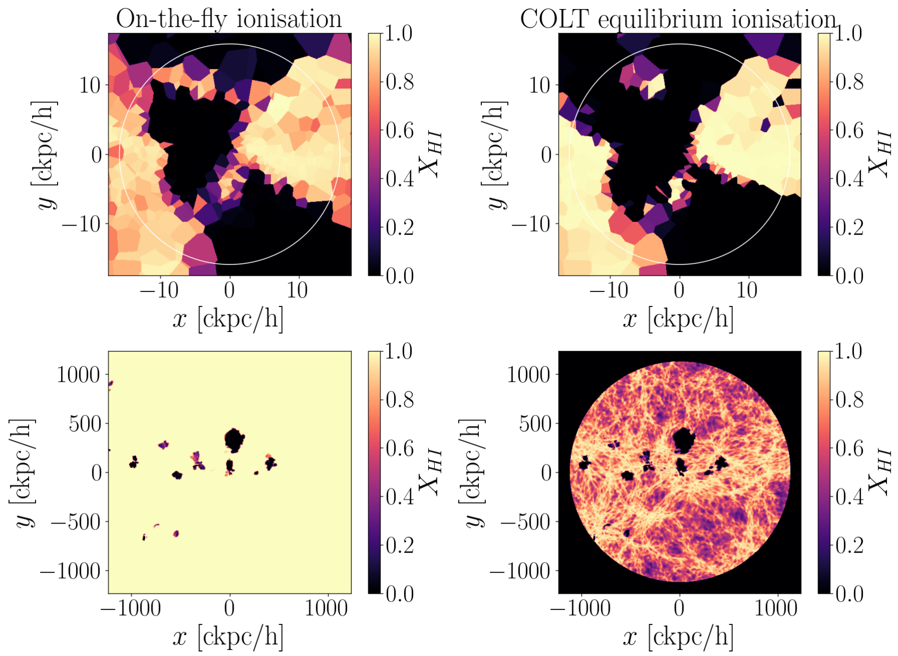

Figure 22: Four slices of the neutral hydrogen density. The upper two slices are taken of a halo, the white circle shows the virial radius. The bottom two panels show the region extracted by the preprocessing for COLT. They show a larger region of the high-resolution region. The left panels show the neutral hydrogen density as derived by the non-equilibrium approach in SMUGGLE-RT. The right panels show the neutral hydrogen density as ionised by the equilibrium approach of COLT.

SFRs, the equilibrium ionised galaxies have a slightly increasing escape fraction towards lower SFR values, especially in the intervals from redshift 4 to redshift 7. Why this happens would need to be investigated further. My suspicion is that the lower gas mass expected in galaxies with a lower SFR is easier to ionise, especially in the equilibrium approach, such that more channels are formed for the radiation to escape.

Another interesting analysis would be to see how active galactic nuclei (AGN) influence the radiation escape. They could either inject feedback and increase the escape fraction or inject luminosity and hence increase the escaping luminosity. The analysis of Trebitsch et al. (2018) concluded that AGN had negligible effects on both the feedback and escaping luminosity of dwarf galaxies, but an analysis of this using our simulation code might yield new insight.

A complete understanding of the ISM and the mechanisms influencing the escape fraction cannot be gained using SMUGGLE, as the ISM can still not be fully resolved at the moment. However, the ISM might be largely resolved with growing computational power and higher resolutions. Some of the first progress on this was made by Gutcke et al. (2022) with the LYRA model, which is imple-

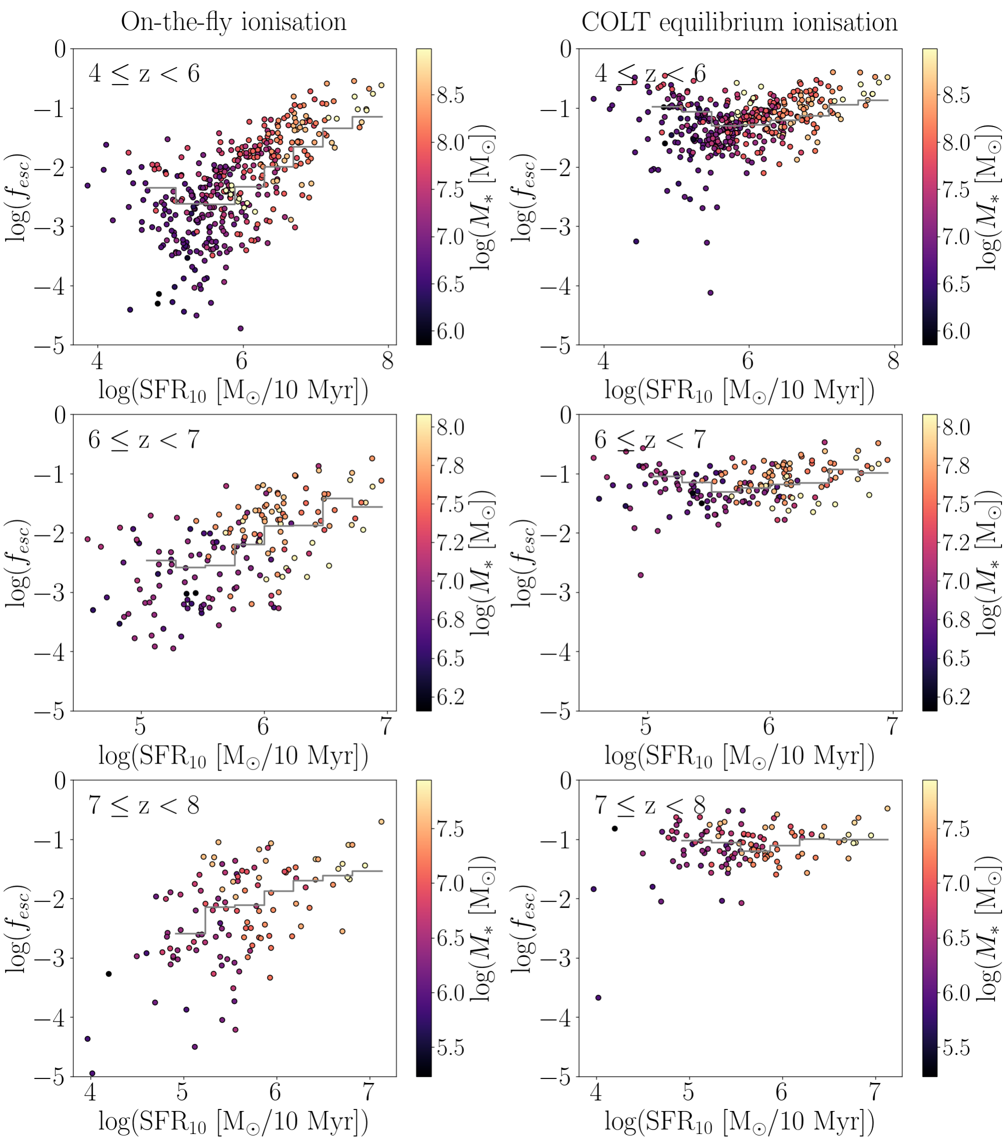

Figure 23: Escape fraction versus the star formation rate of the last 10 Myr for three different redshift ranges. The stellar mass of a galaxy is indicated by the colour of the points. The grey lines show the luminosity-weighted mean escape fraction for 10 star formation rate bins, while only bins with more than 10 data points are shown. Each data point is based on one of the 10 largest halos of one of the snapshots in the redshift range shown on the top of the panels. The haloes were taken from the high-resolution region of the resimulation of the medium group, which has a virial mass of 4.74 $\times 10^{10}$ M$_\odot$ at redshift 4.57. The left panels display the data with the ionisation states taken from the M1 radiative transfer. The right panels display the data with ionisation states derived from the COLT code.

mented in AREPO. This code aims to resolve individual massive stars and the feedback they provide, e.g. by resolving individual supernova explosions. With a resolution of 4 $M_\odot$, the simulation can resolve the processes in the ISM and the explosions of supernovae. At this point, LYRA was only used to simulate dwarf galaxies of sizes of up to 4×10^9 $M_\odot$. Once enough computational power is available to not only look at single galaxies with this high resolution but also do similar statistic analyses to the ones being conducted in this thesis, a more detailed view of the epoch of reionisation, the escape fractions and the interplay between these and the feedback inside the galaxies would be possible.

References

Abel, T., Bryan, G. L. and Norman, M. L. (2002). The Formation of the First Star in the Universe, *Science* **295**(5552): 93–98.
URL: *https://www.science.org/doi/10.1126/science.1063991*

Adams, N. J., Conselice, C. J., Ferreira, L., Austin, D., Trussler, J. A. A., Juodžbalis, I., Wilkins, S. M., Caruana, J., Dayal, P., Verma, A. and Vijayan, A. P. (2022). Discovery and properties of ultra-high redshift galaxies ($9 < z < 12$) in the *JWST* ERO SMACS 0723 Field, *Monthly Notices of the Royal Astronomical Society* **518**(3): 4755–4766.
URL: *https://academic.oup.com/mnras/article/518/3/4755/6835532*

Ahn, K., Shapiro, P. R., Iliev, I. T., Mellema, G. and Pen, U.-L. (2009). THE INHOMOGENEOUS BACKGROUND OF H_2 -DISSOCIATING RADIATION DURING COSMIC REIONIZATION, *The Astrophysical Journal* **695**(2): 1430–1445.
URL: *https://iopscience.iop.org/article/10.1088/0004-637X/695/2/1430*

Barkana, R. and Loeb, A. (1999). The Photoevaporation of Dwarf Galaxies during Reionization, *The Astrophysical Journal* **523**(1): 54–65.
URL: *https://iopscience.iop.org/article/10.1086/307724*

Bartelmann, M. and Pfrommer, C. (2023). Cosmology.
URL: *https://pages.aip.de/pfrommer/Lectures/cosmology.pdf*

Behroozi, P., Wechsler, R. H., Hearin, A. P. and Conroy, C. (2019). UniverseMachine: The correlation between galaxy growth and dark matter halo assembly from z = 0-10, *Monthly Notices of the Royal Astronomical Society* **488**(3): 3143–3194.
URL: *https://academic.oup.com/mnras/article/488/3/3143/5484868*

Benson, A. J. and Bower, R. (2010). Cold Mode Accretion in Galaxy Formation. Publisher: arXiv Version Number: 2.
URL: *https://arxiv.org/abs/1004.1162*

Birnboim, Y. and Dekel, A. (2003). Virial shocks in galactic haloes?, *Monthly Notices of the Royal Astronomical Society* **345**(1): 349–364.
URL: *https://doi.org/10.1046/j.1365-8711.2003.06955.x*

Bosman, S. E. I., Davies, F. B., Becker, G. D., Keating, L. C., Davies, R. L., Zhu, Y., Eilers, A.-C., D'Odorico, V., Bian, F., Bischetti, M., Cristiani, S. V., Fan, X., Farina, E. P., Haehnelt, M. G., Hennawi, J. F., Kulkarni, G., Mesinger, A., Meyer, R. A., Onoue, M., Pallottini, A., Qin, Y., Ryan-Weber, E., Schindler, J.-T., Walter, F., Wang, F. and Yang, J. (2022). Hydrogen reionization ends by $z = 5.3$: Lyman-α optical depth measured by the XQR-30 sample, *Monthly Notices of the*

Royal Astronomical Society **514**(1): 55–76.
URL: *https://academic.oup.com/mnras/article/514/1/55/6598046*

Brandt, T. D., Tojeiro, R., Aubourg, E., Heavens, A., Jimenez, R. and Strauss, M. A. (2010). THE AGES OF TYPE Ia SUPERNOVA PROGENITORS, *The Astronomical Journal* **140**(3): 804–816.
URL: *https://iopscience.iop.org/article/10.1088/0004-6256/140/3/804*

Brantseg, T. F. (2013). *Core-Collapse Supernova Remnants and Interactions with Their Surroundings*, Doctor of Philosophy, University of Iowa, Iowa City, IA, United States.
URL: *https://iro.uiowa.edu/esploro/outputs/doctoral/9983776866002771*

Bromm, V. (2013). Formation of the first stars, *Reports on Progress in Physics* **76**(11): 112901.
URL: *https://iopscience.iop.org/article/10.1088/0034-4885/76/11/112901*

Bromm, V. and Yoshida, N. (2011). The First Galaxies, *Annual Review of Astronomy and Astrophysics* **49**(1): 373–407. Publisher: Annual Reviews.
URL: *https://doi.org/10.1146/annurev-astro-081710-102608*

Burke, J. R. and Hollenbach, D. J. (1983). The gas-grain interaction in the interstellar medium - Thermal accommodation and trapping, *The Astrophysical Journal* **265**: 223–234. ADS Bibcode: 1983ApJ...265..223B.
URL: *https://ui.adsabs.harvard.edu/abs/1983ApJ...265..223B*

Cherchneff, I. and Dwek, E. (2010). THE CHEMISTRY OF POPULATION III SUPERNOVA EJECTA. II. THE NUCLEATION OF MOLECULAR CLUSTERS AS A DIAGNOSTIC FOR DUST IN THE EARLY UNIVERSE, *The Astrophysical Journal* **713**(1): 1–24.
URL: *https://iopscience.iop.org/article/10.1088/0004-637X/713/1/1*

Choi, J.-H. and Nagamine, K. (2009). Effects of metal enrichment and metal cooling in galaxy growth and cosmic star formation history, *Monthly Notices of the Royal Astronomical Society* **393**(4): 1595–1607.
URL: *https://doi.org/10.1111/j.1365-2966.2008.14297.x*

Cox, D. P. (1972). Cooling and Evolution of a Supernova Remnant, *The Astrophysical Journal* **178**: 159–168. ADS Bibcode: 1972ApJ...178..159C.
URL: *https://ui.adsabs.harvard.edu/abs/1972ApJ...178..159C*

Dekel, A. and Birnboim, Y. (2006). Galaxy bimodality due to cold flows and shock heating, *Monthly Notices of the Royal Astronomical Society* **368**(1): 2–20.
URL: *https://doi.org/10.1111/j.1365-2966.2006.10145.x*

Dekel, A., Sarkar, K. C., Birnboim, Y., Mandelker, N. and Li, Z. (2023). Efficient formation of massive galaxies at cosmic dawn by feedback-free starbursts,

Monthly Notices of the Royal Astronomical Society **523**(3): 3201–3218.
URL: *https://academic.oup.com/mnras/article/523/3/3201/7179993*

Donnan, C. T., McLeod, D. J., Dunlop, J. S., McLure, R. J., Carnall, A. C., Begley, R., Cullen, F., Hamadouche, M. L., Bowler, R. A. A., Magee, D., McCracken, H. J., Milvang-Jensen, B., Moneti, A. and Targett, T. (2022). The evolution of the galaxy UV luminosity function at redshifts $z \simeq 8 - 15$ from deep *JWST* and ground-based near-infrared imaging, *Monthly Notices of the Royal Astronomical Society* **518**(4): 6011–6040.
URL: *https://academic.oup.com/mnras/article/518/4/6011/6849970*

Donnan, C. T., McLeod, D. J., McLure, R. J., Dunlop, J. S., Carnall, A. C., Cullen, F. and Magee, D. (2023). The abundance of $z \gtrsim 10$ galaxy candidates in the HUDF using deep JWST NIRCam medium-band imaging, *Monthly Notices of the Royal Astronomical Society* **520**(3): 4554–4561.
URL: *https://academic.oup.com/mnras/article/520/3/4554/7034347*

Dwek, E. (1998). The Evolution of the Elemental Abundances in the Gas and Dust Phases of the Galaxy, *The Astrophysical Journal* **501**(2): 643–665.
URL: *https://iopscience.iop.org/article/10.1086/305829*

D'Aloisio, A., McQuinn, M., Maupin, O., Davies, F. B., Trac, H., Fuller, S. and Upton Sanderbeck, P. R. (2019). Heating of the Intergalactic Medium by Hydrogen Reionization, *The Astrophysical Journal* **874**(2): 154.
URL: *https://iopscience.iop.org/article/10.3847/1538-4357/ab0d83*

Efstathiou, G. (2000). A model of supernova feedback in galaxy formation, *Monthly Notices of the Royal Astronomical Society* **317**(3): 697–719.
URL: *https://academic.oup.com/mnras/article/317/3/697/967513*

Eldridge, J. J., Stanway, E. R., Xiao, L., McClelland, L. A. S., Taylor, G., Ng, M., Greis, S. M. L. and Bray, J. C. (2017). Binary Population and Spectral Synthesis Version 2.1: construction, observational verification and new results, *Publications of the Astronomical Society of Australia* **34**: e058. arXiv:1710.02154 [astro-ph].
URL: *http://arxiv.org/abs/1710.02154*

Ferland, G. J., Korista, K. T., Verner, D. A., Ferguson, J. W., Kingdon, J. B. and Verner, E. M. (1998). CLOUDY 90: Numerical Simulation of Plasmas and Their Spectra, *Publications of the Astronomical Society of the Pacific* **110**(749): 761–778.
URL: *http://iopscience.iop.org/article/10.1086/316190*

Finkelstein, S. L., Bagley, M. B., Ferguson, H. C., Wilkins, S. M., Kartaltepe, J. S., Papovich, C., Yung, L. Y. A., Arrabal Haro, P., Behroozi, P., Dickinson, M., Kocevski, D. D., Koekemoer, A. M., Larson, R. L., Le Bail, A., Morales, A. M., Pérez-González, P. G., Burgarella, D., Davé, R., Hirschmann, M., Somerville,

R. S., Wuyts, S., Bromm, V., Casey, C. M., Fontana, A., Fujimoto, S., Gardner, J. P., Giavalisco, M., Grazian, A., Grogin, N. A., Hathi, N. P., Hutchison, T. A., Jha, S. W., Jogee, S., Kewley, L. J., Kirkpatrick, A., Long, A. S., Lotz, J. M., Pentericci, L., Pierel, J. D. R., Pirzkal, N., Ravindranath, S., Ryan, R. E., Trump, J. R., Yang, G., Bhatawdekar, R., Bisigello, L., Buat, V., Calabrò, A., Castellano, M., Cleri, N. J., Cooper, M. C., Croton, D., Daddi, E., Dekel, A., Elbaz, D., Franco, M., Gawiser, E., Holwerda, B. W., Huertas-Company, M., Jaskot, A. E., Leung, G. C. K., Lucas, R. A., Mobasher, B., Pandya, V., Tacchella, S., Weiner, B. J. and Zavala, J. A. (2023). CEERS Key Paper. I. An Early Look into the First 500 Myr of Galaxy Formation with JWST, *The Astrophysical Journal Letters* **946**(1): L13.
URL: *https://iopscience.iop.org/article/10.3847/2041-8213/acade4*

Furlanetto, S. R., Peng Oh, S. and Briggs, F. H. (2006). Cosmology at low frequencies: The 21cm transition and the high-redshift Universe, *Physics Reports* **433**(4-6): 181–301.
URL: *https://linkinghub.elsevier.com/retrieve/pii/S0370157306002730*

Garaldi, E., Kannan, R., Smith, A., Springel, V., Pakmor, R., Vogelsberger, M. and Hernquist, L. (2022). The THESAN project: properties of the intergalactic medium and its connection to Reionization-era galaxies, *Monthly Notices of the Royal Astronomical Society* **512**(4): 4909–4933. arXiv:2110.01628 [astro-ph].
URL: *http://arxiv.org/abs/2110.01628*

Glover, S. (2005). The Formation Of The First Stars In The Universe, *Space Science Reviews* **117**(3-4): 445–508.
URL: *http://link.springer.com/10.1007/s11214-005-5821-y*

Glover, S. C. O. (2011). The Chemistry of the Early Universe, *Proceedings of the International Astronomical Union* **7**(S280): 313–324. Edition: 2011/12/21 Publisher: Cambridge University Press.
URL: *https://www.cambridge.org/core/product/2A667FAD439C933E990FCB786F7CDAD7*

Glover, S. C. O. and Brand, P. W. J. L. (2003). Radiative feedback from an early X-ray background, *Monthly Notices of the Royal Astronomical Society* **340**(1): 210–226.
URL: *https://doi.org/10.1046/j.1365-8711.2003.06311.x*

Gnedin, N. Y. (2000). Effect of Reionization on Structure Formation in the Universe, *The Astrophysical Journal* **542**(2): 535–541.
URL: *https://iopscience.iop.org/article/10.1086/317042*

Gnedin, N. Y. and Abel, T. (2001). Multi-dimensional cosmological radiative transfer with a Variable Eddington Tensor formalism, *New Astronomy* **6**(7): 437–455.
URL: *https://linkinghub.elsevier.com/retrieve/pii/S1384107601000689*

Gorski, K. M., Hivon, E., Banday, A. J., Wandelt, B. D., Hansen, F. K., Reinecke, M. and Bartelmann, M. (2005). HEALPix: A Framework for High-Resolution Discretization and Fast Analysis of Data Distributed on the Sphere, *The Astrophysical Journal* **622**(2): 759–771.
URL: *https://iopscience.iop.org/article/10.1086/427976*

Greif, T. H., White, S. D. M., Klessen, R. S. and Springel, V. (2011). THE DELAY OF POPULATION III STAR FORMATION BY SUPERSONIC STREAMING VELOCITIES, *The Astrophysical Journal* **736**(2): 147.
URL: *https://iopscience.iop.org/article/10.1088/0004-637X/736/2/147*

Gutcke, T. A., Pfrommer, C., Bryan, G. L., Pakmor, R., Springel, V. and Naab, T. (2022). LYRA. III. The Smallest Reionization Survivors, *The Astrophysical Journal* **941**(2): 120.
URL: *https://iopscience.iop.org/article/10.3847/1538-4357/aca1b4*

Haiman, Z., Abel, T. and Rees, M. J. (2000). The Radiative Feedback of the First Cosmological Objects, *The Astrophysical Journal* **534**(1): 11–24.
URL: *https://iopscience.iop.org/article/10.1086/308723*

Haro, P. A., Dickinson, M., Finkelstein, S. L., Fujimoto, S., Fernández, V., Kartaltepe, J. S., Jung, I., Cole, J. W., Burgarella, D., Chworowsky, K., Hutchison, T. A., Morales, A. M., Papovich, C., Simons, R. C., Amorín, R. O., Backhaus, B. E., Bagley, M. B., Bisigello, L., Calabrò, A., Castellano, M., Cleri, N. J., Davé, R., Dekel, A., Ferguson, H. C., Fontana, A., Gawiser, E., Giavalisco, M., Harish, S., Hathi, N. P., Hirschmann, M., Holwerda, B. W., Huertas-Company, M., Koekemoer, A. M., Larson, R. L., Lucas, R. A., Mobasher, B., Pérez-González, P. G., Pirzkal, N., Rose, C., Santini, P., Trump, J. R., de la Vega, A., Wang, X., Weiner, B. J., Wilkins, S. M., Yang, G., Yung, L. Y. A. and Zavala, J. A. (2023). Spectroscopic Confirmation of CEERS NIRCam-selected Galaxies at $\boldsymbol{nzn \simeq 8-10}$, *The Astrophysical Journal Letters* **951**(1): L22. arXiv:2304.05378 [astro-ph].
URL: *http://arxiv.org/abs/2304.05378*

Hollenbach, D. and McKee, C. F. (1979). Molecule formation and infrared emission in fast interstellar shocks. I. Physical processes., *The Astrophysical Journal Supplement Series* **41**: 555–592. Publisher: IOP ADS Bibcode: 1979ApJS...41..555H.
URL: *https://ui.adsabs.harvard.edu/abs/1979ApJS...41..555H*

Hopkins, P. F., Wetzel, A., Kereš, D., Faucher-Giguère, C.-A., Quataert, E., Boylan-Kolchin, M., Murray, N., Hayward, C. C., Garrison-Kimmel, S., Hummels, C., Feldmann, R., Torrey, P., Ma, X., Anglés-Alcázar, D., Su, K.-Y., Orr, M., Schmitz, D., Escala, I., Sanderson, R., Grudić, M. Y., Hafen, Z., Kim, J.-H., Fitts, A., Bullock, J. S., Wheeler, C., Chan, T. K., Elbert, O. D. and Narayanan, D. (2018). FIRE-2 simulations: physics versus numerics in galaxy formation,

Monthly Notices of the Royal Astronomical Society **480**(1): 800–863.
URL: *https://doi.org/10.1093/mnras/sty1690*

Iliev, I. T., Shapiro, P. R. and Raga, A. C. (2005). Minihalo photoevaporation during cosmic reionization: evaporation times and photon consumption rates, *Monthly Notices of the Royal Astronomical Society* **361**(2): 405–414.
URL: *https://academic.oup.com/mnras/article-lookup/doi/10.1111/j.1365-2966.2005.09155.x*

Indriolo, N. and McCall, B. J. (2012). INVESTIGATING THE COSMIC-RAY IONIZATION RATE IN THE GALACTIC DIFFUSE INTERSTELLAR MEDIUM THROUGH OBSERVATIONS OF H_3^+, *The Astrophysical Journal* **745**(1): 91.
URL: *https://iopscience.iop.org/article/10.1088/0004-637X/745/1/91*

Kannan, R., Garaldi, E., Smith, A., Pakmor, R., Springel, V., Vogelsberger, M. and Hernquist, L. (2022). Introducing the THESAN project: radiation-magnetohydrodynamic simulations of the epoch of reionization, *Monthly Notices of the Royal Astronomical Society* **511**(3): 4005–4030. arXiv:2110.00584 [astro-ph].
URL: *http://arxiv.org/abs/2110.00584*

Kannan, R., Marinacci, F., Vogelsberger, M., Sales, L. V., Torrey, P., Springel, V. and Hernquist, L. (2020). Simulating the interstellar medium of galaxies with radiative transfer, non-equilibrium thermochemistry, and dust, *Monthly Notices of the Royal Astronomical Society* **499**(4): 5732–5748.
URL: *https://doi.org/10.1093/mnras/staa3249*

Kannan, R., Vogelsberger, M., Marinacci, F., McKinnon, R., Pakmor, R. and Springel, V. (2019). Arepo-rt: radiation hydrodynamics on a moving mesh, *Monthly Notices of the Royal Astronomical Society* **485**(1): 117–149.
URL: *https://academic.oup.com/mnras/article/485/1/117/5303742*

Katz, N., Weinberg, D. H. and Hernquist, L. (1996). Cosmological Simulations with TreeSPH, *The Astrophysical Journal Supplement Series* **105**: 19.
URL: *http://adsabs.harvard.edu/doi/10.1086/192305*

Kereš, D., Katz, N., Weinberg, D. H. and Davé, R. (2005). How do galaxies get their gas?, *Monthly Notices of the Royal Astronomical Society* **363**(1): 2–28.
URL: *https://doi.org/10.1111/j.1365-2966.2005.09451.x*

Kimm, T., Haehnelt, M., Blaizot, J., Katz, H., Michel-Dansac, L., Garel, T., Rosdahl, J. and Teyssier, R. (2018). Impact of Lyman alpha pressure on metal-poor dwarf galaxies, *Monthly Notices of the Royal Astronomical Society* **475**(4): 4617–4635.
URL: *https://doi.org/10.1093/mnras/sty126*

Klessen, R. S. and Glover, S. C. (2023). The First Stars: Formation, Properties, and Impact, *Annual Review of Astronomy and Astrophysics* **61**(1): 65–130. Publisher: Annual Reviews.
URL: *https://doi.org/10.1146/annurev-astro-071221-053453*

Kulkarni, G., Keating, L. C., Haehnelt, M. G., Bosman, S. E. I., Puchwein, E., Chardin, J. and Aubert, D. (2019). Large Ly α opacity fluctuations and low CMB τ in models of late reionization with large islands of neutral hydrogen extending to $z > 5.5$, *Monthly Notices of the Royal Astronomical Society: Letters* **485**(1): L24–L28.
URL: *https://academic.oup.com/mnrasl/article/485/1/L24/5364567*

Labbé, I., Van Dokkum, P., Nelson, E., Bezanson, R., Suess, K. A., Leja, J., Brammer, G., Whitaker, K., Mathews, E., Stefanon, M. and Wang, B. (2023). A population of red candidate massive galaxies $\sim$ 600 Myr after the Big Bang, *Nature* **616**(7956): 266–269.
URL: *https://www.nature.com/articles/s41586-023-05786-2*

Latif, M. A. and Khochfar, S. (2019). UV regulated star formation in high-redshift galaxies, *Monthly Notices of the Royal Astronomical Society* **490**(2): 2706–2716.
URL: *https://doi.org/10.1093/mnras/stz2812*

Levermore, C. (1984). Relating Eddington factors to flux limiters, *Journal of Quantitative Spectroscopy and Radiative Transfer* **31**(2): 149–160.
URL: *https://linkinghub.elsevier.com/retrieve/pii/0022407384901122*

Li, Z., Dekel, A., Sarkar, K. C., Aung, H., Giavalisco, M., Mandelker, N. and Tacchella, S. (2023). Feedback-Free Starbursts at Cosmic Dawn: Observable Predictions for JWST. arXiv:2311.14662 [astro-ph].
URL: *http://arxiv.org/abs/2311.14662*

López Fernández, R., González Delgado, R. M., Pérez, E., García-Benito, R., Cid Fernandes, R., Schoenell, W., Sánchez, S. F., Gallazzi, A., Sánchez-Blázquez, P., Vale Asari, N. and Walcher, C. J. (2018). Cosmic evolution of the spatially resolved star formation rate and stellar mass of the CALIFA survey, *A&A* **615**.
URL: *https://doi.org/10.1051/0004-6361/201732358*

Machacek, M. E., Bryan, G. L. and Abel, T. (2001). Simulations of Pregalactic Structure Formation with Radiative Feedback, *The Astrophysical Journal* **548**(2): 509–521.
URL: *https://iopscience.iop.org/article/10.1086/319014*

Maoz, D., Mannucci, F. and Brandt, T. D. (2012). The delay-time distribution of Type Ia supernovae from Sloan II: SDSS2 supernova DTD, *Monthly Notices of the Royal Astronomical Society* **426**(4): 3282–3294.

URL: *https://academic.oup.com/mnras/article-lookup/doi/10.1111/j.1365-2966.2012.21871.x*

Marinacci, F., Sales, L. V., Vogelsberger, M., Torrey, P. and Springel, V. (2019). Simulating the interstellar medium and stellar feedback on a moving mesh: implementation and isolated galaxies, *Monthly Notices of the Royal Astronomical Society* **489**(3): 4233–4260.
URL: *https://academic.oup.com/mnras/article/489/3/4233/5565052*

McQuinn, M. and O'Leary, R. M. (2012). THE IMPACT OF THE SUPERSONIC BARYON-DARK MATTER VELOCITY DIFFERENCE ON THE $z \sim 20$ 21 cm BACKGROUND, *The Astrophysical Journal* **760**(1): 3.
URL: *https://iopscience.iop.org/article/10.1088/0004-637X/760/1/3*

Mebane, R. H., Mirocha, J. and Furlanetto, S. R. (2018). The Persistence of Population III Star Formation, *Monthly Notices of the Royal Astronomical Society* **479**(4): 4544–4559.
URL: *https://academic.oup.com/mnras/article/479/4/4544/5054055*

Michel-Dansac, L., Blaizot, J., Garel, T., Verhamme, A., Kimm, T. and Trebitsch, M. (2020). RASCAS: RAdiation SCattering in Astrophysical Simulations, *A&A* **635**.
URL: *https://doi.org/10.1051/0004-6361/201834961*

Mihalas, D. and Mihalas, B. W. (1984). *Foundations of radiation hydrodynamics*. Publication Title: New York ADS Bibcode: 1984oup..book.....M.
URL: *https://ui.adsabs.harvard.edu/abs/1984oup..book.....M*

Mirabel, I. F., Dijkstra, M., Laurent, P., Loeb, A. and Pritchard, J. R. (2011). Stellar black holes at the dawn of the universe, *A&A* **528**.
URL: *https://doi.org/10.1051/0004-6361/201016357*

Mitra, S. and Chatterjee, A. (2023). Non-parametric Reconstruction of Photon Escape Fraction from Reionization. arXiv:2303.02704 [astro-ph].
URL: *http://arxiv.org/abs/2303.02704*

Muñoz, J. B., Mirocha, J., Chisholm, J., Furlanetto, S. R. and Mason, C. (2024). Reionization after JWST: a photon budget crisis? arXiv:2404.07250 [astro-ph, physics:hep-ph].
URL: *http://arxiv.org/abs/2404.07250*

Naoz, S., Yoshida, N. and Gnedin, N. Y. (2012). SIMULATIONS OF EARLY BARYONIC STRUCTURE FORMATION WITH STREAM VELOCITY. I. HALO ABUNDANCE, *The Astrophysical Journal* **747**(2): 128.
URL: *https://iopscience.iop.org/article/10.1088/0004-637X/747/2/128*

Navarro, J. F. and Steinmetz, M. (1997). The Effects of a Photoionizing Ultraviolet Background on the Formation of Disk Galaxies, *The Astrophysical Journal* **478**(1): 13–28.
URL: *https://iopscience.iop.org/article/10.1086/303763*

Nozawa, T., Kozasa, T., Umeda, H., Maeda, K. and Nomoto, K. (2003). Dust in the Early Universe: Dust Formation in the Ejecta of Population III Supernovae, *The Astrophysical Journal* **598**(2): 785–803.
URL: *https://iopscience.iop.org/article/10.1086/379011*

Oh, S. P. (2001). Reionization by Hard Photons. I. X-Rays from the First Star Clusters, *The Astrophysical Journal* **553**(2): 499.
URL: *https://dx.doi.org/10.1086/320957*

Oh, S. P. and Haiman, Z. (2002). Second-Generation Objects in the Universe: Radiative Cooling and Collapse of Halos with Virial Temperatures above 10^4 K, *The Astrophysical Journal* **569**(2): 558–572.
URL: *https://iopscience.iop.org/article/10.1086/339393*

O'Leary, R. M. and McQuinn, M. (2012). THE FORMATION OF THE FIRST COSMIC STRUCTURES AND THE PHYSICS OF THE $z \sim 20$ UNIVERSE, *The Astrophysical Journal* **760**(1): 4.
URL: *https://iopscience.iop.org/article/10.1088/0004-637X/760/1/4*

Olivier, G. M., Lopez, L. A., Rosen, A. L., Nayak, O., Reiter, M., Krumholz, M. R. and Bolatto, A. D. (2021). Evolution of Stellar Feedback in H ii Regions, *The Astrophysical Journal* **908**(1): 68. Publisher: The American Astronomical Society.
URL: *https://dx.doi.org/10.3847/1538-4357/abd24a*

O'Shea, B. W. and Norman, M. L. (2008). Population III Star Formation in a λCDM Universe. II. Effects of a Photodissociating Background, *The Astrophysical Journal* **673**(1): 14–33.
URL: *https://iopscience.iop.org/article/10.1086/524006*

Pakmor, R. and Springel, V. (2013). Simulations of magnetic fields in isolated disc galaxies, *Monthly Notices of the Royal Astronomical Society* **432**(1): 176–193.
URL: *http://academic.oup.com/mnras/article/432/1/176/1116630/Simulations-of-magnetic-fields-in-isolated-disc*

Pakmor, R., Springel, V., Bauer, A., Mocz, P., Munoz, D. J., Ohlmann, S. T., Schaal, K. and Zhu, C. (2016). Improving the convergence properties of the moving-mesh code AREPO, *Monthly Notices of the Royal Astronomical Society* **455**(1): 1134–1143.
URL: *http://academic.oup.com/mnras/article/455/1/1134/986779/Improving-the-convergence-properties-of-the*

Pillepich, A., Springel, V., Nelson, D., Genel, S., Naiman, J., Pakmor, R., Hernquist, L., Torrey, P., Vogelsberger, M., Weinberger, R. and Marinacci, F. (2018). Simulating Galaxy Formation with the IllustrisTNG Model, *Monthly Notices of the Royal Astronomical Society* **473**(3): 4077–4106. arXiv:1703.02970 [astro-ph].
URL: *http://arxiv.org/abs/1703.02970*

Planck Collaboration, Aghanim, N., Akrami, Y., Ashdown, M., Aumont, J., Baccigalupi, C., Ballardini, M., Banday, A. J., Barreiro, R. B., Bartolo, N., Basak, S., Battye, R., Benabed, K., Bernard, J.-P., Bersanelli, M., Bielewicz, P., Bock, J. J., Bond, J. R., Borrill, J., Bouchet, F. R., Boulanger, F., Bucher, M., Burigana, C., Butler, R. C., Calabrese, E., Cardoso, J.-F., Carron, J., Challinor, A., Chiang, H. C., Chluba, J., Colombo, L. P. L., Combet, C., Contreras, D., Crill, B. P., Cuttaia, F., de Bernardis, P., de Zotti, G., Delabrouille, J., Delouis, J.-M., Di Valentino, E., Diego, J. M., Doré, O., Douspis, M., Ducout, A., Dupac, X., Dusini, S., Efstathiou, G., Elsner, F., Enßlin, T. A., Eriksen, H. K., Fantaye, Y., Farhang, M., Fergusson, J., Fernandez-Cobos, R., Finelli, F., Forastieri, F., Frailis, M., Fraisse, A. A., Franceschi, E., Frolov, A., Galeotta, S., Galli, S., Ganga, K., Génova-Santos, R. T., Gerbino, M., Ghosh, T., González-Nuevo, J., Górski, K. M., Gratton, S., Gruppuso, A., Gudmundsson, J. E., Hamann, J., Handley, W., Hansen, F. K., Herranz, D., Hildebrandt, S. R., Hivon, E., Huang, Z., Jaffe, A. H., Jones, W. C., Karakci, A., Keihänen, E., Keskitalo, R., Kiiveri, K., Kim, J., Kisner, T. S., Knox, L., Krachmalnicoff, N., Kunz, M., Kurki-Suonio, H., Lagache, G., Lamarre, J.-M., Lasenby, A., Lattanzi, M., Lawrence, C. R., Jeune, M. L., Lemos, P., Lesgourgues, J., Levrier, F., Lewis, A., Liguori, M., Lilje, P. B., Lilley, M., Lindholm, V., López-Caniego, M., Lubin, P. M., Ma, Y.-Z., Macías-Pérez, J. F., Maggio, G., Maino, D., Mandolesi, N., Mangilli, A., Marcos-Caballero, A., Maris, M., Martin, P. G., Martinelli, M., Martínez-González, E., Matarrese, S., Mauri, N., McEwen, J. D., Meinhold, P. R., Melchiorri, A., Mennella, A., Migliaccio, M., Millea, M., Mitra, S., Miville-Deschênes, M.-A., Molinari, D., Montier, L., Morgante, G., Moss, A., Natoli, P., Nørgaard-Nielsen, H. U., Pagano, L., Paoletti, D., Partridge, B., Patanchon, G., Peiris, H. V., Perrotta, F., Pettorino, V., Piacentini, F., Polastri, L., Polenta, G., Puget, J.-L., Rachen, J. P., Reinecke, M., Remazeilles, M., Renzi, A., Rocha, G., Rosset, C., Roudier, G., Rubiño-Martín, J. A., Ruiz-Granados, B., Salvati, L., Sandri, M., Savelainen, M., Scott, D., Shellard, E. P. S., Sirignano, C., Sirri, G., Spencer, L. D., Sunyaev, R., Suur-Uski, A.-S., Tauber, J. A., Tavagnacco, D., Tenti, M., Toffolatti, L., Tomasi, M., Trombetti, T., Valenziano, L., Valiviita, J., Van Tent, B., Vibert, L., Vielva, P., Villa, F., Vittorio, N., Wandelt, B. D., Wehus, I. K., White, M., White, S. D. M., Zacchei, A. and Zonca, A. (2020). Planck 2018 results. VI. Cosmological parameters, *Astronomy & Astrophysics* **641**: A6. arXiv:1807.06209 [astro-ph].
URL: *http://arxiv.org/abs/1807.06209*

Rauch, M., Becker, G. D., Haehnelt, M. G., Gauthier, J.-R. and Sargent, W. L. W.

(2013). Extended and filamentary Lyα emission from the formation of a protogalactic halo at z = 2.63, *Monthly Notices of the Royal Astronomical Society* **429**(1): 429–443.
URL: *https://doi.org/10.1093/mnras/sts346*

Riaz, S., Hartwig, T. and Latif, M. A. (2022). Unveiling the Contribution of Population III Stars in Primeval Galaxies at Redshift $\gtrsim$6, *The Astrophysical Journal Letters* **937**(1): L6.
URL: *https://iopscience.iop.org/article/10.3847/2041-8213/ac8ea6*

Rosdahl, J., Blaizot, J., Aubert, D., Stranex, T. and Teyssier, R. (2013). ramses-rt: radiation hydrodynamics in the cosmological context, *Monthly Notices of the Royal Astronomical Society* **436**(3): 2188–2231.
URL: *https://doi.org/10.1093/mnras/stt1722*

Rosdahl, J., Blaizot, J., Katz, H., Kimm, T., Garel, T., Haehnelt, M., Keating, L. C., Martin-Alvarez, S., Michel-Dansac, L. and Ocvirk, P. (2022). LyC escape from SPHINX galaxies in the Epoch of Reionization, *Monthly Notices of the Royal Astronomical Society* **515**(2): 2386–2414. arXiv:2207.03232 [astro-ph].
URL: *http://arxiv.org/abs/2207.03232*

Rosdahl, J., Katz, H., Blaizot, J., Kimm, T., Michel-Dansac, L., Garel, T., Haehnelt, M., Ocvirk, P. and Teyssier, R. (2018). The SPHINX cosmological simulations of the first billion years: the impact of binary stars on reionization, *Monthly Notices of the Royal Astronomical Society* **479**(1): 994–1016.
URL: *https://doi.org/10.1093/mnras/sty1655*

Rosen, A. and Bregman, J. N. (1995). Global Models of the Interstellar Medium in Disk Galaxies, *The Astrophysical Journal* **440**: 634. ADS Bibcode: 1995ApJ...440..634R.
URL: *https://ui.adsabs.harvard.edu/abs/1995ApJ...440..634R*

Saslaw, W. C. and Zipoy, D. (1967). Molecular Hydrogen in Pre-galactic Gas Clouds, *Nature* **216**(5119): 976–978.
URL: *https://doi.org/10.1038/216976a0*

Schauer, A. T. P., Glover, S. C. O., Klessen, R. S. and Ceverino, D. (2019). The influence of streaming velocities on the formation of the first stars, *Monthly Notices of the Royal Astronomical Society* **484**(3): 3510–3521.
URL: *https://doi.org/10.1093/mnras/stz013*

Schauer, A. T. P., Glover, S. C. O., Klessen, R. S. and Clark, P. (2021). The influence of streaming velocities and Lyman–Werner radiation on the formation of the first stars, *Monthly Notices of the Royal Astronomical Society* **507**(2): 1775–1787.
URL: *https://doi.org/10.1093/mnras/stab1953*

SEDOV, L. (1959). *Similarity and Dimensional Methods in Mechanics*, Elsevier.
URL: *https://linkinghub.elsevier.com/retrieve/pii/C2013008173X*

Shapiro, P. R., Iliev, I. T. and Raga, A. C. (2004). Photoevaporation of cosmological minihaloes during reionization, *Monthly Notices of the Royal Astronomical Society* **348**(3): 753–782.
URL: *https://academic.oup.com/mnras/article-lookup/doi/10.1111/j.1365-2966.2004.07364.x*

Shapiro, P. R. and Raga, A. C. (2000). Reionization of the Universe and the Photoevaporation of Cosmological Minihalos. arXiv:astro-ph/0002100.
URL: *http://arxiv.org/abs/astro-ph/0002100*

Silk, J. (2013). UNLEASHING POSITIVE FEEDBACK: LINKING THE RATES OF STAR FORMATION, SUPERMASSIVE BLACK HOLE ACCRETION, AND OUTFLOWS IN DISTANT GALAXIES, *The Astrophysical Journal* **772**(2): 112.
URL: *https://iopscience.iop.org/article/10.1088/0004-637X/772/2/112*

Smith, A., Kannan, R., Garaldi, E., Vogelsberger, M., Pakmor, R., Springel, V. and Hernquist, L. (2022). The THESAN project: Lyman-alpha emission and transmission during the Epoch of Reionization, *Monthly Notices of the Royal Astronomical Society* **512**(3): 3243–3265. arXiv:2110.02966 [astro-ph].
URL: *http://arxiv.org/abs/2110.02966*

Smith, A., Safranek-Shrader, C., Bromm, V. and Milosavljević, M. (2015). The Lyman α signature of the first galaxies, *Monthly Notices of the Royal Astronomical Society* **449**(4): 4336–4362.
URL: *http://academic.oup.com/mnras/article/449/4/4336/1193683/The-Lyman-α-signature-of-the-first-galaxies*

Springel, V. (2009). E pur si muove: Galiliean-invariant cosmological hydrodynamical simulations on a moving mesh. Publisher: arXiv Version Number: 3.
URL: *https://arxiv.org/abs/0901.4107*

Springel, V. (2010). Moving-mesh hydrodynamics with the AREPO code, *Proceedings of the International Astronomical Union* **6**(S270): 203–206.
URL: *https://www.cambridge.org/core/product/identifier/S1743921311000378/type/journal_article*

Springel, V. (2011). Hydrodynamic simulations on a moving Voronoi mesh. arXiv:1109.2218 [astro-ph, physics:physics].
URL: *http://arxiv.org/abs/1109.2218*

Springel, V., Pakmor, R., Zier, O. and Reinecke, M. (2021). Simulating cosmic structure formation with the gadget-4 code, *Monthly Notices of the Royal Astronomical Society* **506**(2): 2871–2949.
URL: *https://academic.oup.com/mnras/article/506/2/2871/6312509*

Springel, V., White, S., Tormen, G. and Kauffmann, G. (2001). Populating a cluster of galaxies - I. Results at z=0, *Monthly Notices of the Royal Astronomical Society* **328**(3): 726–750. arXiv:astro-ph/0012055.
URL: *http://arxiv.org/abs/astro-ph/0012055*

Stinson, G. S., Brook, C., Macciò, A. V., Wadsley, J., Quinn, T. R. and Couchman, H. M. P. (2013). Making Galaxies In a Cosmological Context: the need for early stellar feedback, *Monthly Notices of the Royal Astronomical Society* **428**(1): 129–140.
URL: *https://doi.org/10.1093/mnras/sts028*

Tegmark, M., Silk, J., Rees, M. J., Blanchard, A., Abel, T. and Palla, F. (1997). How Small Were the First Cosmological Objects?, *The Astrophysical Journal* **474**(1): 1–12.
URL: *https://iopscience.iop.org/article/10.1086/303434*

Teyssier, R. (2002). Cosmological hydrodynamics with adaptive mesh refinement, *A&A* **385**(1): 337–364.
URL: *https://doi.org/10.1051/0004-6361:20011817*

Tornatore, L., Ferrara, A. and Schneider, R. (2007). Population III stars: hidden or disappeared?, *Monthly Notices of the Royal Astronomical Society* **382**(3): 945–950.
URL: *https://doi.org/10.1111/j.1365-2966.2007.12215.x*

Trebitsch, M., Blaizot, J., Rosdahl, J., Devriendt, J. and Slyz, A. (2017). Fluctuating feedback-regulated escape fraction of ionizing radiation in low-mass, high-redshift galaxies, *Monthly Notices of the Royal Astronomical Society* **470**: 224–239. ADS Bibcode: 2017MNRAS.470..224T.
URL: *https://ui.adsabs.harvard.edu/abs/2017MNRAS.470..224T*

Trebitsch, M., Volonteri, M., Dubois, Y. and Madau, P. (2018). Escape of ionizing radiation from high-redshift dwarf galaxies: role of AGN feedback, *Monthly Notices of the Royal Astronomical Society* **478**: 5607–5625. ADS Bibcode: 2018MNRAS.478.5607T.
URL: *https://ui.adsabs.harvard.edu/abs/2018MNRAS.478.5607T*

Triani, D. P., Sinha, M., Croton, D. J., Pacifici, C. and Dwek, E. (2020). The origin of dust in galaxies across cosmic time, *Monthly Notices of the Royal Astronomical Society* **493**(2): 2490–2505. arXiv:2002.05343 [astro-ph].
URL: *http://arxiv.org/abs/2002.05343*

Tseliakhovich, D. and Hirata, C. (2010). Relative velocity of dark matter and baryonic fluids and the formation of the first structures, *Physical Review D* **82**(8): 083520.
URL: *https://link.aps.org/doi/10.1103/PhysRevD.82.083520*

van de Voort, F., Schaye, J., Altay, G. and Theuns, T. (2012). Cold accretion flows and the nature of high column density H_I absorption at redshift 3, *Monthly Notices of the Royal Astronomical Society* **421**(4): 2809–2819.
URL: *https://doi.org/10.1111/j.1365-2966.2012.20487.x*

Weinberger, R., Springel, V., Hernquist, L., Pillepich, A., Marinacci, F., Pakmor, R., Nelson, D., Genel, S., Vogelsberger, M., Naiman, J. and Torrey, P. (2017). Simulating galaxy formation with black hole driven thermal and kinetic feedback, *Monthly Notices of the Royal Astronomical Society* **465**(3): 3291–3308. arXiv:1607.03486 [astro-ph].
URL: *http://arxiv.org/abs/1607.03486*

Weinberger, R., Springel, V. and Pakmor, R. (2020). The AREPO Public Code Release, *The Astrophysical Journal Supplement Series* **248**(2): 32.
URL: *https://iopscience.iop.org/article/10.3847/1538-4365/ab908c*

White, M. (2001). The mass of a halo, *Astronomy & Astrophysics* **367**(1): 27–32. arXiv:astro-ph/0011495.
URL: *http://arxiv.org/abs/astro-ph/0011495*

Wise, J. H. (2019). An Introductory Review on Cosmic Reionization, *Contemporary Physics* **60**(2): 145–163. arXiv:1907.06653 [astro-ph].
URL: *http://arxiv.org/abs/1907.06653*

Wolfire, M. G., McKee, C. F., Hollenbach, D. and Tielens, A. G. G. M. (2003). Neutral Atomic Phases of the Interstellar Medium in the Galaxy, *The Astrophysical Journal* **587**(1): 278–311.
URL: *https://iopscience.iop.org/article/10.1086/368016*

Zapartas, E., De Mink, S. E., Izzard, R. G., Yoon, S.-C., Badenes, C., Götberg, Y., De Koter, A., Neijssel, C. J., Renzo, M., Schootemeijer, A. and Shrotriya, T. S. (2017). Delay-time distribution of core-collapse supernovae with late events resulting from binary interaction, *Astronomy & Astrophysics* **601**: A29.
URL: *http://www.aanda.org/10.1051/0004-6361/201629685*

Zonca, A., Singer, L., Lenz, D., Reinecke, M., Rosset, C., Hivon, E. and Gorski, K. (2019). healpy: equal area pixelization and spherical harmonics transforms for data on the sphere in Python, *Journal of Open Source Software* **4**(35): 1298.
URL: *http://joss.theoj.org/papers/10.21105/joss.01298*

A Projections of galaxies with high escape fractions and low stellar masses

In Figure 12 a few galaxies galaxies at high redshifts with low stellar masses and high escape fractions were visible. While some of these galaxies are insufficiently resolved, for others the number of gas cells implies a sufficient resolution. Projections of two of these galaxies are shown in Figure A.1 and Figure A.2. While Figure A.1 shows a volume-weighted projection of the gas number density of a halo with more than 1000 gas cells and Figure A.2 shows a halo with less than 1000 gas cells. The colour of the stars in these plots indicates their age.

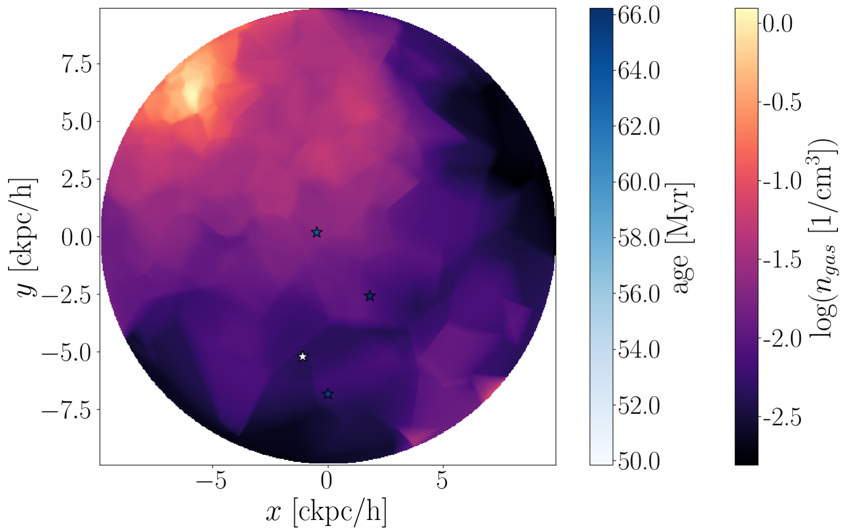

Figure A.1: Volume-weighted projection of the gas number density in a halo, which has a high escape fraction but a low stellar mass. This halo has 1460 cells. The colour of the stars indicates their age.

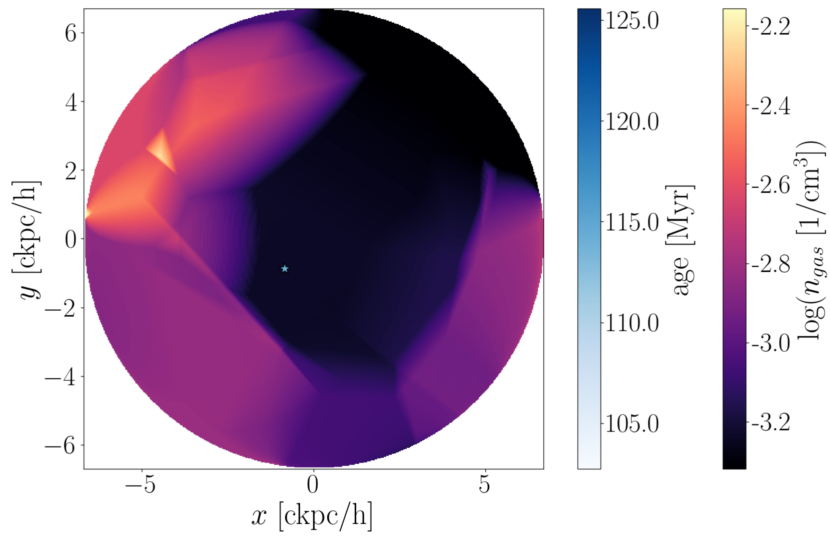

Figure A.2: Volume-weighted projection of the gas number density in a halo, which has a high escape fraction but a low stellar mass. This halo has 197 cells. The colour of the star indicates its age.

B Gas mass versus stellar mass

The scatter plots of the escape fraction versus the stellar mass of different galaxies in Figure 12 show a generally positive correlation. However, one would expect galaxies with high stellar masses to contain high gas masses as well. These high gas masses could, in turn, decrease feedback efficiency and lead to lower escape fractions. This cannot be seen in Figure 12. To see how the gas mass behaves for different stellar masses, the gas mass was plotted versus the stellar mass in Figure B.1 for six different redshift ranges for galaxies found in the high-resolution region of the medium group. The colour of the points indicates the escape fraction. The grey dotted line shows a linear relation between the gas mass and stellar mass with a slope of 1. It becomes clear that the gas mass increases slower than the stellar mass.

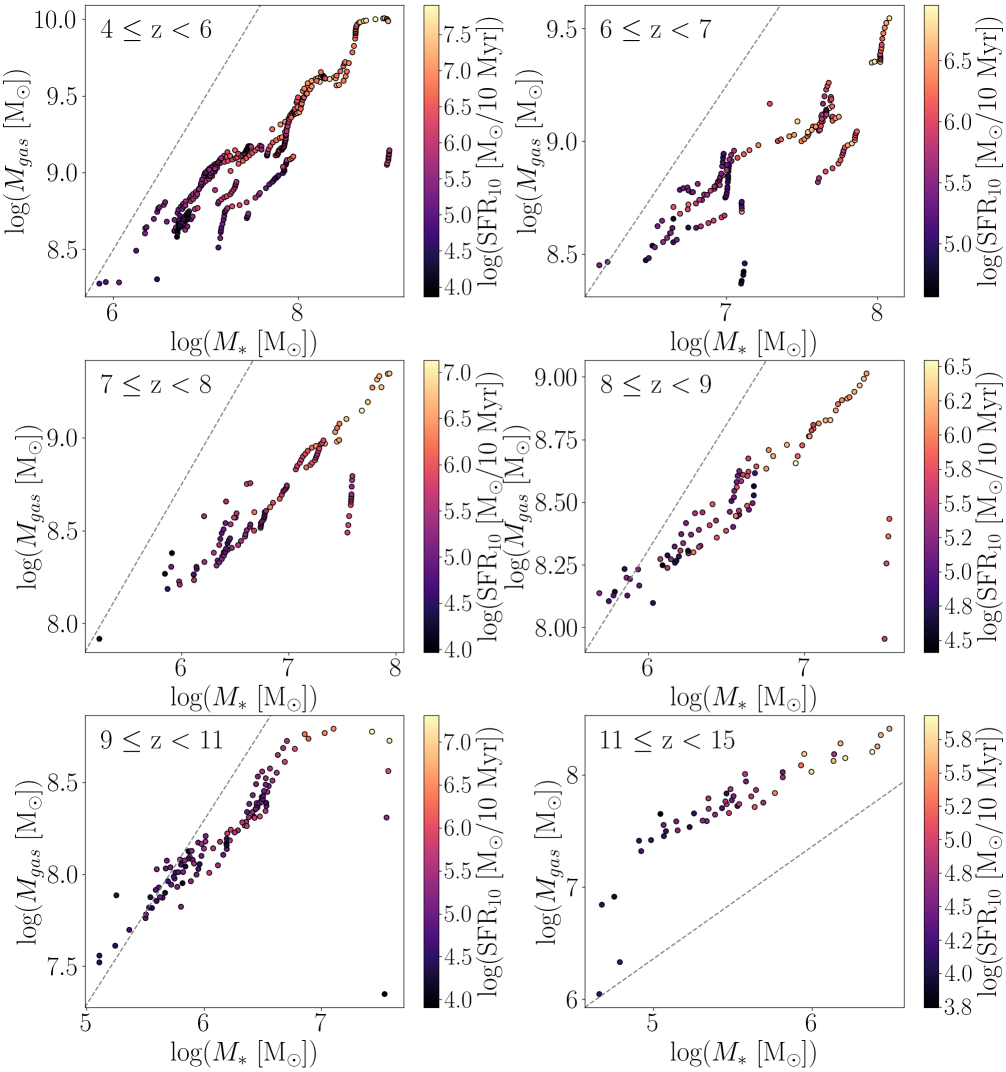

Figure B.1: Gas mass versus stellar mass for six different redshift ranges. The colour of the points indicates the escape fraction. The grey dotted line shows a linear relation between the stellar mass and gas mass with a slope of 1, i.e. if the gas mass increases by a value, the stellar mass increases by the same value. Each data point is based on one of the ten largest halos of one of the snapshots in the redshift range shown on the top of the panels. The haloes were taken from the high-resolution region of the re-simulation of the medium group, which has a virial mass of 4.74 $\times 10^{10}$ $M_\odot$ at redshift 4.57.

C Ionised hydrogen fraction versus redshift

When investigating the median of the escape fraction versus the redshift in Figure 21, it becomes apparent that it flattens for all three groups at some point. To investigate if this effect is due to the ionisation of the high-resolution regions of these three groups or rather due to e.g. the sample of the galaxies chosen, a plot of the mass-weighted mean ionised hydrogen fraction versus the redshift is plotted in Figure C.1. The ionised hydrogen fraction shows a flattening for all three groups as well at similar redshifts at which the escape fraction flattens in Figure 21.

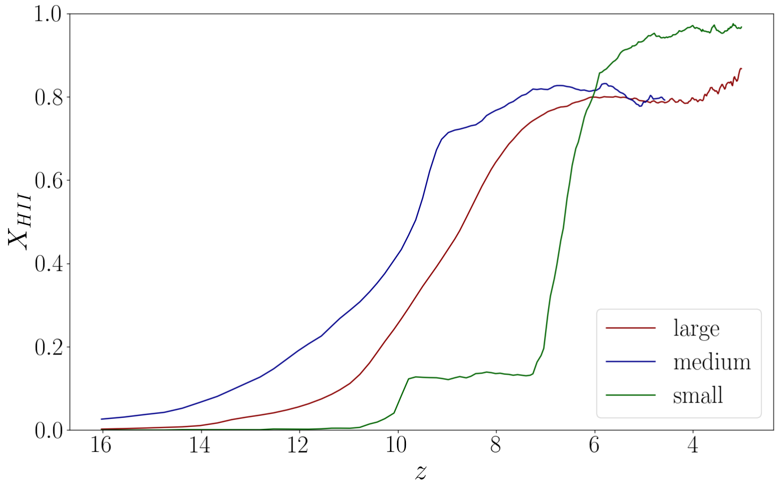

Figure C.1: Ionised hydrogen fraction versus the redshift. For each snapshot of each re-simulated THESAN group, the mass-weighted mean of the ionised hydrogen fraction in the high-resolution region is shown. The three THESAN groups are colour-coded. Red corresponds to the large group, which has a mass of 4.25×10^{12} $M_{\odot}$ at redshift 3, blue corresponds to the medium group, which has a mass of 4.74×10^{10} $M_{\odot}$ at redshift 4.6, and green corresponds to the small group, which has a mass of 1.94×10^{9} $M_{\odot}$ at redshift 3.

D Declaration of Authorship

I hereby certify that I have written this thesis independently and that I have not used any sources or auxiliaries other than those indicated.

Nele Stachlys